RELATING TENSILE PROPERTIES TO MICROSTRUCTURAL HETEROGENEITIES IN ELASTOMERIC MATERIALS

A Dissertation

Presented to the Faculty of the Graduate School

of Cornell University

In Partial Fulfillment of the Requirements for the Degree of

Doctor of Philosophy

by

Bernardo Mauricio Aguilera-Mercado

August 2012

RELATING TENSILE PROPERTIES TO MICROSTRUCTURAL HETEROGENEITIES IN ELASTOMERIC MATERIALS

Bernardo Mauricio Aguilera-Mercado, Ph. D.

Cornell University 2012

Through both molecular modeling and experimental measurements, this investigation seeks a deeper understanding of the underlying relationships between nanostructure and tensile properties in elastomeric networks. We study how the elastic response strongly depends upon microstructural heterogeneities in two different classes of elastomers: first, networks made of chains with bimodal molar mass distributions where heterogeneity arises from purely entropic effects; and second, model liquid crystal elastomers with idealized regular connectivity where microstructural heterogeneities arise from orientational entropic contributions in combination with enthalpic interactions. First, we examine why certain bimodal polymer networks exhibit pronounced improvements of their tensile properties over that of unimodal networks with similar elastic modulus. We explore the impact of composition on the network topology, chain-segment orientation, and tensile enhancement through molecular simulations in addition to ^{2}H-NMR and SANS measurements on PDMS samples. We also derive a novel method, based on the maximum entropy principle, to extract segment orientation distributions from ^{2}H-NMR spectra. After validating our simulation model by comparison with experimental data, we find that optimal tensile properties occur in systems where the concentration of shorter chains slightly exceeds their percolation transition and hence spatial cross-linking heterogeneity is small. Through the use of network topological footprints, we attribute the higher extensibility

of certain bimodal networks (than that of unimodal networks with similar modulus) to their greater spread in the distribution of shortest path lengths between pairs of monomers. Lastly, we explore the tensile response of idealized regular liquid-crystalline elastomers via molecular simulations. Such networks exhibit a distinct *sawtooth*-shaped elastic response similar to that of super-tough natural materials (e.g., nacre, titin, spider silk). This unique tensile response arises from a deformation mechanism that entails the successive creation and distortion of ordered (smectic C_A) chain domains in concert with crosslink segregation and layering. We also investigate the impact of chain stiffness, network architecture, and the use of end-linked tri-block copolymer chains on the elastic response. This chemical bidispersity further stabilizes the smectic chain domains, via microphase separation of the different blocks, and consequently enhances the tensile properties (e.g., toughness and modulus) of these idealized networks with mesogenic tri-block copolymer chains.

BIOGRAPHICAL SKETCH

Bernardo M. Aguilera-Mercado was born in Caracas, Venezuela and received his undergraduate Chemical Engineering degree at *Universidad Nacional Experimental Politécnica "Antonio José de Sucre"* in Barquisimeto, Venezuela in 2003. His undergraduate research and industrial projects dealt with mathematical modeling of trickle-bed reactors for gasoil hydrotreatment process, and statistical modeling of physical properties of crude oil fractions at the Paraguaná crude oil (Amuay) Refinery Complex, respectively. Subsequently, he began his graduate studies at *Universidad Simon Bolívar* in Caracas, Venezuela and obtained a master's degree in Chemical Engineering in 2005. His master's research involved, under the guidance of Professor Erich A. Müller, the development of a coarse-grained molecular model for the onset of asphaltene aggregation in crude oils. Later, Bernardo joined the Ph.D. program at the School of Chemical and Biomolecular Engineering at Cornell University in Ithaca, New York. Under the guidance of Professors Fernando A. Escobedo and Claude Cohen, Bernardo carried out the investigation, contained herein, on the relationships between the tensile properties and the microstructure in elastomeric materials. Bernardo plans to continue his research and modeling career, and has recently joined the Fabric and Home Care Research and Development organization of the Procter & Gamble Company, where he will develop thermodynamic and kinetic models of physico-chemical processes involved in detergency.

A mis padres Ana María y Bernardo y a minha "*Coelhinha*" Anna.

También a aquellos que lamentablente ya no se encuentran entre nosotros pero que fueron grandes fuentes de inspiración para mi persona: mis abuelos Mercedes, Hilda, Felipe y Bernardo y mis primeros mentores en matemática e ingeniería, Profesores Daniel Mujica y Jesús Pérez Ortega.

ACKNOWLEDGMENTS

I would like to sincerely thank both of my research advisors, Professors Fernando A. Escobedo and Claude Cohen, for their invaluable technical and personal guidance. Both Fernando and Claude were always available, and particularly at the moments I most needed their support; they were, and still are, terrific mentors in many aspects much beyond academic matters. I simply cannot thank both of you enough for all your support, patience, and constant encouragement. Joining your research groups was definitely a complete privilege and my entire pleasure.

I would also like to thank my parents Ana María and Bernardo for being always next to me in spite of the distance. I am also extremely thankful to my aunts Patricia, Marta, and Silvana in addition to two very special members of my extended family, Yvonne and Elisa Verano, for their unconditional support during the tough times my family has gone through. Definitely, I could not have come this far without the kind and genuine support all of they have given me; I am truly thankful to all and each of you.

In addition, I would like to especially thank Anna "*Coelhinha*" for your perpetual source of optimism and irradiating positive thoughts. Probably, you do not have an idea how much you contributed to this goal I have just achieved with your steady and inspiring encouragement. You made me realize I was not alone and provided me with the extra energy necessary to face and overcome my own ghosts and unjustified fears. I, therefore, also have to thank Ithaca and Cornell for giving me the blessing of entangling our life paths in such a wonderful way. It certainly was the greatest and most beautiful thing that has happened to me since I arrived in this country. Thank you so much for being such an important part of my life! I love you Anna.

Additionally, I would like to thank former and current members of both Escobedo and Cohen research groups with whom I had uncountable fruitful discussions and collaborations. I especially thank Camilo, Francisco, Geoff, Ernesto, Ivan, Umang, Beth, Stacey, Poornima, Pooja, Sushmit, Juan Carlos, Salomon, and Carlos. I especially thank as well Paulette, Benjamin, Lynden, T. Michael, Yong, Brad, and Abraham for their valuable teachings and their always-open door policy. In addition, I thank all those special friends that made Ithaca extremely enjoyable to me, despite its winter weather, most especially Camilo, Francisco, Paula, and Andreas.

Finally, I would like to convey my gratitude to the National Science Foundation and the American Chemical Society for funding this research work.

TABLE OF CONTENTS

LIST OF FIGURES

LIST OF TABLES

CHAPTER 1

EXTRACTION OF SEGMENT ORIENTATION DISTRIBUTIONS IN POLYMER NETWORKS BY INVERSION OF ^{2}H-NMR SPECTRA THROUGH THE MAXIMUM-ENTROPY METHOD*

1.0 Abstract

We present a simple and computationally inexpensive strategy, to first estimate the average segment-orientation order parameter and then, based on the maximum-entropy method, extract distributions of this order parameter from the conventionally measured ^{2}H-NMR spectra. The proposed methodology allows for a more complete characterization of the segmental orientation behavior as compared to solely measuring the observed quadrupolar splittings. The latter approach only quantifies the segment orientation due to local excluded volume interactions, and does not account for the orientation arising from the network topology that is manifested through the width of the spectral "wings". The application of the proposed strategy can be especially advantageous in polymer networks exhibiting highly heterogeneous segment-orientation responses (e.g., bimodal networks) and complex ^{2}H-NMR spectrum lineshapes. The methodology is validated with both molecular simulation and experimental results as well as applied to complex spectral data of a PDMS sample.

1.1 Introduction

Elastomer networks are materials with a great variety of applications; typical examples are O-rings, tires, and rubber bands. These materials can be deformed repeatedly to large extents without losing their properties.[1] These outstanding

* Reprinted with permission from Aguilera-Mercado, B. M.; Cohen, C.; Escobedo, F. A. *Macromolecules* **2009**, *42*, 8889-8898.

macroscopic properties are entropic in nature and have their origin in the network structure at the nanoscale.[1,2] For about three decades deuterium nuclear magnetic resonance (^{2}H-NMR) experiments have been extensively used in polymer melts and gels to probe microscopic information about configurational entropy, segmental order, and dynamics of polymer chains.[3,4] Such microscopic characterizations have provided valuable experimental evidence to validate various theories in the field of polymer physics.

Most of the ^{2}H-NMR experimental studies[5-15] on segmental orientation in strained polymer melts and gels have, however, centered solely on the observed quadrupolar splitting—or doublet—between the peaks of the ^{2}H-NMR spectrum. The doublet separation is related to the frequency value that maximizes its distribution (i.e., the most probable value) rather than the average frequency splitting or segment-orientation order parameter.[16-18] The observed splitting is therefore not a measure of the total average orientation of the chain segments but the orientation arising from mean-field-like excluded-volume interactions among the chain segments.[16,19-21] Conversely, the lineshape of the NMR spectrum at higher frequencies captures the contribution to segment orientation due to topological network constraints, such as cross-links, and trapped entanglements.[19,22] For instance, networks having a significant fraction of highly stretched end-linked chains—with their chain ends attached to rather distant cross-links—yield NMR spectra with wider "wings".[22]

The total average orientation order parameter (or average frequency splitting) must reflect contributions to segment orientation from both excluded-volume and topological constraints. Hence, the observed splitting of the NMR spectrum may not always be an adequate way to characterize segmental order in elastomeric systems.

For example, in some bimodal networks, upon uniaxial deformation, short-chain segments exhibit a significantly higher overall degree of orientation than that of the long-chain segments;[23,24] yet, the observed splittings for segments of both short and long chains are very similar.[15] It is relevant to mention that obtaining the average orientation from spectral data is not a trivial calculation. Since the ^{2}H-NMR spectrum is the symmetric part of the orientation order parameter distribution,[16] extracting this distribution or its overall average from the spectrum, without any additional information about the shape of the distribution, is an ill-posed problem.

Jacobi et al.[18] estimated the overall average of the order parameter of segmental orientation from the ^{2}H-NMR spectrum through products between the arithmetic and harmonic mean-averages of square roots of shifted order parameter absolute values. Such estimation notably overpredicted the overall average order parameter at small uniaxial deformations; as a result, only differences with respect to the unstrained state of the estimated order parameters were considered in that study.[18] Due to the difficulty in estimating the average of the orientation order parameter, measures of the total orientation and its different contributions have been usually obtained from fitting ^{2}H-NMR spectral data to multi-parameter analytical functions, typically derived from mean-field-based models that involve ideal chain statistics.[19] Nevertheless, mean-field models may not be suitable for an accurate description of systems with highly heterogeneous segmental orientation responses, such as multimodal networks.

Another interesting system in which fitting spectral data to simple mean-field-based models may not be appropriate—particularly due to its ^{2}H-NMR spectrum lineshape complexities—has been recently documented. In that investigation Genesky and coworkers[25] found a clear (peculiar) shoulder in the ^{2}H-NMR spectrum lineshape

at high extension ratios and two characteristic quadrupolar splittings (two pairs of doublets) on uniaxially stretched and nearly ideal polydimethylsiloxane (PDMS) end-linked networks made of chains with relatively high molar mass.

Using a different spectroscopic technique (proton-proton multiple quantum nuclear magnetic resonance) and data analysis approach, Saalwächter et al.[23,26-28] and Gjersing et al.[29] obtained overall averages and distributions of the orientation order parameter on (dry or swollen) unimodal, bimodal, and filled trimodal polymer networks. The authors of those works extracted the distributions of the order parameter from double-quantum build-up intensity curves by numerical Tikhonov regularization[30,31] analysis. The Tikhonov regularization estimates a solution for ill-posed problems involving Fredholm integral equations.[30,31] This regularization approach has also been used to determine order parameter distributions from NMR spectroscopic data in many other systems, such as liquid crystals,[32,33] lipid bilayers,[34] spider dragline silk,[35] and glassy polymers.[36]

Another very well known and commonly used method for the solution of ill-posed problems is the maximum-entropy method (MEM),[30] which through the maximum-entropy principle yields the least biased and most probable solution estimate based on the given information.[37-39] MEM has been successfully applied to a great variety of systems and experimental techniques to determine, for instance, polystyrene distributions of relaxation times using light scattering,[40] second and fourth orientation order parameters using optical spectroscopy,[41] and structural conformations of organic and biological molecules using ^{1}H-NMR and ^{2}H-NMR.[42-44] In addition, hybrid schemes using MEM as a complement of the Tikhonov regularization have been recently proposed in order to suppress oscillatory responses,

with unphysical negative portions, that the Tikhonov regularization may exhibit in the presence of finite noise.[45] Thus, MEM may as well be an appropriate method choice for interpreting ^{2}H-NMR spectral data and obtaining an estimate of the distribution of the orientation order parameter in elastomers.

Herein we present a simple and computationally inexpensive strategy, based on MEM, to extract distributions of the segmental orientation order parameter from the conventionally measured ^{2}H-NMR spectra. This proposed methodology allows for a rather accurate description of the segmental orientation behavior in polymer networks as it takes into account the contributions to segment orientation arising from both the so-called excluded-volume effects[16-22] and topological constraints. In addition, the advocated procedure is expected to be especially useful when applied to polymer networks exhibiting highly heterogeneous segmental orientation responses and complex ^{2}H-NMR spectrum lineshapes. The rest of this work is organized as follows: first, in Section 1.2 we present a derivation of an expression that estimates the overall average frequency splitting or average segment-orientation order parameter in terms of the average absolute value of the order parameter, which can be directly obtained from the ^{2}H-NMR spectrum. Also in Section 1.2, we use MEM to find the probability distribution of the segment-orientation order parameter from ^{2}H-NMR spectrum and the estimated average order parameter. In Section 1.3 we describe the computational methods and simulated (unimodal and bimodal) networks used to validate the proposed strategy. In Section 1.4 we show the results of the validation with spectral data of the simulated networks and experimental PDMS samples, provided by Genesky et al.,[25,46] as well as an application of the proposed methodology to an

experimental network with complex spectrum lineshape.[25] Finally, we conclude with Section 1.5.

1.2 Theoretical Calculations

1.2.1 Basic ^{2}H-NMR Concepts. Here we recall elementary results of ^{2}H-NMR that are relevant for our purpose only; detailed descriptions about the theory of ^{2}H-NMR are beyond the scope of this paper and can be found elsewhere.[8,47,48] If chain segments are in "the fast motion limit", i.e., polymer networks at temperatures above their corresponding glass transition temperatures, the ^{2}H-NMR frequency spectrum of a deuterated sample is the result of the superposition of discrete frequency doublets, with separation $|\delta\nu_i|$, from all deuterium-labeled molecules in the system. Each doublet or quadrupolar splitting consists of two delta functions at $\nu=\pm|\delta\nu_i|/2$. The quadrupolar splitting of the ith deuterated unit and its orientation with respect to the applied magnetic field are related by[5]

$$\delta\nu_i = 3/2\,\delta_Q P_2\left(\cos\theta_i\right)^* \tag{1.1}$$

where δ_Q is the static quadrupolar constant, the P_2 term is the second Legendre polynomial, and θ_i is the angle between the magnetic field and the ith C-^{2}H bond. The asterisk denotes time average over fast segmental reorientations. By taking the average over all of the deuterated units in a uniaxially deformed sample and using the spherical harmonic addition theorem, the overall (or ensemble) average frequency splitting is the following,

$$\left|\left\langle\delta\nu\right\rangle\right| = 3/2\,\delta_Q\left|P_2\left(\cos\Omega\right)\left\langle P_2\left(\cos\phi_i\right)^*\right\rangle\left\langle P_2\left(\cos\psi_i\right)^*\right\rangle\right| \tag{1.2}$$

where angular brackets represent average over all of the deuterated units, Ω is the angle between the magnetic field applied and the strain axis, ϕ_i is the angle between the ith C-^{2}H bond and the vector of the chain-segment to which is attached, and ψ_i is the angle between the ith chain-segment vector and the strain axis. The average segment-orientation order parameter $\langle S^* \rangle$ is $\langle P_2(\cos\psi_i)^* \rangle$. As long as both $P_2(\cos\Omega)$ and $\langle P_2(\cos\phi_i)^* \rangle$ are different from zero, ω can be defined as a dimensionless frequency such that the magnitude of the average dimensionless frequency $|\langle\omega\rangle|$ (i.e., $|\langle\delta\omega\rangle|/2$, which is half of the average dimensionless splitting) is equal to $|\langle S^* \rangle|$. Then, ω is written as:

$$\omega = \frac{\nu}{3/4\,\delta_Q P_2(\cos\Omega)\left\langle P_2(\cos\phi_i)^* \right\rangle} \tag{1.3}$$

If the total width of the frequency spectrum is large enough when compared to the inverse of the characteristic relaxation time, i.e., segments are in "fast motion limit", the spectrum $F(\omega)$ can be written as the symmetrized time-averaged-segment-orientation order parameter distribution,[16] that is

$$F(\omega) \propto \rho(\omega) + \rho(-\omega) \tag{1.4}$$

where $\rho(\omega)$ (or $\rho(S^*)$) is the probability density distribution of the measured dimensionless frequency or the time-averaged orientation order parameter for the entire population of segments. It is important to emphasize that this distribution $\rho(S^*)$ of the time-averaged orientation order parameter is, by definition, different from the distribution $p(S)$ of the instantaneous orientation order parameter. This is because $\rho(S^*)$ is the resulting distribution from sampling pre-averaged values of the order

parameter S, which is distributed through the density function $p(S)$. However, the ensemble averages or first moments of these two density distributions are then identical as these functions characterize (under different sampling schemes) the same segment population. Nonetheless, both distributions would be nearly identical in the case of a frozen sample network, wherein all the segments were approximately fixed in space within the duration time of the ^{2}H-NMR measurement. The distribution $p(S)$ of the instantaneous orientation order parameter is therefore closely related to the solid state NMR spectrum of the frozen sample. The qualitative differences in the lineshape of these two different distributions of the same population of segments are exemplified in Figure 1.1a. Further on this article, we focus on the time-averaged orientation order parameter distribution, which is the only one that can be related to ^{2}H-NMR measurements in amorphous polymer networks (above their glass transition temperature), and simply refer to it as the orientation order parameter distribution.

The observed frequency splitting $\Delta\omega$, which is twice the magnitude of the most probable frequency $|\omega_{max}|$ (where ω_{max} maximizes $\rho(\omega)$), accounts only for the orientation due to the excluded-volume interactions among the chain segments.[16,19-21] On the other hand, the average frequency splitting $|<\delta\omega>|$, twice the magnitude of the average frequency $|<\omega>|$, gives a measure of the total degree of orientation, including the orientation contributions from both excluded-volume interactions and topological constraints. A typical sketch, obtained from one of the simulated networks, of the relationships between $F(\omega)$,$\rho(\omega)$,$\Delta\omega$,$<\omega>$, and $<\delta\omega>$ is shown in Figure 1.1b.

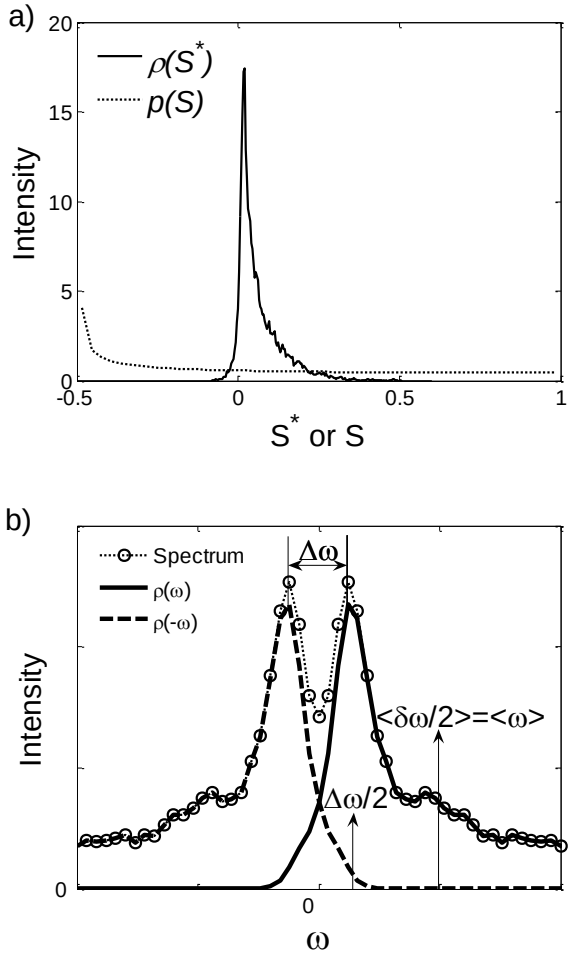

Figure 1.1: Segment orientation order parameter distributions, frequency spectrum, observed and average frequency splittings. a) Comparison between the instantaneous and time-averaged orientation order parameter distributions for a simulated unimodal-15-bead network when uniaxially stretched 2.15 times its original size (<*S*>=0.06). b) Sketch of the relationships between the spectrum, the frequency or order parameter distribution, the observed quadrupolar splitting $\Delta\omega$, the average splitting $\langle\delta\omega\rangle$, and average frequency $\langle\omega\rangle$.

1.2.2 Estimating the Average Segment-orientation Order Parameter. As stated above, the average order parameter $\langle S^* \rangle$ or frequency $\langle\omega\rangle$ cannot be calculated directly from the symmetric function $F(\omega)$, whose all its odd moments are equal to zero. However, the average absolute value of the frequency $\langle|\omega|\rangle$ can be obtained from the spectrum $F(\omega)$ in a straightforward fashion as follows:

$$\left\langle |\omega| \right\rangle = \int_{-1}^{+1} |\omega| \rho(\omega) d\omega = \frac{\int_{-1}^{+1} |\omega| F(\omega) d\omega}{\int_{-1}^{+1} F(\omega) d\omega} \tag{1.5}$$

Let $\Re$ be defined as the difference between the average absolute value of the frequency and the magnitude of its average. $\Re$ can then be written in terms of $\rho(\omega)$ as

$$\Re = \left\langle |\omega| \right\rangle - \left| \langle \omega \rangle \right| = \begin{cases} 2\int_{-1}^{0} (-\omega) \rho(\omega) d\omega & \text{if } \langle \omega \rangle \geq 0 \\ 2\int_{0}^{+1} \omega \rho(\omega) d\omega & \text{if } \langle \omega \rangle < 0 \end{cases} \tag{1.6}$$

It is important to recall that $\Re$ is always greater than or equal to zero, due to the triangle inequality, and for the type of bell-shaped distributions of interest, $\Re$ decreases asymptotically toward zero as $|\langle\omega\rangle|$ increases.

Our approach to estimate the average order parameter consists in approximating $\Re(|\langle\omega\rangle|)$ through Taylor expansions around the unstretched state when $|\langle\omega\rangle| = |\langle\omega\rangle|_0 = 0$, this is assuming that the sample is isotropic when unstretched. If the segments of the sample were not isotropically distributed at the unstretched state, that is, $|\langle\omega\rangle|_0 > 0$, our approach would then estimate the difference of the order parameter with respect to the unstretched state (i.e., $|\langle\omega\rangle - \langle\omega\rangle_0|$) as only Taylor expansions around that state are performed at this stage. The following step is to assume that $\rho(\omega)$ can be reasonably approximated by translating the distribution at the unstretched state $\rho_0(\omega)$ when $|\langle\omega\rangle - \langle\omega\rangle_0|$ is "small enough", i.e., $\rho(\omega) \cong \rho_0(\omega - \langle\omega\rangle + \langle\omega\rangle_0)$ or simply $\rho(\omega) \cong \rho_0(\omega - \langle\omega\rangle)$ for an isotropic sample. This "translation invariance"

approximation is expected to be less accurate when applied to spectral data of relatively short chains (which do not exhibit Gaussian statistics) due to the more pronounced skewness (or asymmetry) of their $\rho(\omega)$ distribution upon deformation; this effect is evidenced by wide spectral "wings" and a severe spectrum broadening upon stretching.

The last step is to perform a Taylor expansion of $\ln(1/\Re)$ instead of $\Re$. Because of this particular choice of expansion, the first term captures the behavior of $\Re$ not only at small values of $|<\omega>|$ but also at large values of $|<\omega>|$ as the resulting approximation for $\Re$ decays exponentially to zero with $|<\omega>|$. Taylor expanding other functions of $\Re$, different from $\ln(1/\Re)$, can produce similar results as long as their inverses are always positive and decay monotonically to zero. The algebraic details of a slightly more general version of this derivation can be found in the Appendix. Equation (1.7) is the resulting expression (after neglecting second order terms) from which the magnitude of the average frequency $|<\omega>|$ can be estimated. Equation (1.7) approximately relates $<|\omega|>$ with $|<\omega>|$ both scaled with respect to $<|\omega|>_0$, where $<|\omega|>_0$ is the average absolute value of the frequency when the sample is unstretched, and gives a measure of the spectrum width.

$$\frac{\langle|\omega|\rangle}{\langle|\omega|\rangle_0} \cong \frac{|\langle\omega\rangle|}{\langle|\omega|\rangle_0} + \exp\left(-\frac{|\langle\omega\rangle|}{\langle|\omega|\rangle_0}\right) \tag{1.7}$$

It is important to stress that by numerically solving Equation (1.7) an estimate for the magnitude of the average order parameter $|<\omega>|$ can be obtained from the

average absolute value of the order parameter $<|\omega|>$, which can be easily calculated from the ^{2}H-NMR spectrum.

This approximation can be extended in order to estimate the magnitude of any odd moment of $\rho(\omega)$ from its symmetric part (or spectrum) $F(\omega)$. Equation (1.8) results from generalizing the procedure described above, and allows approximate calculations of magnitudes of higher order odd moments $|<\omega^{2k-1}>|$ in terms of average absolute values of odd powers of the order parameter $<|\omega|^{2k-1}>$ with k=1,2,…,*M*. These average absolute values of odd powers $<|\omega|^{2k-1}>$ can be directly calculated from the spectrum in an analogous way as $<|\omega|>$ is obtained from Equation (1.5). Both the derivation of Equation (1.8) and the equivalent version of Equation (1.5) for higher order odd powers can be found in the Appendix.

$$\frac{\left\langle |\omega|^{2k-1} \right\rangle}{\left\langle |\omega|^{2k-1} \right\rangle_0} \cong \frac{\left| \left\langle \omega^{2k-1} \right\rangle \right|}{\left\langle |\omega|^{2k-1} \right\rangle_0} + \exp\left(- \frac{\left| \left\langle \omega^{2k-1} \right\rangle \right|}{\left\langle |\omega|^{2k-1} \right\rangle_0} \right) \tag{1.8}$$

1.2.3 Obtaining the Segment-orientation Order Parameter Distribution. The probability distribution of the segment-orientation order parameter is estimated from the ^{2}H-NMR spectral data by applying MEM, which provides the "best" solution estimates for ill-posed problems given the available information.[37] The information known about the solution is specified through a set of constraints, and MEM yields the solution distribution with the greatest Shannon–Jaynes entropy that satisfies the imposed set of constraints. Here, we present a solution for a discretized probability density function, equally spaced in ω, of the orientation order parameter. The Shannon–Jaynes or information entropy, which in this case is a discretized version of

the free energy associated with the orientational entropy of the polymer segments,[8] is defined as[37]

$$A(\rho(\omega_1),...,\rho(\omega_N)) = -\sum_i [\rho(\omega_i)\ln(\rho(\omega_i))] \tag{1.9}$$

Herein the available information about the order parameter distribution is written as the following set of constraints:

1) The distribution has to be normalized,

$$\int_{-1}^{+1} \rho(\omega) d\omega = 1 \tag{1.10}$$

2) The symmetric part of the distribution must be proportional to the ^{2}H-NMR spectrum,

$$F(\omega_i) = c \cdot [\rho(\omega_i) + \rho(-\omega_i)] \tag{1.11}$$

where *c* is a proportionality constant, which will be absorbed in the normalization constant resulting from constraint 1. It is important to stress that this constraint can be simply written as Equation (1.11) only because chain segments are assumed to be in "the fast motion limit", otherwise the Fourier transform of the relaxation function (written in terms of $\rho(\omega_i)$ and the characteristic relaxation time) should be used instead; this would certainly lead to more complicated algebraic expressions, which may require a numerical solution.

3) And, the average order parameter is approximately calculated from solving Equation (1.7), that is

$$\int_{-1}^{+1} \omega\rho(\omega) d\omega \cong \langle\omega\rangle_{Eqn(1.7)} \tag{1.12}$$

In the strict sense Equation (1.7) estimates $|\langle\omega\rangle|$ instead of $\langle\omega\rangle$, but the sign of $\langle\omega\rangle$ is determined by the type of deformation performed. In uniaxial extension the sign of $\langle\omega\rangle$ is positive, whereas in compression it is negative.

Since we are solving for discrete values of the distribution, the integrals must be replaced by their corresponding and approximated discrete forms. The resulting probability distribution that maximizes $A(\rho(\omega_1),...,\rho(\omega_N))$, subject to the constraints (Equations 1.10, 1.11,and 1.12) can be written in terms of the ^{2}H-NMR spectrum as follows:

$$\rho(\omega_i)=\left[\int_{-1}^{+1}\frac{F(\omega)d\omega}{1+\exp(-\lambda\omega)}\right]^{-1}\left[\frac{F(\omega_i)}{1+\exp(-\lambda\omega_i)}\right] \tag{1.13}$$

where λ is the Lagrange multiplier associated with constraint 3, and obtained by solving the following nonlinear equation,

$$\int_{-1}^{+1}\frac{\left(\omega-\langle\omega\rangle_{Eqn(1.7)}\right)F(\omega)d\omega}{1+\exp(-\lambda\omega)}=0 \tag{1.14}$$

Since the average order parameter from Equation (1.7) is an estimate, the distribution error bars associated with the uncertainty in estimating the average order parameter can be evaluated from:

$$\varepsilon(\rho(\omega_i))=\left|\frac{\partial\rho(\omega_i)}{\partial\lambda}\frac{\partial\lambda}{\partial\langle\omega\rangle}\right|\varepsilon(\langle\omega\rangle)=\left|\frac{\rho(\omega_i)\omega_i}{1+\exp(\lambda\omega_i)}\left\langle\frac{\omega\left(\omega-\langle\omega\rangle_{Eqn(1.7)}\right)}{1+\exp(\lambda\omega)}\right\rangle^{-1}\right|\varepsilon(\langle\omega\rangle) \tag{1.15}$$

where $\varepsilon(\rho(\omega_i))$ and $\varepsilon(\langle\omega\rangle)$ are the uncertainties in determining $\rho(\omega_i)$ and $\langle\omega\rangle$, respectively.

Information about higher odd moments of the distribution can be similarly included when applying MEM. This may be particularly useful in cases where the

lineshape of the distribution obtained from Equation (1.13) is very susceptible to small variations of the estimated average order parameter, that is, when the error bars are considerably larger in some specific ranges of frequency. It is worth noting that, in general, the inclusion of additional constraints having inherent uncertainties leads to an overall increase of the solution's uncertainty; nevertheless, including information about the third moment of the distribution may improve the solution stability for some systems.

When the values of the first M odd moments of the distribution, which can be estimated through Equation (1.8), are imposed among the constraints, the resulting distribution from MEM can be written as:

$$\rho(\omega_i) = \left[\int_{-1}^{+1} \frac{F(\omega) d\omega}{1 + \exp\left(-\sum_{k=1}^{M} \lambda_k \omega^{2k-1} \right)} \right]^{-1} \left[\frac{F(\omega_i)}{1 + \exp\left(-\sum_{k=1}^{M} \lambda_k \omega_i^{2k-1} \right)} \right] \tag{1.16}$$

where λ_k is the Lagrange multiplier associated with the constraint related with the kth odd moment. All the M Lagrange Multipliers are now obtained by solving the following system of M nonlinear equations,

$$\begin{cases} \displaystyle\int_{-1}^{+1} \frac{\left(\omega - \langle \omega \rangle_{Eqn(1.8)} \right) F(\omega) d\omega}{1 + \exp\left(-\sum_{k=1}^{M} \lambda_k \omega^{2k-1} \right)} = 0 \\ \vdots \\ \displaystyle\int_{-1}^{+1} \frac{\left(\omega^{2M-1} - \langle \omega^{2M-1} \rangle_{Eqn(1.8)} \right) F(\omega) d\omega}{1 + \exp\left(-\sum_{k=1}^{M} \lambda_k \omega^{2k-1} \right)} = 0 \end{cases} \tag{1.17}$$

Analogously, the distribution error bars associated with the uncertainty in estimating the first *M* odd moments can be written as follows:

$$\varepsilon\left(\rho\left(\omega_i\right)\right)=\sqrt{\sum_{j=1}^{M}\left[\left(\sum_{l=1}^{M}\left(\frac{\partial\rho\left(\omega_i\right)}{\partial\lambda_l}\frac{\partial\lambda_l}{\partial\left\langle\omega^{2j-1}\right\rangle}\right)\right)^2\varepsilon^2\left(\left\langle\omega^{2j-1}\right\rangle\right)\right]} \tag{1.18}$$

where $\varepsilon^2(<\omega^{2j-1}>)$ is the square of the uncertainty in determining $<\omega^{2j-1}>$. Derivative terms in Equation (1.18) can be evaluated from:

$$\frac{\partial\rho\left(\omega_i\right)}{\partial\lambda_l}\frac{\partial\lambda_l}{\partial\left\langle\omega^{2j-1}\right\rangle}=\frac{\rho\left(\omega_i\right)\omega_i^{2l-1}}{1+\exp\left(\sum_{k=1}^{M}\lambda_k\omega_i^{2k-1}\right)}\left\langle\frac{\omega^{2l-1}\left(\omega^{2j-1}-\left\langle\omega^{2j-1}\right\rangle_{Eqn(1.8)}\right)}{1+\exp\left(\sum_{k=1}^{M}\lambda_k\omega^{2k-1}\right)}\right\rangle^{-1} \tag{1.19}$$

In short, the process to obtain segment-orientation order parameter distributions from the ^{2}H-NMR spectra can be summarized as follows:

i) Estimate the magnitude of the average frequency or order parameter $|<\omega>|$ by numerically solving Equation (1.7).

ii) Calculate the Lagrange multiplier through Equation (1.14).

iii) Determine the order parameter distribution and its error bars from Equations 1.13 and 1.15, respectively.

iv) If the error bars are considerably larger in some specific ranges of frequency, include information about the third moment of the distribution (or higher moments if necessary) as follows:

   a. Estimate the magnitude of the third (or higher) moment $|<\omega^3>|$ from Equation (1.8). The signs of $<\omega^{2k-1}>$ and $<\omega>$ are the same for the distributions of interests.

b. Calculate the set of Lagrange multipliers by numerically and simultaneously solving the system of nonlinear Equations (1.17).
c. Determine the order parameter distribution and its error bars from Equations 1.16, 1.18, and 1.19.

1.3 Molecular Simulation Model and Procedures

Coarse-grained Monte Carlo simulations of polymer networks consisting of unimodal and bimodal chain length distributions were performed in order to validate, along with experimental evidence, the proposed strategy for extracting segment-orientation order parameter distributions from the ^{2}H-NMR spectra. The molecular model used in this work has been previously shown to represent well PDMS sample networks in terms of mechanical properties and network microstructure.[24] A brief description of the employed simulation procedures for the polymer end-linking reaction and uniaxial deformation is presented in the following sub-sections. Detailed information about the simulation methods can be found in reference 24 and works cited therein.

1.3.1 Network End-linking. Simulations of the end-linking reaction were carried out on a lattice in the framework of the Bond Fluctuation Model (BFM).[49] This coarse-grained scheme allows for a complete and simultaneous analysis of both static and dynamic quantities in polymeric systems.[50] Here, coarse-grained units (i.e., chain monomers and crosslinks) are modeled as cubes capable of forming bonds along any of 108 distinct bond vectors. Only excluded-volume interactions and bonding restrictions are taken into account in this model. The fraction of occupied lattice points was set between 0.46 – 0.47, a value that has been shown to resemble melt-like

conditions.[51] Chains and crosslinks were first inserted in the simulation box and then relaxed using hop moves that mimic diffusive dynamics.[50]

After the equilibration stage, which typically involved up to 10^6 moves per repeat unit, the end-linking reaction was initiated by allowing bond formation between chain ends and neighboring tetrafunctional cross-links, while the system continued being equilibrated by the hop moves. The reaction was stopped when the percentage of unreacted chain ends was 1% or lower. The ratio of crosslink arms to chain ends, r_x, used for each simulated system was chosen in order to obtain soluble fractions no greater than 0.3 mass %. The fractions of elastic material—chains that are neither single looped nor pendant—were greater than 95 mol % in the unimodal networks and greater than 75 mol % in the bimodal networks. The size of all systems was set to be approximately equal to allow for a consistent comparison of the different simulated networks. Tables 1.1 and 1.2 show the main characteristics of the resulting networks.

Table 1.1: Characteristics of the simulated set of unimodal networks

Chain length (# of beads)	r_x	Number of chains	Number of crosslinks	Sol cont. (mass%)	Elastic cont. (mol%)
15	1.05	1659	871	0.00	94.7
29	1.10	858	472	0.00	95.6
43	1.05	579	304	0.00	96.7
129	1.15	193	111	0.00	97.4

Table 1.2: Characteristics of the simulated set of (15-300-bead) bimodal networks

Short chain content(mol%)	r_x	Number of short chains	Number of Long chains	Number of crosslinks	Sol cont. (mass%)	Elastic cont. (mol%)
60	1.15	110	73	105	0.07	74.9
80	1.10	268	67	185	0.25	84.2
90	1.05	490	54	286	0.00	87.3
95	1.10	778	41	451	0.00	90.7
98	1.10	1106	21	621	0.07	92.5

1.3.2 Network Uniaxial Deformation. Monte Carlo simulations of network uniaxial extension were performed off-lattice to allow for continuous deformations of the simulation box. Network coordinates obtained from the on-lattice BFM were transformed into the continuous framework preserving the polymer volume fraction and the network structure. Both chain monomers and crosslinks were modeled as Lennard-Jones sites with diameter σ_{LJ} and interaction energy ε_{LJ}. In terms of entanglement chain lengths, each Lennard-Jones site is roughly equivalent to 300 g/mol (~4 monomers) of PDMS.[24] A purely repulsive interaction between non-bonded beads was defined through a cut-shifted Lennard-Jones potential with cutoff at $r_{cut} = 2^{1/6}\,\sigma_{LJ}$, while bond lengths were allowed to fluctuate between $0.8\sigma_{LJ}$ and $1.2\sigma_{LJ}$. Bond crossing was prevented by setting a bead-bead overlap distance ($r_0 = 0.8\sigma_{LJ}$).

Hop (bead translation), flip (bead rotation) and cluster volume (box dimensions change) moves were implemented, in random order, to equilibrate the system in a pseudo-dynamic manner.[52] All moves were grouped in cycles. One cycle, which roughly mimics one molecular dynamics step, includes a fixed number (typically equal to the total number of sites in the system) of attempted single-site moves (95% hops and 5% flips) and two volume moves.[53,54] The acceptance ratios for hop, flip and cluster volume moves were 0.30, 0.45, and 0.35, respectively. NPT Monte Carlo simulations at temperature T =2.0 (in ε_{LJ}/k_B units) and pressure P = 3.0 (in k_BT/σ_{LJ}^3 units) were performed in order to initially equilibrate the system at a melt-like density (~0.8 in $1/\sigma_{LJ}^3$ units). After equilibration (~10^6 cycles), uniaxial extension simulations were subsequently carried out in an isostress ensemble. The imposed stress is given by the difference of applied normal stresses $(P_{xx} + P_{yy})/2 - P_{zz}$, where P_{xx}, P_{yy}, and P_{zz} are the applied normal stresses in the x,y, and z directions respectively. The extension ratio was obtained from the quotient of the box z-length after the stress was imposed to the initial unperturbed box z-length. Systems were considered to be in equilibrium when their simulation box dimensions reached plateau values, which were typically achieved after 10^7 cycles.

1.3.3 Simulated ^{2}H-NMR Spectra and Order Parameter Distributions. As previously mentioned in Section 1.2.1 (Equation 1.4), under certain conditions, generally satisfied for ^{2}H-NMR measurements in polymeric systems, the ^{2}H-NMR spectrum $F(\omega)$ can be written as the symmetrized distribution of the time-averaged order parameter $\rho(\omega)$.[16] The simulated spectrum can therefore be directly calculated from the order parameter distribution obtained from brute force simulations.[16,17,22]

After a (simulated) deformed network reached equilibrium, statistics for each chain segment were taken at every 40 cycles during an additional run of approximately 3×10^7 cycles. At the end of this additional run, the time-averaged order parameter (over the entire additional run) or frequency splitting $\delta\omega$ is calculated separately for each chain segment. The frequency spectrum $F(\omega)$ was obtained from normalizing (by area) an occurrence histogram constructed by adding 1 to the bins corresponding to both $+\delta\omega/2$ and $-\delta\omega/2$ for every chain segment in the system; conversely, the distribution or histogram of the order parameter $\rho(\omega)$ was the result of adding 1 only to the bin corresponding to $\delta\omega/2$ for all the segments. The width of the bins ranged between 0.002 and 0.004.

1.4 Results and Discussions

1.4.1 Validating the Estimate of the Average Order Parameter. Segment-orientation measurements from both brute force simulations and experimental ^{2}H-NMR are used to evaluate the performance of Equation (1.7) and (1.8) in predicting the magnitudes of the first and higher odd moments of the order parameter distribution.

A direct comparison between the simulated results and estimations from Equation (1.7) can be made since both the average order parameter and its average absolute value can be calculated in a straightforward manner in simulations. Analogously, direct comparisons can also be made to test the accuracy of Equation (1.8). Figure 1.2 shows the result of such comparisons. In Figure 1.2a we can observe that Equation (1.7) predicts rather well the dependence of the (scaled) average order parameter on the (scaled) average absolute value of the order parameter for the

simulated results. The mean percentile deviation for all the simulated systems is around 5%. In general, Equation (1.7) tends to slightly overpredict the average order parameter, yet its observed accuracy increases with the length of the polymer chain. For example, in the unimodal networks made with chains of 15, 29, 43, and 129 beads, the mean percentile deviations of Equation (1.7) are 10%, 4%, 2.5%, and 0.5%, respectively. Similarly, for the results of a set of bimodal networks (consisting of chains with 15 and 300 beads) the mean percentile deviations for the short and long chains are 8% and 2%, correspondingly. This accuracy dependence on the chain length is not surprising because longer chains exhibit segment-orientation distributions with less skewness upon deformation (evidenced by a milder spectrum broadening), which favors the applicability of the translation invariance approximation for "small" deformations that was assumed in Section 1.2.2. This suggests that for segments of non-Gaussian (or relatively short) chains the difference $\Re$ decays with the average at a slower rate than the exponential approximation. From Figure 1.2b analogous results are obtained for the performance of Equation (1.8) when predicting magnitudes of the third and fifth moments of the order parameter distribution. However, when estimating higher odd moments the noise of the frequency spectrum is also amplified, which leads to an additional increase of uncertainty in the estimation of such moments.

Although the predictions of Equation (1.7) cannot be directly compared with experimental results, indirect quantitative comparisons, based on theoretical relations, may be performed to evaluate the quality of the predictions. Specifically, we know from classical theory of rubber elasticity[2,3] and from experimental evidence[15] that the average orientation order parameter is proportional to Young's modulus E and the network deformation term $\alpha^2 - \alpha^{-1}$, where α is the extension ratio. Then, the reduced

frequency [$<\nu>$], defined below, is expected to be very similar for polymer networks made of the same chemical monomer.[3]

$$\left[\langle\nu\rangle\right] = \frac{\langle\nu\rangle / E}{\alpha^2 - \alpha^{-1}} \tag{1.20}$$

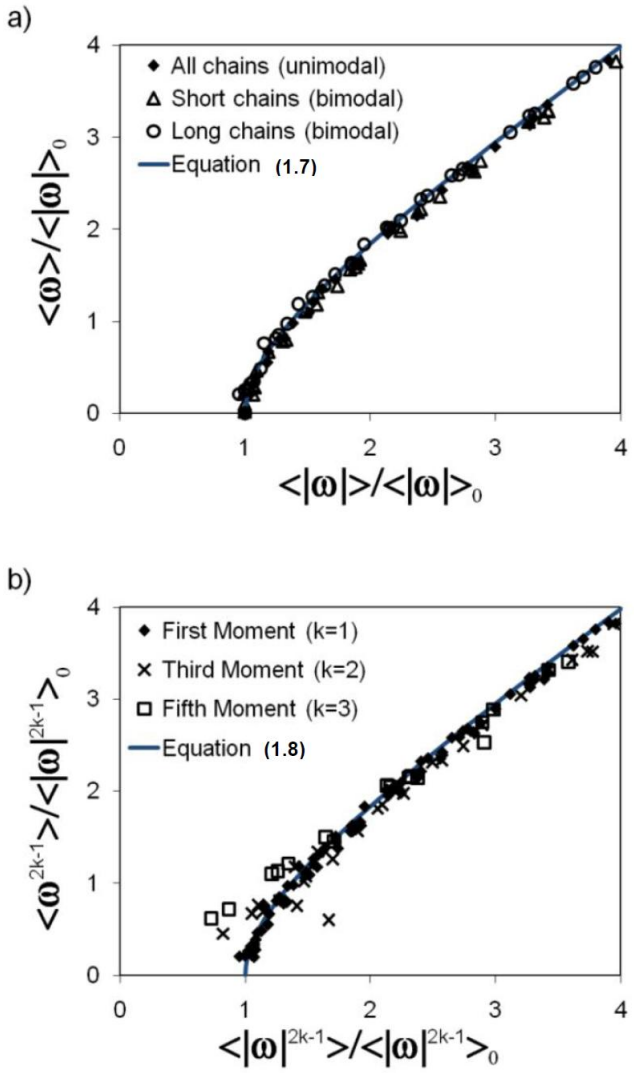

Figure 1.2: Comparison between predicted (curves) and simulated (symbols) average odd moments for the sets of unimodal and bimodal networks. a) Scaled average values vs. scaled average absolute values of the order parameter distribution. b) Scaled odd moments vs. scaled average absolute odd moments of the order parameter distribution.

Figure 1.3a shows the expected linear dependence of the estimated average frequency $<\nu>$ on the extension term $\alpha^2-\alpha^{-1}$ for a nearly unimodal PDMS end-linked network with chains having number-average molar mass of 36 kg/mol.[25] Moreover, Figure 1.3b depicts the comparison between the predicted values for the total reduced frequencies [$<\nu>$] in several bimodal PMDS networks and the 36-kg/mol-unimodal network. For all bimodal networks, total reduced frequencies are calculated as the mass-weighted averages of the reduced frequencies of short and long chains. Predicted reduced frequencies [$<\nu>$] are rather similar for all the studied networks regardless of the differences in chain polydispersity. All the bimodal networks were the result of end-linking two sets of chains with number-average molar mass of 5.0-4.5 kg/mol and 90-80 kg/mol in different proportions. The synthesis of the different deuterated systems and ^{2}H-NMR measurements were performed by Genesky et al.[25,46] From Figure 1.3 we can infer that the estimates of the average order parameter obtained from Equation (1.7) agree relatively well with the predictions of classical theory of rubber elasticity.

Altogether, these results and those for the direct comparisons with simulated networks suggest that the proposed methodology to estimate the average order parameter (and higher odd moments of the distribution) from spectral data can be used quantitatively within a rather acceptable range of uncertainty (5% to 10%).

1.4.2 Validating the Estimated Order Parameter Distribution. Here order parameter distributions extracted by interpreting spectral data through MEM are compared with the corresponding distributions obtained from brute force Monte Carlo simulations. The system used for the comparisons is a bimodal network, which exhibits considerably high degree of heterogeneity in its segment-orientation

responses of the short and long chains. This bimodal network consists of 90 mol% of 15-bead (short) chains and 10 mol% of 300-bead (long) chains. More information about this network can be found in Table 1.2. Figure 1.4 illustrates good agreement between the distributions obtained from simulations and their estimates calculated through MEM for both short and long chains in the network stretched to α=2.15. Only information about the first moment was used in these comparisons. Error bars are calculated assuming a 5% of uncertainty in the $<\omega>$ estimation. As expected from the assumptions made in Section 1.2.2, the accuracy of the distribution estimates also increases with chain length.

The observed (dimensionless) frequency splitting for both types of chains in the network is in the order of 2×10^{-2}, whereas the average frequency (or order parameter) for the short and long chains are 5.27×10^{-2} and 2.30×10^{-2}, respectively. For comparison, the estimates from Equation (1.7) of the average order parameters for the short and long chains of this system are 5.5×10^{-2} and 2.3×10^{-2}, and the corresponding predicted values of the average order parameters obtained from fitting spectral data to the mean-field-based Gaussian network model of Ries et al. (Equations 9 & 10 of reference 19) are 12.9×10^{-2} and 1.77×10^{-2}. As the model presented by Ries et al. involves ideal chain statistics, specifically affine deformation, important deviations are expected for the short chains of 14 segments since they exhibit a pronounced non-Gaussian behavior.

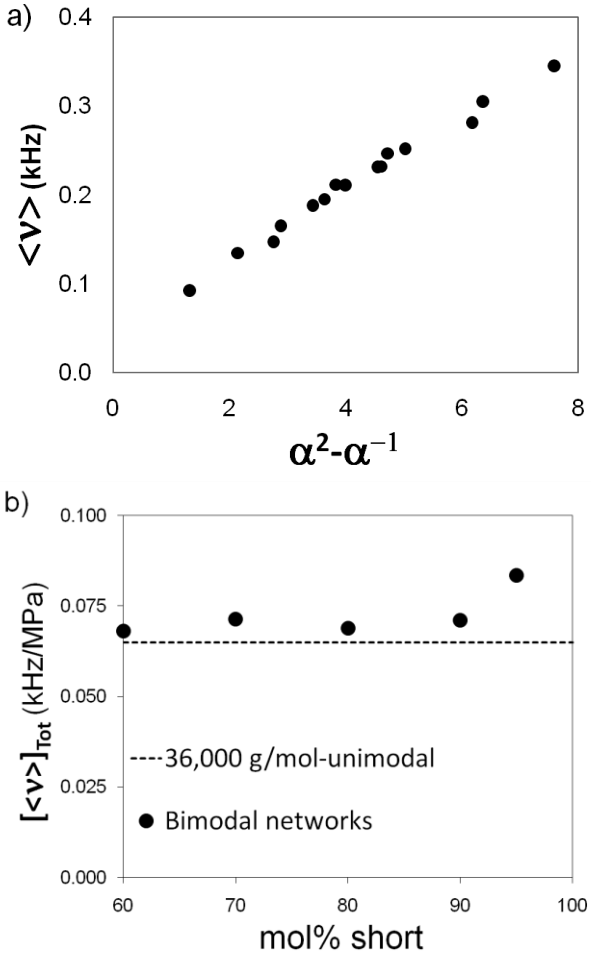

Figure 1.3: Estimates of the average frequency and the total reduced frequency for PDMS networks. a) Estimated average frequency (Equation (1.7)) vs. extension for the 36-kg/mol-unimodal PDMS network. b) Estimated total reduced frequency for the 36-kg/mol-unimodal PDMS network (dashed line) and several (5.0/4.5-90/80 kg/mol) bimodal PDMS networks with different molar content of short chains (solid circles).

Another interesting feature of this bimodal network is that the large difference in the orientation response among the different chains in the network is not captured well by the observed splittings, and is clearly evidenced by the distinct spectra lineshapes. Such a difference in the orientation response between the short and long chain segments is attributed to the fact that short chains are significantly more stretched than their longer counterparts in certain bimodal networks.[23,24] It is important

to stress that these types of systems represent a good example of the potential applicability of the advocated methodology to quantitatively characterize the orientational behavior in polymer networks with heterogeneous orientation responses from the conventional ^{2}H-NMR measurements.

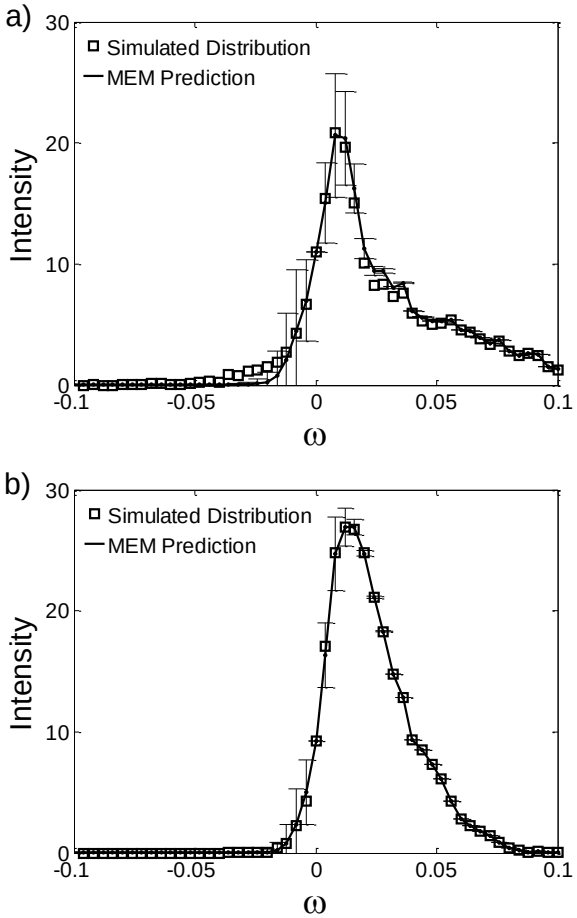

Figure 1.4: Comparison between order parameter distributions directly obtained from molecular simulations (empty squares) and their corresponding MEM predictions (solid lines) for a simulated bimodal network consisting of 90 mol% of 15-bead chains and 10 mol% of 300-bead chains when α=2.15. a) Orientation order parameter distributions (simulated and predicted) for the short (15-bead) chains. b) Orientation order parameter distributions (simulated and predicted) for the long (300-bead) chains.

1.4.3 Application to an Experimental PDMS Network. By means of the proposed method, frequency splitting distributions are estimated, from their corresponding ^{2}H-NMR spectra, for the 36-kg/mol-unimodal PDMS network[25] at low and high uniaxial deformations. Figure 1.5 shows the ^{2}H-NMR frequency spectrum and the predicted frequency distribution of this unimodal PDMS network at extension ratio α=1.42; only information about the first moment was used. Although the quadrupolar splitting is not clearly visible in the spectrum at such moderate deformation, the observed frequency splitting, in addition to the average splitting, can be determined from the predicted distribution. Interestingly, when this 36-kg/mol-unimodal PDMS network is greatly stretched (α=2.56), its ^{2}H-NMR spectrum (Figure 1.6) shows a clear and unusual shoulder, that is, two characteristic quadrupolar splittings are observed.[25] The existence of these two splittings at high extensions may be attributed to a great disparity in the chain end-to-end distance distribution which could lead to such heterogeneous orientation response within the network. Figure 1.6a shows the estimated frequency distribution when only information about the first moment or average of the distribution is included. All error bars are calculated assuming a 5% of uncertainty in the $<\nu>$ estimation. The solution distribution yielded by MEM for this complex lineshaped-spectrum seems very sensitive to small variations of the estimated average; in order to improve the stability of the solution, information about its third moment was also included in MEM. The result of this second attempt is shown in Figure 1.6b where a significant improvement in the distribution stability is observed for this complex spectrum; however, if information about the fifth moment is included as well, the resulting error bars in the distribution

are much larger and the distribution lineshape is less smooth in some frequency ranges (not shown). In this case then, the first and third moments provide the amount of information that optimizes stability of the solution distribution.

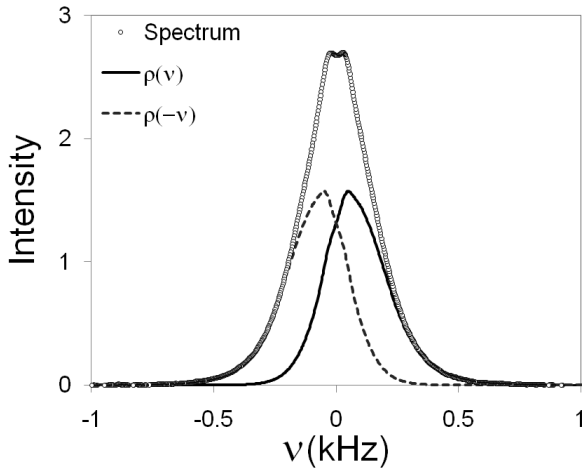

Figure 1.5: Frequency spectrum (empty circles) and its decomposition into the predicted frequency distribution (solid line) and its mirror image (dashed line), for the 36-kg/mol-unimodal PDMS network when α=1.42.

As illustrated with this last system, another instance wherein the proposed methodology of estimating segment-orientation distributions may be especially advantageous is in interpreting ^{2}H-NMR spectral data of systems exhibiting complex spectra, which cannot be trivially analyzed through the conventional treatment of multi-parameter fitting of spectral data to ideal-chain-like models.

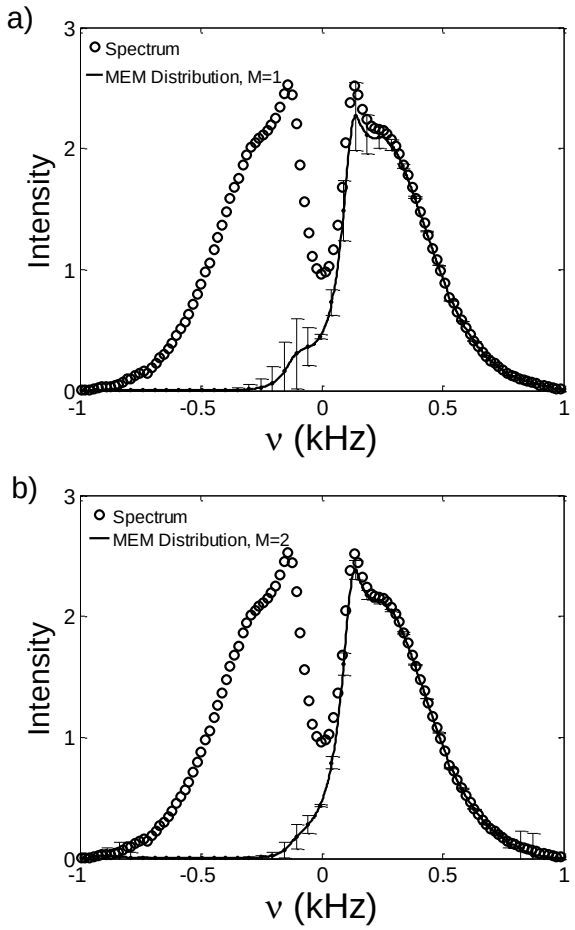

Figure 1.6: Frequency spectrum (empty circles) and the predicted frequency distributions (solid lines), for the 36-kg/mol-unimodal PDMS network when α=2.56. a) MEM prediction using information about the first moment only (Equation 1.16 with M=1). b) MEM prediction using information about the first and third moments (Equation 1.16 with M=2).

1.5 Conclusions

An analytical expression was derived, based on suitable Taylor expansions, to estimate the magnitude of the average order parameter and higher odd moments from spectral data (i.e., from average absolute values of the order parameter or average absolute moments). It was found through comparisons with simulated and experimental results that the derived expression can estimate the average order parameter within an acceptable range of uncertainty (5% to 10%), whose accuracy increases for systems showing more completely averaged spectra (e.g., networks

consisted of "long" chains). The latter is due to the translation invariance approximation for "small" deformations used in Section 1.2.2 when deriving the estimate for the average order parameter.

In principle, the accuracy of the estimation of the average order parameter for networks containing "too short" chains could be improved by using more flexible schemes, but at the expense of losing generality. For example, one could Taylor-expand a different function of $\mathfrak{R}$, instead of $\ln(1/\mathfrak{R})$, that allows for tuning how fast $\mathfrak{R}$ decays with the average. For instance, by choosing $1/\mathfrak{R}^h$, the free parameter h would modulate the decay of $\mathfrak{R}$; and for a given set of data, the most appropriate value of h could be found such that one observes the expected dependence of the average order parameter $<\nu>$ on $\alpha^2-\alpha^{-1}$ (i.e., linear and with very small or null intercept).

Based on the maximum-entropy method, an alternative strategy for interpreting the ^{2}H-NMR spectral data was developed. This simple and computationally inexpensive strategy, which requires the numerical solution of a few nonlinear equations only, is capable to accurately extract distributions of the segmental orientation order parameter from the conventionally measured ^{2}H-NMR spectra. The proposed methodology can be especially advantageous when applied to polymer networks exhibiting highly heterogeneous segmental orientation responses and complex ^{2}H-NMR spectrum lineshapes. Such systems may not be appropriately analyzed through the conventional treatments—multi-parameter fitting of spectral data to ideal-chain-mean-field-like models or solely measuring the observed quadrupolar splittings.

1.6 Acknowledgments

This work was supported by the National Science Foundation Polymers Program under grant DMR-0705565. We thank T. Michael Duncan and Geoffrey D. Genesky for helpful discussions and providing the critical ^{2}H-NMR spectral data of the PDMS networks.

1.A Appendix

1.A.1 Derivation of Equation (1.8). The average absolute values of odd powers of the order parameter $\langle|\omega|^{2k-1}\rangle$ (with k=1,2,…,*M*) can be calculated from spectral data as follows

$$\left\langle |\omega|^{2k-1} \right\rangle = \int_{-1}^{+1} |\omega|^{2k-1} \rho(\omega) d\omega = \frac{\int_{-1}^{+1} |\omega|^{2k-1} F(\omega) d\omega}{\int_{-1}^{+1} F(\omega) d\omega} \tag{1.A-1}$$

Let $\Re_{2k-1}$ be defined as the difference between $\langle|\omega|^{2k-1}\rangle$ and $|\langle\omega^{2k-1}\rangle|$. Then, $\Re_{2k-1}$ can then be written in terms of $\rho(\omega)$ as:

$$\Re_{2k-1} = \left\langle |\omega|^{2k-1} \right\rangle - \left| \left\langle \omega^{2k-1} \right\rangle \right| = \begin{cases} 2\int_{-1}^{0} \left(-\omega^{2k-1}\right) \rho(\omega) d\omega & \text{if } \left\langle \omega^{2k-1} \right\rangle \geq 0 \\ 2\int_{0}^{+1} \omega^{2k-1} \rho(\omega) d\omega & \text{if } \left\langle \omega^{2k-1} \right\rangle < 0 \end{cases} \tag{1.A-2}$$

Subsequently, $\ln(1/\Re_{2k-1})$ is Taylor expanded around the unperturbed state, $|\langle\omega^{2k-1}\rangle| = |\langle\omega^{2k-1}\rangle|_0$, assuming first that all segments are isotropically distributed when the sample is unstretched (i.e., $|\langle\omega^{2k-1}\rangle|_0 = 0$ and $|\langle\omega\rangle|_0 = 0$), and second that $\rho(\omega)$ can be reasonably approximated by translating the distribution at the unstretched state

$\rho_0(\omega)$ when $|<\omega>-<\omega>_0|$ (or equivalently $|<\omega^{2k-1}>-<\omega^{2k-1}>|_0$) is "small enough", i.e., $\rho(\omega) \cong \rho_0(\omega-<\omega>+<\omega>_0)$. After some algebraic manipulations of the aforementioned the Taylor expansion, the following expressions result:

If $<\omega^{2k-1}> \geq 0$,

$$-\ln\left(\frac{\Re_{2k-1}}{\left\langle|\omega|^{2k-1}\right\rangle_0}\right) = -\frac{\left\langle\omega^{2k-1}\right\rangle}{\left\langle|\omega|^{2k-1}\right\rangle_0}\frac{d\langle\omega\rangle}{d\left\langle\omega^{2k-1}\right\rangle}\bigg|_0 \frac{d}{d\langle\omega\rangle}\left(2\int_{-1-<\omega>}^{-<\omega>} -\left(\omega+\langle\omega\rangle\right)^{2k-1}\rho_0(\omega)d\omega\right)\bigg|_0 \qquad \text{(1.A-3a)}$$

And, if $<\omega^{2k-1}> < 0$,

$$-\ln\left(\frac{\Re_{2k-1}}{\left\langle|\omega|^{2k-1}\right\rangle_0}\right) = -\frac{\left\langle\omega^{2k-1}\right\rangle}{\left\langle|\omega|^{2k-1}\right\rangle_0}\frac{d\langle\omega\rangle}{d\left\langle\omega^{2k-1}\right\rangle}\bigg|_0 \frac{d}{d\langle\omega\rangle}\left(2\int_{-<\omega>}^{1-<\omega>} \left(\omega+\langle\omega\rangle\right)^{2k-1}\rho_0(\omega)d\omega\right)\bigg|_0 \qquad \text{(1.A-3b)}$$

The subscript "0" denotes that the evaluations of the expressions have to be at the unstretched state (that is, when $|<\omega>|=0$ and $|<\omega^{2k-1}>|=0$). The derivatives of the integrals in Equations (1.A-3) can be evaluated by the application of the Leibniz integral rule or the Reynolds transport theorem for one dimension; in this step we also assume that $\rho_0(\pm 1)=0$, and the results are $\pm$ (2k-1) $<-\omega^{2k-2}>_0$, respectively. The derivative of $<\omega>$ with respect to $<\omega^{2k-1}>$ is obtained from the following binomial expansion

$$\frac{d\left\langle\left(\omega-\langle\omega\rangle\right)^{2k-1}\right\rangle}{d\langle\omega\rangle}\bigg|_0 = \frac{d}{d\langle\omega\rangle}\left(\sum_{i=0}^{2k-1}\frac{(2k-1)!}{(i)!(2k-1-i)!}\left\langle\omega^{2k-1-i}\right\rangle\langle\omega\rangle^i\right)\bigg|_0 \qquad \text{(1.A-4a)}$$

After isolating the term involving $<\omega^{2k-1}>$ and evaluating at the unperturbed state the polynomial terms, we find

$$\left.\frac{d\langle\omega\rangle}{d\left\langle\omega^{2k-1}\right\rangle}\right|_0 = \left((2k-1)\left\langle\omega^{2k-2}\right\rangle_0 + \left.\frac{d\left\langle\left(\omega-\langle\omega\rangle\right)^{2k-1}\right\rangle}{d\langle\omega\rangle}\right|_0 \right)^{-1} \tag{1.A-4b}$$

At this point we invoke our translation invariance approximation, i.e., $\rho(\omega) \cong \rho_0(\omega - \langle\omega\rangle)$, which also implies that all central moments should not change significantly around $|\langle\omega\rangle|_0 \cong 0$ (as the resulting entire distribution is reasonably well described by just a small translation of the distribution of the reference state); as a result this approximation implies that

$$\left| \left.\frac{d\left\langle\left(\omega-\langle\omega\rangle\right)^{2k-1}\right\rangle}{d\langle\omega\rangle}\right|_0 \right| << (2k-1)\left\langle\omega^{2k-2}\right\rangle_0 \tag{1.A-5}$$

Equation (1.A-5) explains the statement on Section 1.2.2 about the dependence of the accuracy of the translation invariance approximation on the skewness (or asymmetry) of the distribution upon deformation. Spectral data from networks containing relatively short chains are more likely to poorly satisfy Equation (1.A-5), as severe spectrum broadening upon sample deformation is a manifestation of considerable changes of the central odd moments.

The next step is to substitute Equations (1.A-5), (1.A-4b), and the resulting derivatives of the integrals into Equations (1.A-3). After simplifying, Equations (1.A-3) can be rewriting as

$$-\ln\left(\frac{\Re_{2k-1}}{\left\langle|\omega|^{2k-1}\right\rangle_0}\right) \cong \begin{cases} \dfrac{\left\langle\omega^{2k-1}\right\rangle}{\left\langle|\omega|^{2k-1}\right\rangle_0} & \text{if } \left\langle\omega^{2k-1}\right\rangle \geq 0 \\ -\dfrac{\left\langle\omega^{2k-1}\right\rangle}{\left\langle|\omega|^{2k-1}\right\rangle_0} & \text{if } \left\langle\omega^{2k-1}\right\rangle < 0 \end{cases} \tag{1.A-6}$$

Finally, Equation (1.A-6) can be rearranged and condensed to obtain Equation (1.8):

$$\frac{\left\langle |\omega|^{2k-1} \right\rangle}{\left\langle |\omega|^{2k-1} \right\rangle_0} \cong \frac{\left| \left\langle \omega^{2k-1} \right\rangle \right|}{\left\langle |\omega|^{2k-1} \right\rangle_0} + \exp\left(- \frac{\left| \left\langle \omega^{2k-1} \right\rangle \right|}{\left\langle |\omega|^{2k-1} \right\rangle_0} \right) \tag{1.8}$$

REFERENCES

(1) Rubinstein, M.; Colby, R. H. *Polymer Physics*; Oxford University Press, USA, 2003.

(2) Flory, P. J. *Principles of Polymer Chemistry*; Cornell University Press, 1953.

(3) Mark, J. E.; Erman, B. *Rubberlike Elasticity: A Molecular Primer*; Wiley: New York, 1988; p. 196.

(4) Mark, J. E. *Progress in Polymer Science* **2003**, *28*, 1205-1221.

(5) Deloche, B.; Samulski, E. T. *Macromolecules* **1981**, *14*, 575-581.

(6) Deloche, B.; Dubault, A.; Herz, J.; Lapp, A. *EPL (Europhysics Letters)* **1986**, *1*, 629-635.

(7) Sotta, P.; Deloche, B.; Herz, J.; Lapp, A.; Durand, D.; Rabadeux, J. C. *Macromolecules* **1987**, *20*, 2769-2774.

(8) Sotta, P.; Deloche, B. *Macromolecules* **1990**, *23*, 1999-2007.

(9) Kornfield, J. A.; Chung, G. C.; Smith, S. D. *Macromolecules* **1992**, *25*, 4442-4444.

(10) Sotta, P. *Macromolecules* **1998**, *31*, 3872-3879.

(11) Hedden, R. C.; McCaskey, E.; Cohen, C.; Duncan, T. M. *Macromolecules* **2001**, *34*, 3285-3293.

(12) Hedden, R. C.; Tachibana, H.; Duncan, T. M.; Cohen, C. *Macromolecules* **2001**, *34*, 5540-5546.

(13) Callaghan, P. T.; Samulski, E. T. *Macromolecules* **2003**, *36*, 724-735.

(14) Batra, A.; Hedden, R. C.; Schofield, P.; Barnes, A.; Cohen, C.; Duncan, T. M. *Macromolecules* **2003**, *36*, 9458-9466.

(15) Chapellier, B.; Deloche, B.; Oeser, R. *J. Phys. II* **1993**, *3*, 1619-1631.

(16) Depner, M.; Deloche, B.; Sotta, P. *Macromolecules* **1994**, *27*, 5192-5199.

(17) Sotta, P.; Higgs, P. G.; Depner, M.; Deloche, B. *Macromolecules* **1995**, *28*, 7208-7214.

(18) Jacobi, M. M.; Abetz, V.; Stadler, R.; Gronski, W. *Polymer* **1996**, *37*, 1669-1675.

(19) Ries, M. E.; Brereton, M. G.; Klein, P. G.; Ward, I. M.; Ekanayake, P.; Menge, H.; Schneider, H. *Macromolecules* **1999**, *32*, 4961-4968.

(20) Edwards, S. F.; McLeish, T. C. B. *J. Chem. Phys.* **1990**, *92*, 6855-6857.

(21) Brereton, M. G. *Macromolecules* **1993**, *26*, 1152-1157.

(22) Yong, C. W.; Higgs, P. G. *Macromolecules* **1999**, *32*, 5062-5071.

(23) Saalwächter, K.; Ziegler, P.; Spyckerelle, O.; Haidar, B.; Vidal, A.; Sommer, J. *J. Chem. Phys.* **2003**, *119*, 3468-3482.

(24) Genesky, G. D.; Aguilera-Mercado, B. M.; Bhawe, D. M.; Escobedo, F. A.; Cohen, C. *Macromolecules* **2008**, *41*, 8231-8241.

(25) Genesky, G. D.; Duncan, T. M.; Cohen, C. *Macromolecules* **2009**, *(submitted concurrently)*.

(26) Saalwächter, K.; Kleinschmidt, F.; Sommer, J. *Macromolecules* **2004**, *37*, 8556-8568.

(27) Saalwächter, K.; Sommer, J. *Macromolecular Rapid Communications* **2007**, *28*, 1455-1465.

(28) Saalwächter, K. *Progress in Nuclear Magnetic Resonance Spectroscopy* **2007**, *51*, 1-35.

(29) Gjersing, E.; Chinn, S.; Giuliani, J. R.; Herberg, J.; Maxwell, R. S.; Eastwood, E.; Bowen, D.; Stephens, T. *Macromolecules* **2007**, *40*, 4953-4962.

(30) Weese, J. *Computer Physics Communications* **1992**, *69*, 99-111.

(31) Tikhonov, A. N.; Arsenin, V. Y. *Solutions of Ill-Posed Problems*; Winston: Washington, 1977; p. 258.

(32) Schäfer, H.; Stannarius, R. *Journal of Magnetic Resonance, Series B* **1995**, *106*, 14-23.

(33) Winterhalter, J.; Maier, D.; Grabowski, D. A.; Honerkamp, J.; Muller, S.; Schmidt, C. *J. Chem. Phys.* **1999**, *110*, 4035-4046.

(34) Schäfer, H.; Mädler, B.; Sternin, E. *Biophysical Journal* **1998**, *74*, 1007-1014.

(35) van Beek, J. D.; Meier, B. H.; Schäfer, H. *Journal of Magnetic Resonance* **2003**, *162*, 141-157.

(36) Wendlandt, M.; van Beek, J. D.; Suter, U. W.; Meier, B. H. *Macromolecules* **2005**, *38*, 8372-8380.

(37) Jaynes, E. T. *Phys. Rev.* **1957**, *106*, 620.

(38) Jaynes, E. T. *Phys. Rev.* **1957**, *108*, 171.

(39) Jaynes, E. T. *Probability Theory: The Logic of Science*; Bretthorst, G. L., Ed.; Cambridge University Press: Cambridge, UK, 2003; p. 727.

(40) Brown, W.; Johnsen, R.; Stepanek, P.; Jakes, J. *Macromolecules* **1988**, *21*, 2859-2865.

(41) Runge, A. F.; Saavedra, S. S.; Mendes, S. B. *J. Phys. Chem. B* **2006**, *110*, 6721-6731.

(42) Berardi, R.; Spinozzi, F.; Zannoni, C. *J. Chem. Phys.* **1998**, *109*, 3742-3759.

(43) Sakakibara, D.; Sasaki, A.; Ikeya, T.; Hamatsu, J.; Hanashima, T.; Mishima, M.; Yoshimasu, M.; Hayashi, N.; Mikawa, T.; Walchli, M.; Smith, B. O.; Shirakawa, M.; Guntert, P.; Ito, Y. *Nature* **2009**, *458*, 102-105.

(44) Thaning, J.; Stevensson, B.; Östervall, J.; Naidoo, K. J.; Widmalm, G.; Maliniak, A. *J. Phys. Chem. B* **2008,** *112*, 8434-8436.

(45) Chiang, Y.; Borbat, P. P.; Freed, J. H. *Journal of Magnetic Resonance* **2005,** *177*, 184-196.

(46) Genesky, G. D.; Aguilera-Mercado, B. M.; Escobedo, F. A.; Cohen, C.

Macromolecules **2009,** (*in preparation).*

(47) Cohen-Addad, J. P. *J. Chem. Phys.* **1974,** *60,* 2440-2453.

(48) Cohen-Addad, J. P.; Domard, M.; Herz, J. *J. Chem. Phys.* **1982,** *76,* 2744-2753.

(49) Carmesin I.; Kremer K. *Macromolecules* **1988,** *21,* 2819.

(50) Binder K.; Paul W. *J. Polym. Sci., Polym. Phys.* **1997,** *35,* 1.

(51) Paul W.; Binder K.; Heermann D.; Kremer K. *J. Phys. II* **1991,** *1,* 37.

(52) Escobedo, F. A.; de Pablo, J. J. *J. Chem. Phys.* **1997,** *106,* 793-810.

(53) Chen, Z.; Cohen, C.; Escobedo, F. A. *Macromolecules* **2002,** *35,* 3296-3305.

(54) Bhawe, D. M.; Cohen, C.; Escobedo, F. A. *Macromolecules* **2004,** *37,* 3924-3933.

CHAPTER 2

^{2}H-NMR AND SIMULATION STUDIES OF CHAIN SEGMENT ORIENTATION IN PDMS BIMODAL NETWORKS*

2.0 Abstract

We present a systematic study through ^{2}H-NMR and molecular simulations of chain-segment orientation in model PDMS bimodal networks. Estimates of the average segment orientation order parameter in model PDMS bimodal networks compare well to those of equivalent simulated networks. We find that lineshapes of short and long chains are different due to the dissimilar degrees of motional restrictions. Short chain conformations are perturbed from random coiled states when incorporated into bimodal networks whereas long chain conformations are unaffected. Although experiments and simulations both indicate that the overall segment orientation normalized by the elastic modulus is fairly constant across all bimodal network compositions, short-chain normalized segment orientation displays a non-monotonic trend with the network composition (related to changes in network microstructure and mechanical properties). Finally, we show that the unusual outer splittings observed in spectra of highly extended unimodal and bimodal samples correspond to segments in long chains able to be exceptionally stretched and oriented along the strain axis.

2.1 Introduction

Bimodal polymer networks have attracted interest due to their interesting mechanical properties.[1] These elastomers are synthesized from chemically-identical telechelic chains of two different molar masses. When these precursor chain lengths

* Reprinted with permission from Aguilera-Mercado, B. M.; Genesky, G. D.; Cohen, C.; Escobedo, F. A. *Macromolecules* **2010**, *43*, 7173-7184. Copyright 2010 American Chemical Society. This chapter makes extensive use of experimental observations and their corresponding analyses reported in Genesky, G. D., Ph.D. Thesis, Cornell University, Ithaca, New York, 2009.

are widely separated, the end-linked networks require increased energy to rupture (toughness) and stress increases markedly at high elongation.[2] The connection between these interesting macroscopic properties and the conformations of the network chains has long been a matter of debate. For instance, some researchers have claimed that the short chains cluster into heterogeneous domains which could toughen networks, like filler particles toughen commercial rubbers.[3,4] The ability of short chains to segregate in such systems has been confirmed using a variety of methods,[3,5-7] but a connection between this microstructure and an enhancement in mechanical properties has not been demonstrated. Others have attributed the improved mechanical properties of bimodal networks to the finite extensibility of the short chains when the network is highly elongated.[2,8-10] In this hypothesis, the highly stretched short chains increase the stress abruptly, while the more moderately extended long chains allow the network to strain highly before fracturing.

Studies of chain segment orientation with increasing elongation ratio α are valuable in illuminating structure-property relationships in bimodal networks. ^{2}H-NMR is a powerful method to investigate these network properties at local scales because the NMR frequency spectrum $f(\nu)$ is determined by the distribution of the chain segment orientation order parameter S. In the polydimethylsiloxane (PDMS) chains studied here, the CH_3 side groups are selectively replaced by $C(^2H)_3$ groups. Chain segment orientation is monitored through the deuterium quadrupole interaction between the electrostatic field gradient along the labeled C-^{2}H bonds. The resulting lineshape of an unstrained elastomer is broader than the lineshape of a melt but much narrower than that of a rigid solid. As the network is uniaxially extended, motional averaging of the quadrupole interaction is constrained due to the anisotropic

orientation of chain segments and the spectra broaden. The lineshape eventually forms two symmetric peaks (which represent the most frequently accessed degree of time-averaged segment orientation) separated by distance $\Delta\nu$. Both experiments and models have shown that these peaks result from inter-chain excluded volume interactions.[11-14]

Given the interest in the structure and properties of bimodal networks and the ability of ^{2}H-NMR experiments to monitor either the short or long chains through selective labeling, relatively few ^{2}H-NMR studies have been performed on this type of elastomer. Chapellier et al.[15,16] and Sotta[17] selectively labeled 3000 and 25000 g/mol PDMS chains and monitored the peak splittings $\Delta\nu$, concluding that the short and long chain segments experienced similar orientation with increasing strain. However, bimodal networks have been found to display enhanced mechanical properties only when the precursor molar masses differ by at least a factor of 10.[8,9] The relatively small (~8x) difference in molar masses employed by these authors may have not been sufficient to correlate segmental orientation with macroscopic properties in bimodal elastomers.

Other experimental methods have also been used to probe chain segment orientation in bimodal networks. Stress-optical studies have noted non-linearity in plots of birefringence vs. stress.[18-20] This effect becomes more pronounced with increasing short chain concentration, suggesting changes in spatial heterogeneity with composition.[19] Infrared dichromism studies have found a similar degree of segment orientation for the short and long chains in polytetrahydrofuran networks,[21] but an increased ordering for the short chains when they occupy a majority of the volume of a bimodal PDMS network.[22] Monte Carlo (MC) simulations have also found a higher degree of segmental order.[23] More recently, multiple quantum (MQ) NMR has been

utilized to elucidate the distribution function of local chain order in elastomers.[24] This method reveals that the distribution has two components for bimodal networks in the unstretched state,[7,25] suggesting a heterogeneous structure brought about by the differences in precursor chain lengths. However, MQ-NMR spectroscopy has yet to be applied to uniaxially stretched bimodal networks to monitor chain segment orientation of each component with strain.

Herein we present a systematic study, through ^{2}H-NMR and molecular simulations, of chain segment orientation in model PDMS bimodal networks. These well characterized elastomers contain selectively deuterated short or long chains to monitor the degree of chain segment orientation of each component in both the unstrained and highly stretched states. Although the spectra for stretched networks split into two peaks symmetric around $\nu = 0$, the segment orientation is not well described by these peak locations.[26] Therefore, we utilize a recently developed theoretical strategy[27] to estimate the average frequency $\langle\nu\rangle$ from ^{2}H-NMR spectral data for both short and long chains upon uniaxial extension. The ensemble average frequency $\langle\nu\rangle$ is over the frequency probability distribution, rather than the ^{2}H-NMR spectrum, and is directly proportional to the average segmental alignment; this average frequency $\langle\nu\rangle$ describes more accurately (than solely the frequency splittings $\Delta\nu$) the widening of the lineshape and the overall segment orientation.[27] Estimates of the average segmental alignment $\langle\nu\rangle$ in model PDMS bimodal networks are compared to averages of segmental order $\langle S\rangle$ in roughly equivalent simulated bimodal elastomers. Variations in the ^{2}H-NMR response at different bimodal compositions are closely related to changes in the network microstructure and the resulting macroscopic

mechanical properties. Additionally, we investigate in more detail ^{2}H-NMR spectra of unimodal and bimodal samples uniaxially stretched to high extension ratios that exhibit a peculiar shoulder in the lineshape, that is, two characteristic quadrupolar splittings;[28] through molecular simulations we explore the microstructural nature of these unusual two splittings.

2.2 Experimental and Simulation Methods

2.2.1 Experimental Procedures. Both hydrogenated and randomly deuterated PDMS precursor chains were synthesized using methods detailed in an earlier publication.[29] Number average molar masses were determined to be 5500 (^{1}H), 80000 (^{1}H), 5000 (^{2}H), and 90000 (^{2}H) g/mol by gel permeation chromatography (GPC). These chains were combined into 5000-80000 and 5500-90000 g/mol selectively labeled bimodal blends at the desired compositions (60-98 mol % short chains). We also used 11000 (^{2}H), 30000 (^{1}H, ^{2}H), and 36000 (^{2}H) g/mol chains to synthesize unimodal networks. The polydispersity index of all chains was 1.32 or lower. For both unimodal and bimodal networks, tetrakis(dimethylsiloxy)silane cross-linker was added such that the ratio of cross-linking arms to polymer chain ends was 1.7 to form networks of the highest possible quality.[30] Because this optimal ratio is smaller for shorter precursor chains,[31] it was reduced to 1.5 for the 5000 g/mol unimodal sample only. In one network, 36000 g/mol chains were mixed with non-reactive 2000 g/mol chains at a 70/30 mass % ratio before cross-linking. This network was tested in the preparation state (36000p) and in the dry state after extraction of the free chains (36000d). The PDMS/crosslinker mixtures were well-stirred with a spatula and mixed on a rotator overnight for homogeneous distribution of the components. Networks were formed upon addition of the catalyst cis-dichlorobis(diethylsulfide)platinum(II)

using the methods detailed in reference 29. Equilibrium mass swell Q, soluble fraction w_{sol}, and elastic Young's modulus E of the fully cured elastomers were all determined by previously reported techniques.[29] The E value for 36000p was calculated from that of 36000d by multiplying the latter by the polymer volume fraction in the prepared state raised to the 1/3 power.[32] These bimodal and unimodal network properties are reported in Table 2.1. ^{2}H-NMR data were obtained on a Tecmag Apollo HF spectrometer operating at 30.72 MHz for deuterium by employing a 5μs 90^{o} pulse. For stretched samples, the direction of the magnetic field is perpendicular to the strain axis. Methods for processing these data are described in reference 28.

Table 2.1: Network compositions and properties

5000(^{2}H)-80000 g/mol bimodal networks

mol % short chains	Q	E(MPa)	w_{sol} (mass %)	$\langle\|\nu\|\rangle_0$ (Hz)	q* (Hz/MPa)
60	4.76	0.59	1.72	193	31.1
70	4.53	0.64	1.49	205	66.6
80	4.21	0.73	1.61	209	56.3
90	3.65	0.93	0.88	260	81.5
95	3.26	1.14	1.13	282	112.0
98	3.17	1.20	1.92	230	-

5500-90000(^{2}H) g/mol bimodal networks

mol % short chains	Q	E(MPa)	w_{sol} (mass %)	$\langle\|\nu\|\rangle_0$ (Hz)	q* (Hz/MPa)
60	5.24	0.49	2.18	81	71.6
70	4.68	0.60	1.82	89	72.0
80	4.09	0.76	1.01	85	71.9
90	3.99	0.80	2.31	84	65.2
95	3.78	0.88	2.46	87	49.9

unimodal networks

M_n (g/mol)	Q	E(MPa)	w_{sol} (mass %)	$\langle\|\nu\|\rangle_0$ (Hz)	q* (Hz/MPa)
5000	3.02	1.30	0.59	181	54.5
11000	3.39	1.06	0.80	169	93.3
36000	4.64	0.61	1.45	96	65.0
90000	7.31	0.27	5.48	77	106.5
30000**	4.55	0.63	2.36	47	26.3
36000d***	5.98	0.39	1.46	107	73.3
36000p***	-	0.35****	-	103	80.6

*q = slope of best fit line through $(\langle\nu\rangle/E)/(\alpha^2-1/\alpha)$

**Consists of unlabeled elastic chains and ^{2}H-labeled probe chains, both with M_n = 30000 g/mol. Unlabeled soluble material was extracted before dissolution of labeled free chains.

***Unimodal network made with 70 mass % 36000 g/mol ^{2}H-labeled precursor chains and 30 % 2000 g/mol non-reactive and unlabeled "solvent" chains. ^{2}H-NMR experiments were performed on networks in the prepared state (p) and in the dry state after extraction of the solvent chains (d).

****Elastic modulus of network in the prepared state calculated from E of the dry network as detailed in the text.

2.2.2 Estimating the Average Chain Segment Order ⟨ν⟩ from ^{2}H-NMR Spectra. In this paper we used a recent theoretical method[27] that estimates, from ^{2}H-NMR spectral data, the average frequency splitting ⟨ν⟩ or segment-orientation order parameter of chain segments in a polymer network. Calculation of ⟨ν⟩ is valuable to understand chain segment alignment because the observed quadrupolar splitting Δν does not measure the total average orientation of the chain segments. Several works[11-14] have shown that the quadrupolar splitting Δν induced at high elongation measures only segment orientation resulting from excluded volume interactions between interacting chains. Conversely, the average frequency ⟨ν⟩ accounts for the segment orientation resulting from both excluded volume interactions and constraints imposed by the cross-links along with chain entanglements within a given network. However, the ensemble average frequency ⟨ν⟩, defined by Equation 2.1a below, cannot be calculated directly from spectral data because the ^{2}H-NMR frequency spectrum $f(\nu)$ is the frequency probability distribution $\rho(\nu)$ symmetrized around ν=0 (Equation 2.1b), and all the odd moments of $f(\nu)$ are therefore equal to 0.[27] On the contrary and due to this symmetric relationship between $f(\nu)$ and $\rho(\nu)$, their even moments and the average absolute values of any power of ν are identical for both $f(\nu)$ and $\rho(\nu)$ (Equation 2.1c).[27]

$$\langle \nu \rangle = \int \nu \rho(\nu) d\nu \tag{2.1a}$$

$$f(\nu) \propto \rho(\nu) + \rho(-\nu) \tag{2.1b}$$

$$\langle |\nu| \rangle = \int \rho(\nu) |\nu| d\nu = \frac{\int f(\nu) |\nu| d\nu}{\int f(\nu) d\nu} \tag{2.1c}$$

Where $f(\nu)$ is the ^{2}H-NMR signal at frequency ν, the $\rho(\nu)$ is probability density

distribution of frequencies ν, and the integrals are over the entire frequency spectrum.

The employed strategy[27] to estimate ⟨ν⟩ is based on truncated Taylor Expansions and considers the entire ^{2}H-NMR lineshape, including the wide spectral wings often observed for elastomers. After computing the average absolute value ⟨|ν|⟩ from Equation 2.1c,[27] the estimate of the average frequency ⟨ν⟩ (or chain segment order parameter) for uniaxial extension is solved for from the following nonlinear equation:[27]

$$\frac{\langle|\nu|\rangle}{\langle|\nu|\rangle_0} \cong \frac{\langle\nu\rangle}{\langle|\nu|\rangle_0} + \exp\left(-\frac{\langle\nu\rangle}{\langle|\nu|\rangle_0}\right) \qquad (2.2)$$

where $\langle|\nu|\rangle_0$ is the average absolute frequency value of the unstrained sample.

2.2.3 Simulation Methods. ^{2}H-NMR spectral data were calculated for coarse-grained bimodal networks obtained from Monte Carlo simulations. In our previous work[29] we have shown that the molecular model used in this work provides a good representation of model PDMS bimodal networks in terms of mechanical properties and network microstructure. The simulation methods for the end-linking reaction, uniaxial deformation, and obtaining the ^{2}H-NMR spectrum of the simulated networks are briefly described below. A more comprehensive description of these simulation procedures can be also found in reference 29.

2.2.3.1 Network end-linking. The end-linking reaction was simulated on a lattice using the Bond Fluctuation Model (BFM).[33] In this scheme, coarse-grained cubes representing chain monomers and crosslinks are capable of forming chemical bonds along any of 108 bond vectors accessible in the BFM. Each coarse-grained unit roughly mimics 4 monomers of PDMS (~300 g/mol).[29] The simulation of the end-linking reaction is carried out athermally, that is, only bonding restrictions and

excluded-volume interactions were considered. For all the simulated networks, lattice volume fractions were set around 0.47, resembling melt-like conditions.[34] Hop moves, which mimic diffusive dynamics,[35] of the coarse-grained cubes were used to equilibrate polymer chains and crosslinks. This equilibration stage involved 10^6 moves per coarse-grained unit on average.

The end-linking reaction was initiated after equilibration, by allowing bond formation between chain ends and crosslinks, as the system relaxed through the hop moves. When the fraction of unreacted chain ends was 0.01 or lower, the reaction was ended. The resulting soluble mass fractions were less than 0.003, and the mol fractions of inelastic chains (single looped or pendant) were no greater than 0.05 in the unimodal networks and 0.25 in the bimodal networks. The ratio of crosslink arms to chain ends, r_x, was used to tune the soluble fraction for each simulated network. Detailed information about the resulting simulated networks is shown in Tables 2.2 and 2.3.

2.2.3.2 Network uniaxial deformation. Uniaxial extension, NPT Monte Carlo, simulations were conducted off-lattice to produce continuous and smooth deformations. Preserving the network structure and polymer volume fraction, coordinates from the end-linking (on-lattice) simulations were transformed into a continuous framework. In this continuous scheme, coarse-grained units that represent chain monomers and crosslinks were modeled as purely repulsive beads, through a cut-shifted Lennard-Jones interaction potential, with diameter σ_{LJ} and interaction energy ε_{LJ}. An infinite square-well potential was used to model the interaction between bonded beads; such bonding potential allowed bond lengths to fluctuate between $0.8\sigma_{LJ}$ and $1.2\sigma_{LJ}$.

Table 2.2: Characteristics of the simulated set of unimodal networks

Chain length (# of beads)	r_x	Number of chains	Number of cross-links	w_{sol} (mass%)	Inelastic cont. (mol%)	Slope q*
15	1.05	1659	871	0.00	5.3	0.339
29	1.10	858	472	0.00	4.4	0.341
43	1.05	579	304	0.00	3.3	0.343
129	1.15	193	111	0.00	2.6	0.357

* Slope q is the average slope of the plot $\langle S \rangle/E$ vs. α^2-1/α and is in σ_{LJ}^3/k_BT units.

One Monte Carlo cycle consisted of a fixed number (equal to the total number of beads in the system) of attempted single-site moves (95% hops and 5% flips) plus two volume moves in complete random order. Hop, flip and volume moves had acceptance ratios of 0.30, 0.45, and 0.35, respectively. Simulations were performed at temperature T =2.0 (in ε_{LJ}/k_B units), pressure P = 3.0 (in k_BT/σ_{LJ}^3 units) at the unperturbed state, and the resulting melt-like density was approximately 0.8 (in $1/\sigma_{LJ}^3$ units). An isostress ensemble was employed to simulate the deformation of the networks subject to given stresses. The imposed stresses on the z direction are the result of the differences of applied normal stresses $(P_{xx} + P_{yy})/2 - P_{zz}$, where P_{xx}, P_{yy}, and P_{zz} are the applied normal stresses in the x,y, and z directions correspondingly; and the quotient of the box z-length after equilibrating the system for a given stress to the initial undeformed box z-length gives the extension ratio α. On average the box dimensions reached plateau values (i.e., the system achieved mechanical equilibrium)

after 10^7 Monte Carlo cycles.

Table 2.3: Characteristics of the simulated set of (15-300-bead) bimodal networks

Short chain cont. (mol%)	r_x	# of short chains	# of long chains	# of cross-links	w_{sol} (mass%)	Inelastic cont. (mol%)	Total Slope q*
60	1.15	110	73	105	0.07	25.1	0.344
70	1.00	169	73	121	0.13	18.2	0.330
80	1.10	268	67	185	0.25	15.8	0.331
90	1.05	490	54	286	0.00	12.7	0.319
95	1.10	778	41	451	0.00	9.3	0.313
98	1.10	1106	21	621	0.07	7.5	0.315
100	1.05	1659	0	871	0.00	5.3	0.339

* Total slope q (in σ_{LJ}^3/k_BT units) is the slope of the plot $\langle S\rangle/E$ vs. α^2-$1/\alpha$ where $\langle S\rangle$ is the weighted average chain segment order parameter of short and long chains.

2.2.3.3 Simulated ^{2}H-NMR spectra. If the chain segments are in "the fast motion limit" (i.e., when the temperature is higher than the polymer glass transition temperature) the ^{2}H-NMR spectrum $f(\nu)$ can be written as the symmetric part of the frequency (or order parameter) distribution $\rho(\nu)$;[36] that is, $f(\nu) \propto \rho(\nu) + \rho(-\nu)$. Hence, simulated spectra can be extracted straightforwardly from the order parameter distributions obtained from Monte Carlo simulations.[36-38] Because $\rho(\nu)$ is the distribution of the time-averaged segment-orientation order parameter, values of order

parameter for each chain segment were stored every 40 cycles during an additional run of approximately 3×10^7 cycles. This additional run was performed after the deformed networks reached equilibrium. Subsequently, the average order parameter over the entire additional run is computed for each chain segment, and used to construct the distribution histogram of the order parameter $\rho(\nu)$. The simulated frequency spectrum $f(\nu)$ was obtained by normalizing $\rho(\nu)+\rho(-\nu)$. The width of the bins used to construct the histograms ranged between 0.002 and 0.004 in order parameter (dimensionless) units for all the simulated systems.

2.3 Results and Discussion

2.3.1 Unstrained Bimodal Networks. ^{2}H-NMR spectra for undeformed bimodal networks with selectively labeled short and long chains are shown in Figures 2.1a and 2.1b, respectively. All spectra are plotted with equal peak heights to emphasize the relative contributions from the center portion of the lineshape and the high frequency spectral wings. Comparison of Figures 2.1a and 2.1b demonstrates the different lineshape characteristics for the 5000 and 90000 g/mol chains. While the short-chain spectra have wide wings that form the "super-Lorentzian" shape typically observed for PDMS networks,[39,40] the long-chain lineshapes are relatively broad in the center but diminish rather quickly. Because the spectral wings correspond to the portion of the segment order distribution that is associated with more highly stretched chains, we have attributed the 5000 g/mol lineshape to a higher proportion of these chains cross-linked when they were in a conformation with relatively higher radii of gyration. This is more clearly observed in Figure 2.2a, where only the distributions of the radius of gyration for the elastic short chains in the simulated networks are

displayed. As shown in Figure 2.2a, the elastic short chains in the bimodal networks shown (60 and 90 mol% short) are slightly more stretched than those in a network of pure short chains (100 mol% short). This is because the crosslinks are effectively farther apart in bimodal networks where they are less concentrated than in networks made of pure short chains, and as a consequence, short chains may need to stretch slightly more to reach them. The long network chains, meanwhile, appear to be less perturbed from their melt configurations because the number of accessible crosslinks inside their pervaded volume is still very high for all the short chain contents (see values of n_x in Table 4 in reference 29).

Figure 2.1 reveals that these general lineshapes persist for 5000 and 90000 g/mol chains when they are incorporated into bimodal networks. However, it is immediately clear from Figure 2.1a that the lineshape of the short chain segments evolves with network composition, while the lineshapes of the long chains appear unchanged as their concentration varies. The wings increasingly contribute to the spectra as the short chain content is increased from 60 to 90 mol %, then shrink at 98 mol % and for the unimodal short chain network (100 mol %). The wider spectral wings observed in the 90 mol% short network, with respect to 60 mol% short network, can be attributed to the fact that the elastic short chains in the 90 mol% network are slightly more stretched than those in the 60 mol% network (Figure 2.2a). This trend also holds for the labeled short chain networks (70, 80, 95 mol %) that were omitted from the figures for clarity.

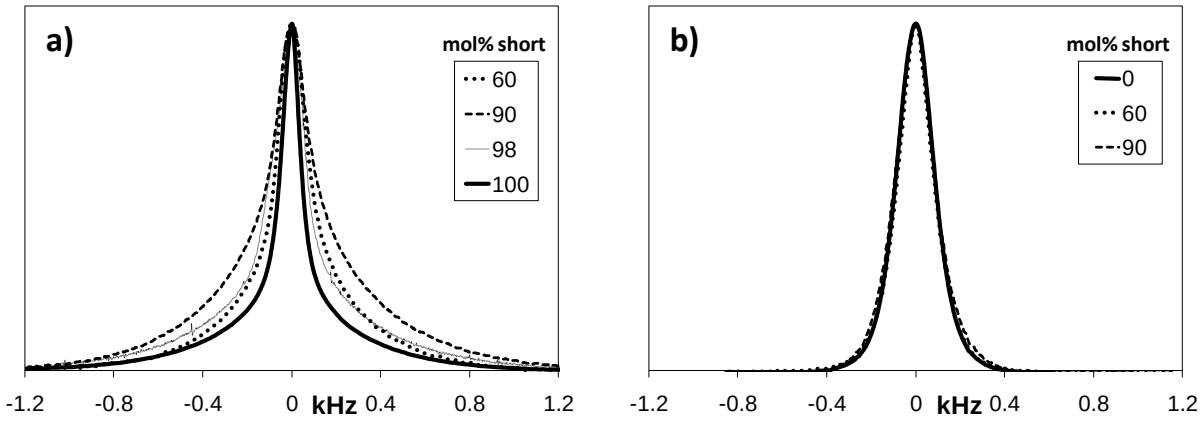

Figure 2.1: ^{2}H-NMR spectra for a) short (5000 g/mol) and b) long (90000 g/mol) chain segments in bimodal networks. Spectra are measured on samples in the unstrained state and are normalized by peak height.

The varying wing contribution to the spectra is clearly quantified in Figure 2.2b, where the relative average absolute values at the unperturbed state $\langle|\nu|\rangle_0$ (Equation 2.1c), normalized with respect to $\langle|\nu|\rangle_0$ of the network with 100 mol% of short chains, for short and long chains in the PDMS networks are plotted against mass (and mol) % of short chains. Figure 2.2c shows the dependence of the dimensionless average absolute frequency value $\langle|\nu^*|\rangle_0$ with the network composition for the simulated bimodal networks. Error bars in Figure 2.2c are always smaller than the symbols used; specifically, the uncertainty is on average 0.02 and 0.005 (in dimensionless units) for short and long chains, respectively. Although Figures 2.2b and 2.2c differ qualitatively, a much stronger dependence on the network composition of average absolute frequency value $\langle|\nu|\rangle_0$ of the short-chain segments is evident for both experimental and simulated networks. Qualitative discrepancies between experimental and simulated results for $\langle|\nu|\rangle_0$ may be attributed to the fewer defects present in the simulated network models. A maximum $\langle|\nu|\rangle_0$ for the short chains is observed (Figures 2.2b and 2.2c) around a network composition of 95 mol% of short

chains or ~ 50-60 mass% of short chains. At this network composition, most short chains would be elastically coupled and would form an infinite cluster that pervades the entire space. Additional work is necessary to confirm this conjecture about the network microstructure at such compositions.

The nearly constant lineshape for the long chains in Figure 2.1b is well described by the constant value of $\langle|\nu|\rangle_0$ across all concentrations in Figure 2.2b. Thus, the residual segmental order imposed on the long chains during cross-linking is not significantly affected by the introduction of a bimodal distribution of chain lengths. Long chains also showed similar segmental order parameter distributions across a variety of bimodal network compositions in recent MQ-NMR studies of 800-47000 g/mol PDMS elastomers.[7,25] In unimodal 90000 g/mol networks, the lineshape broadens only slightly upon network formation because the cross-link concentration is low, and the network chains are perturbed negligibly from their random coiled states.[28] Clearly, this persists in bimodal networks even with the increase in cross-linking density caused by the introduction of short chains. The 90000 g/mol chains likely react with the nearest cross-linker without much change in their melt state segmental order or end-to-end distance. An alternative physical interpretation for these nearly unperturbed lineshapes for the long chains may be that the topological constraints imposed on the long chains by the cross-links, are not as fixed in space over the timescale of the NMR experiment as they are for short chains. In either case, the impact of the network composition on the lineshapes is significantly stronger on the short chains than on the long chains.

The short chains are clearly affected by incorporation into the bimodal network. We believe the variation in the spectral wings to be a consequence of

changes in the network topology with short chain concentration in the network. MC simulations have demonstrated an increased pair distribution function for the intermolecular centers of mass g(r) upon cross-linking for 60 mol % short chain bimodal networks with molar masses similar to those employed in these experiments.[29] Therefore, the short chains can aggregate into heterogeneous domains when their concentrations are relatively low due to the faster diffusion of the mobile chains and cross-linkers in the mixture. Clustering has also been observed for networks with low short chain concentrations via SANS[3,6] and light scattering.[5] Therefore, it is not surprising that the lineshapes for the 60 and 100 mol % short chain networks are similar ($\langle|\nu|\rangle_0$ = 193 and 181 Hz) even though the network compositions are very different. Because the short chains form clusters in the 60 mol % network, most of a given short chain's neighbors are other short chains and the cross-link density in their vicinity is quite high. Thus, the segmental order of these chains is affected negligibly by the presence of the long chains, and the microstructure can be pictured as small domains of 5000 g/mol unimodal network dispersed in a unimodal network of long chains. The similarity of 98 and 100 mol % short chain spectra, meanwhile, is expected given the similar number of the 5000 g/mol chains in each system. The smaller chains dominate the volume of the network in this bimodal system. Consequently, we suspect the long chains to be intermittently woven into an interconnected skeleton of short chains that spans the whole network. The 90 and 95 mol % networks have the most prominent spectral wings in Figures 2.1a and 2.2, indicating a greater degree of motional restriction on their short chain segments. At these concentrations the short chains are near their overlap concentrations in a 5000-80000 g/mol system. Thus, it appears that the lower molar mass chains in these

networks do not form small clusters, but instead reach cross-linker arms when they are slightly elongated from their random states. Here, the difference in residual segmental order between the short and long chain segments is at a maximum (Figure 2.2b).

2.3.2 Stretched Bimodal Networks. Both experiments[13] and theoretical models[11,14,26] have established that the quadrupolar splitting $\Delta\nu$ induced at high extension is the result of excluded volume interactions between chain segments. When normalized by the elastic modulus E, $\Delta\nu$ has been shown to follow a universal relationship with the extension term α^2-1/α.[13] However, additional details of the ^{2}H-NMR lineshape describe network chains that are greatly affected by the network constraints.[38,26] Specifically, the outer frequency portions of the lineshape have been associated with more ordered chain segments that have less motional averaging, because these wings represent the tail of the order parameter probability distribution.

Figure 2.3 further illustrates why the peak frequency split $\Delta\nu$ is not useful as a measure of the average segmental order. Although the short chains in the 60 and 90 mol % networks each have a similar $\Delta\nu$ value in the plotted spectra, the wings are noticeably more prominent in the latter. Therefore, the higher proportion of ordered chain segments found in the rest state for the 90 mol % short chain elastomer (Figure 2.1a) continues as the network is extended. Clearly, the initial chain conformations affect the segmental order induced upon loading. Due to these differences in lineshape, we used Equation 2.2 to calculate the average segmental order $\langle\nu\rangle$ for the 60 and 90 mol % short chain bimodal networks at various elongation ratios. The results are normalized by the corresponding elastic modulus and displayed in Figure 2.4 against the average segmental order resulting from intersegmental interactions

(Section 2.3.3). We must compare to ½Δν/E here because the two peaks in a ^{2}H-NMR spectrum are the result of the order parameter distribution and its mirror image reflected about $\nu = 0$. Although the trend for the 60 mol % short chain sample is noisy due to the lower ^{2}H content in this network, it clearly follows the ½Δν/E trend more closely than the 90 mol % network. Consequently, the segmental order of short chains in the 60 mol % network is more influenced by excluded volume interactions between segments than by chains with large end-to-end distances

Because we selectively labeled both the short and long chains in our PDMS bimodal networks, it is instructive to compare the segmental order as each sample is stretched. These plots of $\langle\nu\rangle$/E vs. α^2-1/α are displayed for 60, 70, 90 and 95 mol % short chain networks in Figure 2.5. The segmental orientation of the short chains approaches and surpasses that of the long chains as the short-chain concentration increases. At 60 mol % short chains, the clustered chains appear to be shielded from order by the more compliant long chain matrix. We recently concluded that such highly heterogeneous networks do not show enhanced macroscopic properties,[29] and the results in Figure 2.5a reinforce this view. If short chain clusters were to aid in the toughening of these elastomers, the short chains would have to sustain a significant portion of the applied load. Instead, the ordering of these segments appears to be highly influenced by interchain segmental interactions (Figure 2.4).

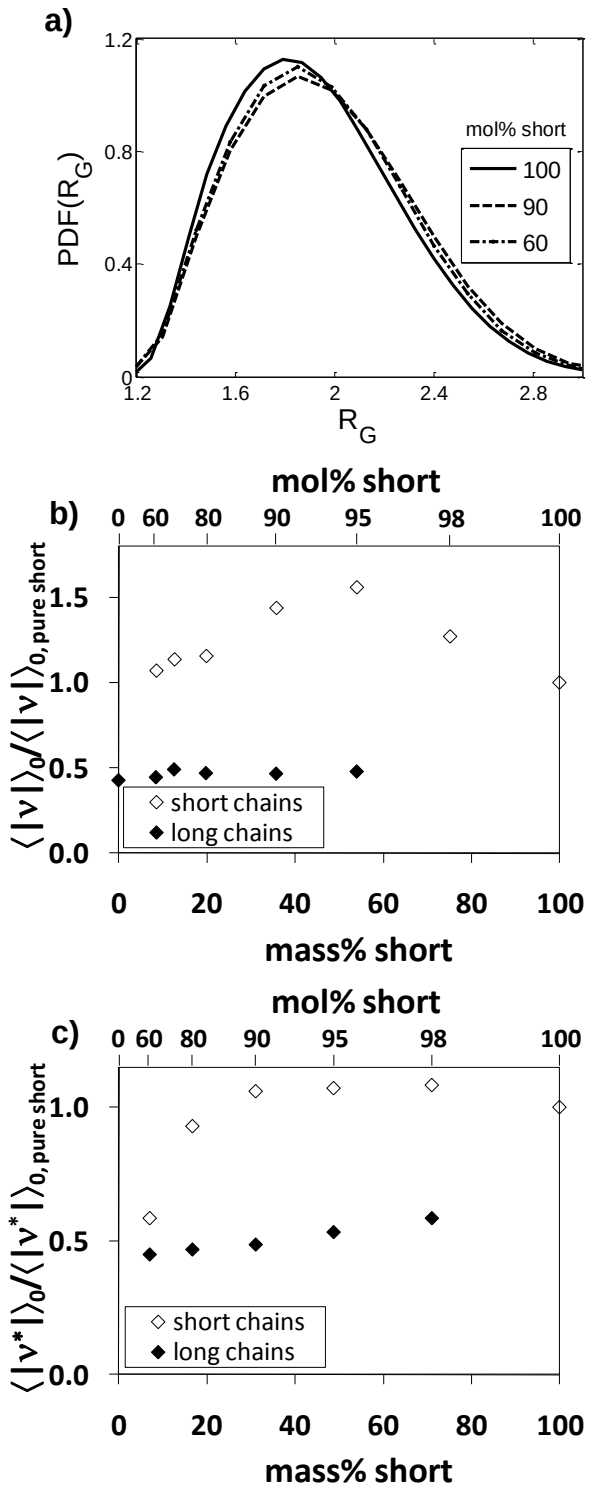

Figure 2.2: a) Probability density function for the radius of gyration of elastic short chains only in simulated networks with different short chain compositions. b) Experimental and c) simulation values of the average absolute value for unstretched bimodal networks $\langle|\nu|\rangle_0$, relative to the value of $\langle|\nu|\rangle_0$ for the 100 mol% of short network, with varying short chain concentration.

.

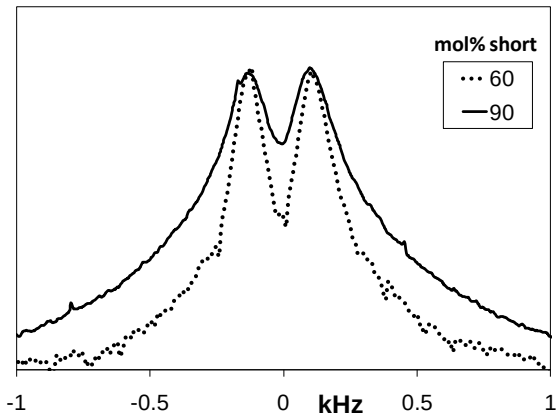

Figure 2.3: Bimodal networks at 60 and 90 mol % ^{2}H-labeled short chains (α = 2.43 and 1.81, respectively) have similar spectral splitting $\Delta\nu$ but different overall lineshapes. The wide spectral wings in the 90 mol % network indicate a large contribution from highly stretched chains.

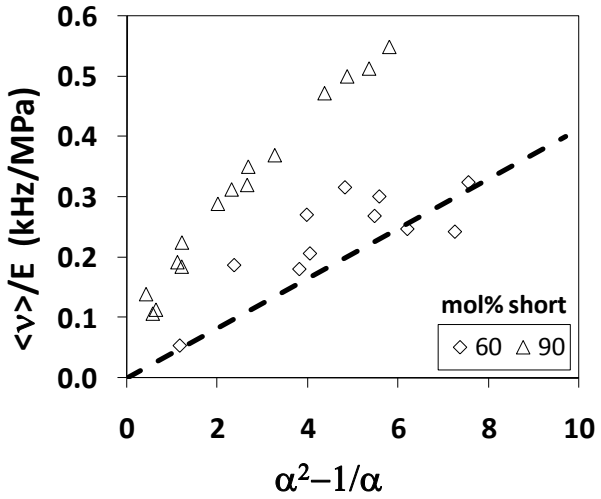

Figure 2.4: Average segmental order $\langle\nu\rangle$ normalized by elastic modulus E for bimodal networks at 60 and 90 mol % ^{2}H-labeled short chains at increasing extension. The 60 mol % short chain segments follow approximately the universal curve for excluded volume interactions between chain segments $\frac{1}{2}\Delta\nu/E$ (dashed line). The average order is much higher for the short chains in the 90 mol % network due to its wide spectral wings.

Analogous results for simulated bimodal networks are displayed in Figure 2.6, where the dependence of the normalized chain segment order parameter ($\langle S\rangle/E$) on extension (α^2-1/α) is displayed for 60, 70, 90 and 95 mol % short chains. Simulations

predict similar segment orientation for both chains upon uniaxial extension of a 60 mol % short chain network (Figure 2.6a) whereas this equivalence occurs experimentally when the short chain content is 70 mol % (Figure 2.5b). Therefore, the agreement between simulations and experiments is reasonable. The discrepancy in the equivalence point may be attributed to small variations in the microstructure of simulated networks caused by different crosslink concentrations employed in curing simulations (~30% lower than in experiments). Lower crosslink concentrations were used in the BFM end-linking simulations because they yield nearly ideal networks with very low (~ 0.1 mass %) minimum soluble fractions at such concentrations.[29,41] Beyond this equivalence point in segmental orientation between short and long chains, segments on the shorter chains are more aligned than those from the long chains.

The results for the simulated 90 and 95 mol % short chain networks (Figures 2.6c and 2.6d) slightly differ from trends observed in the experimental networks (Figures 2.5c and 2.5d). However, short chain segments orient significantly more than long chain segments in both experimental and simulated networks with short chain content of 90 and 95 mol %. Contrary to the experimental evidence, in simulated networks short chain segments orient more upon extension in the 90 mol % network than in the 95 mol % network. The disparity of the observed trends may imply, as aforementioned, the existence of certain differences in microstructural details between (experimental) PDMS and simulated networks. Nevertheless, a perfect mapping (as a function of network composition) between the microstructures of experimental and simulated networks should not be expected because the used coarse-grained molecular model is very simple and lead to more perfect structures than can be achieved experimentally, as previously mentioned in Section 2.3.1.

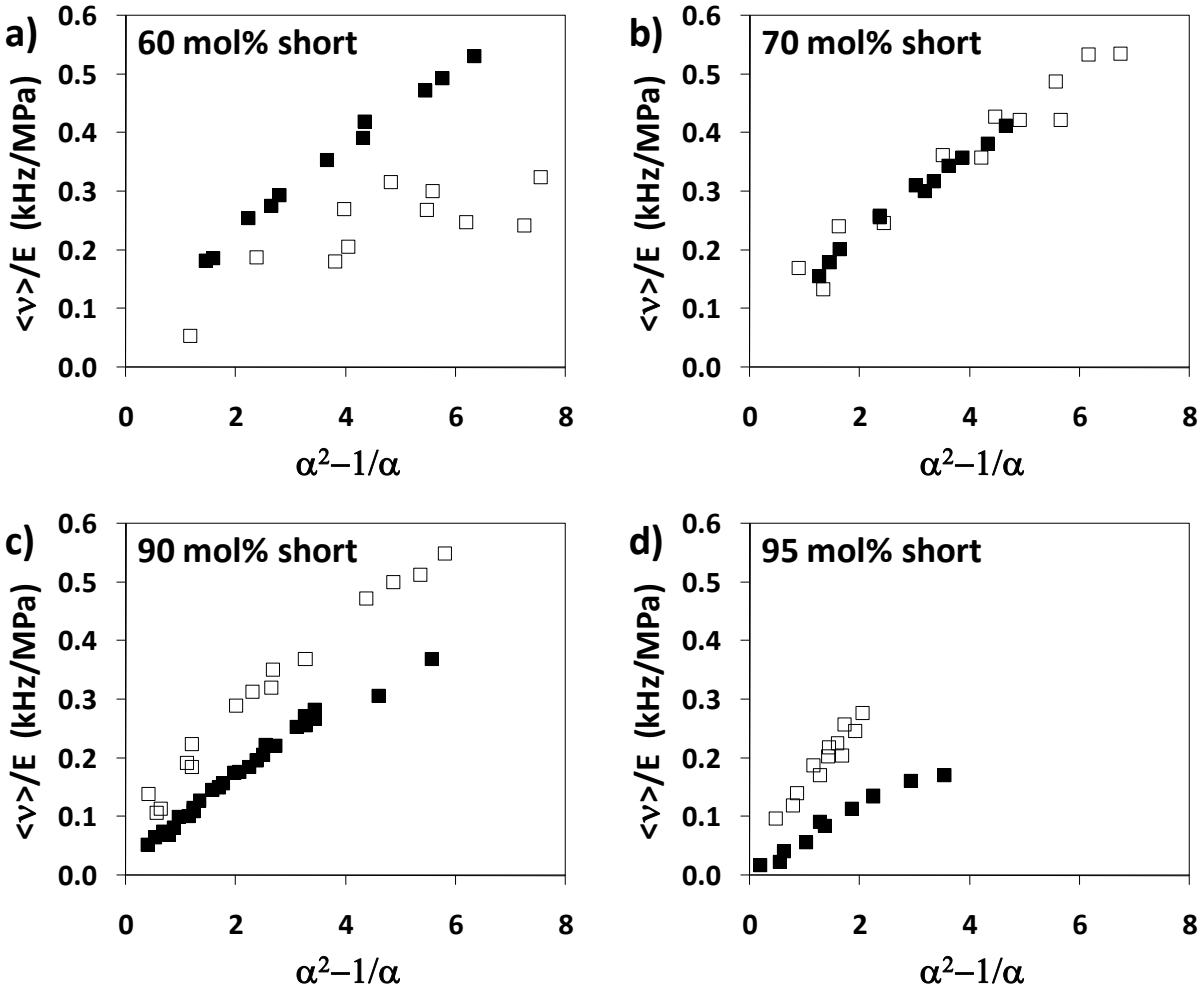

Figure 2.5: Average segmental order ⟨ν⟩ normalized by elastic modulus E for short (open squares) and long (filled squares) chain segments in a) 60 b) 70 c) 90 and d) 95 mol % short chain bimodal networks. The segment orientation of the short chains increases relative to the long chains as the short-chain concentration is increased.

Networks at 90-95 mol % short chains display the greatest enhancement in mechanical properties[2,8,9,29] because further addition of short chains leads to very brittle samples. Note that even the 95 mol % short chain network breaks at a small value of α (Figure 2.5d). Increased ordering of the short chain segments appears to play a role in generating the stress upturn at high strain and increased toughness of

these networks. Thus, the limited extensibility of the 90-95 mol % short chains must be the primary cause of the improved mechanical properties. While $\langle \nu \rangle$ is not a direct measure of end-to-end distance, the prominent spectral wings in the 90 mol % network (Figure 2.3) suggest that a significant portion of the orientation is due to segments on chains that are highly stretched by the movement of the cross-links. In fact, MC simulations have indicated that short-chain end-to-end distances in 90 mol % networks increase markedly with uniaxial elongation as compared to those in 60 mol % short chain networks.[29] Increased residual order upon cross-linking for the short chains in the 90 and 95 mol % networks (Figures 2.1a, 2.2) predisposes some of these chain segments to a highly aligned state upon stretching.

While these results suggest that the extensibility of the short chains is a key factor in the enhanced mechanical properties of bimodal networks, we note that MC simulations have predicted that some degree of topological heterogeneity is likely at compositions around 90 mol % short chains.[29] Additionally, the overall order parameter distribution in 800-47000 g/mol networks measured by MQ-NMR has a bimodal character up to relatively high short chain concentrations, suggesting a slightly heterogeneous structure.[7,25] Thus, while relatively concentrated short chains in a 90 mol % network will not form small clusters, there are likely regions within such networks with higher cross-link densities. At this bimodal network composition, pockets with larger concentrations of long chains interspersed amongst the overall stiffer matrix would likely provide ductility. Such a structure might explain why the 90 mol % short chain network (Figure 2.5c) could be stretched to nearly the same elongation at fracture as the 60 or 70 mol % networks (Figures 2.5a, 2.5b) even with the associated increase in cross-link density.

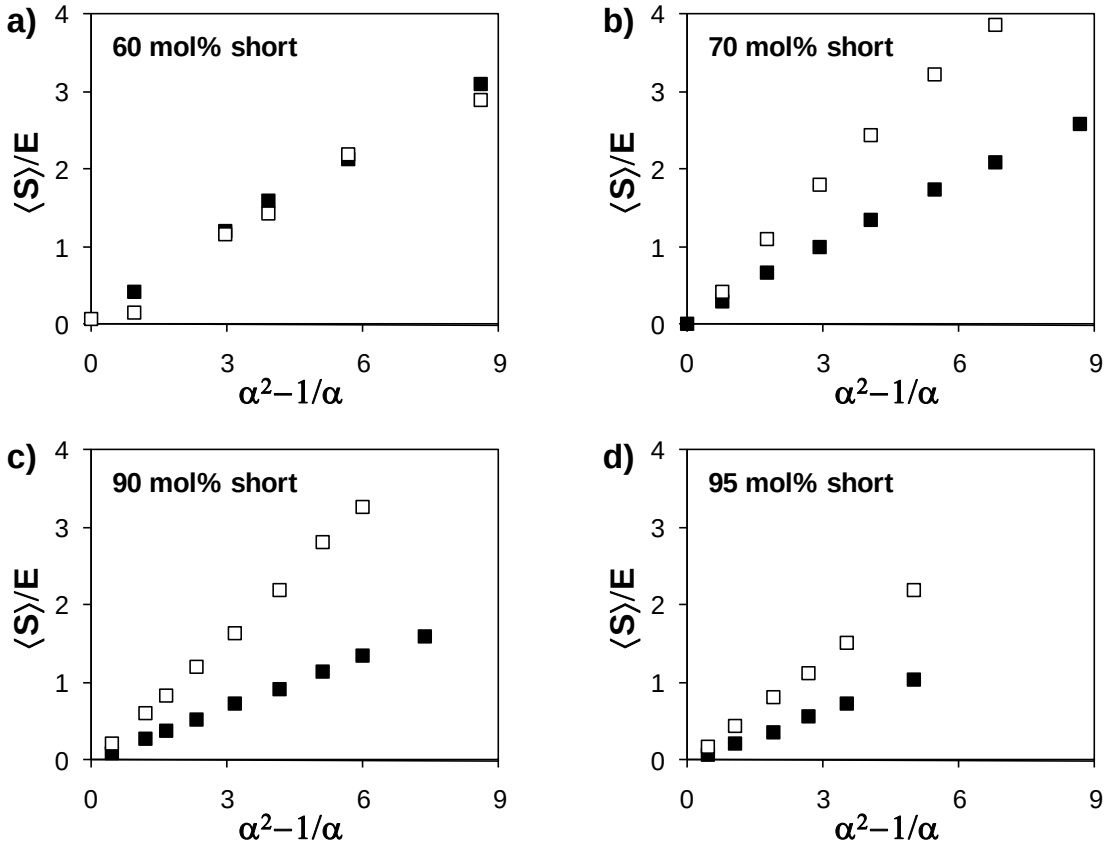

Figure 2.6: Average segmental order, ⟨S⟩, normalized by the dimensionless elastic modulus, E (in $k_B T/\sigma_{LJ}^3$ units), from molecular simulations of bimodal networks. Averages order parameters shown for short (open squares) and long (filled squares) chain segments in networks with a) 60 b) 70 c) 90, and d) 95 mol % of short chains.

Classical rubber elasticity theories[32,42] predict that the average order parameter ⟨S⟩ is directly proportional to E (α^2-1/α). Because ⟨ν⟩ is a measure of ⟨S⟩, plots of ⟨ν⟩/E vs. α^2-1/α should follow a universal trend. Defining the slope of this line as q and taking the best fit line through our data, it seems from Table 2.1 that this universal relationship does not hold for our unimodal networks. This is unlike the previously reported Δν/E vs. α^2-1/α data that follow the expected trend rather well,[13] but Δν/E quantifies solely the contribution to segment orientation that arises from excluded volume interactions between neighboring segments.[13,38,26] It is also important to mention that the universal trend predicted by such classical theories is obtained for

simulated unimodal networks (see Table 2.2). The average q for unimodal networks listed in Table 2.1 is calculated to be 80 +/- 24 Hz/MPa whereas the average q for the simulated unimodal networks shown in Table 2.2 is 0.345 +/- 0.008 (in σ_{LJ}^3/k_BT units). The reason the theoretically predicted trend holds for the simulated unimodal networks, and not for experimental unimodal samples, may be attributed to the fact that the amount of inelastic (i.e., single-looped and pendant) chains in all simulated unimodal networks is relatively similar (Table 2.2). This similarity in the amount of inelastic material is not possible to achieve in all the PDMS unimodal samples.

As detailed in Figures 2.5 and 2.6, there is a clear redistribution of chain segment orientation with short chain concentration. Figure 2.7 nicely quantifies this redistribution by displaying plots of relative values of the slope q vs. mass (and mol) % of short chains, for both PDMS and simulated bimodal networks. Computation of the weighted average q, q_{ave}, for each bimodal network is then performed by weighting the slopes for both the short and long chains (Figure 2.5) by their respective mass fractions within each network[27] (i.e., q_{ave} = (mass% $_{short}$) q_{short} + (mass% $_{long}$) q_{long}). Contrary to the results obtained from the set of PDMS unimodal networks and in agreement with classical theories, the studied set of both experimental and simulated bimodal networks (Figures 2.7a and 2.7b) seem to exhibit the above mentioned universal trend. This is because the weighted averages q_{ave} remain relatively constant over different network compositions. The q_{ave} values yield a rather consistent mean value of $q_{mean} = (\langle\nu\rangle/E)/(\alpha^2\text{-}1/\alpha)$ = 69.5 +/- 9 Hz/MPa for PDMS bimodal networks and $q_{mean} = (\langle S\rangle/E)/(\alpha^2\text{-}1/\alpha)$ = 0.327 +/- 0.012 (in σ_{LJ}^3/k_BT units) for the simulated bimodal networks. These two mean average values q_{mean} are used as normalizing constants in Figures 2.7a and 2.7b, respectively.

Comparison of Figure 2.7a with 2.7b reveals evident qualitative discrepancies in the dependence of q/q_{mean} on the short chain content for the short chains in PDMS and simulated bimodal networks. Such qualitative differences are due to the more perfect networks achieved in the simulations (e.g., the almost stoichiometric end-linking concentrations used, and the significantly lower sol fractions obtained). Moreover, these qualitative discrepancies were somewhat expected because they are equivalent to those mentioned earlier when contrasting segment orientation trends in Figures 2.5 and 2.6. Thus, the corresponding previous discussion about those disparities also addresses the disparities found in Figures 2.7a and 2.7b.

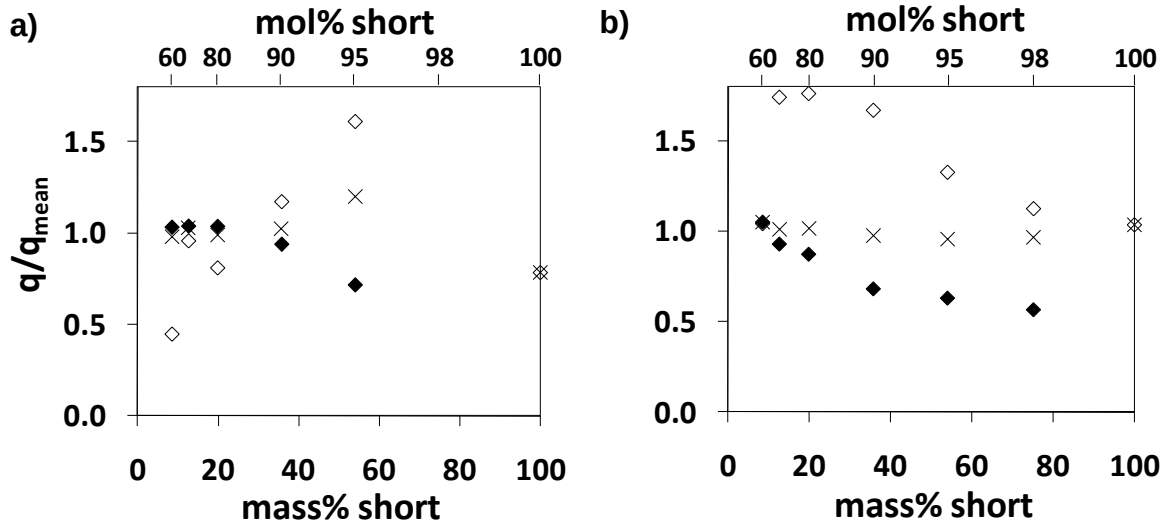

Figure 2.7: a) Relative slopes of $\langle v \rangle/E$ vs. α^2-$1/\alpha$ = q at various bimodal compositions of PDMS networks; and b) relative slopes of $\langle S \rangle/E$ vs. α^2-$1/\alpha$ = q at various bimodal compositions of simulated networks. Values of relative q shown for short (open diamonds) and long (filled diamonds) chain segments. The mass % weighted average slope, q_{ave}, at each composition (x) is also displayed. All shown values are relative to q_{mean}, defined as the mean q_{ave} of the entire set of bimodal networks. For a) q_{mean}= 69.5 Hz/MPa, and for b) q_{mean}= 0.327 in $\sigma_{LJ}^3/k_B T$ units.

2.3.3 ^{2}H-NMR Lineshapes of Highly Stretched Networks. We recently reported on ^{2}H-NMR lineshapes for a series of unimodal networks.[28] At high extension, the 36000 g/mol network spectra displayed a prominent shoulder in

addition to the expected spectral splitting (Figure 2.8b). The lineshapes were empirically fit to two pairs of doublets with splittings $\Delta\nu_w$ (outer or wide) and $\Delta\nu_n$ (inner or narrow) to describe the separation between the shoulders and the peak maxima, respectively.[28] This $\Delta\nu_n$ was shown to be equivalent to the $\Delta\nu$ reported in all previous ^{2}H-NMR studies. We attributed the wide or outer splitting to the alignment of chain segments that are highly influenced by the cross-link constraints, while the narrow or inner splitting is thought to result from excluded volume interactions between segments of chains not very extended.[28] Two populations are also observed in the ^{2}H-NMR spectra for labeled 90000 g/mol chains in highly extended bimodal networks (Figure 2.8a). The spectrum lineshapes of certain simulated unimodal (Figure 2.8d) and bimodal (Figure 2.8e) networks exhibit also a peculiar noticeable shoulder when highly stretched.

To explore the nature of those "*two apparently different sub-populations*" of chain segments that yield the two pairs of doublets in the ^{2}H-NMR spectra, we use molecular simulations to examine in detail how chain segments can be separated into groups depending upon the degree of chain extension, and overall chain orientation. Certainly, chain segments could be classified in more than two groups or even in a continuum spectrum of populations. We limit our analysis to only a few groups (specifically two) of chains, as suggested by previous simulation[38] and empirical[28] approaches, because this appears to be sufficient to describe the origin of those singular shoulders in the spectra lineshape of highly extended networks.

We argue that the outer population corresponds to segments of relatively long chains that are able to be greatly stretched and extremely oriented towards the strain axis. Therefore, such chains may not interact extensively with other chains through

entanglements. In addition, the crosslinks at the end of those chains could significantly displace along the deformation axis. Due to their lack of inter-chain interactions, these highly stretchable chains may mostly undergo desinterspersion upon network extension. Conversely, the inner population may be regarded as segments of relatively long chains that are subject to more inter-chain interactions (i.e., trapped entanglements); consequently, these chains are weakly-to-moderately oriented towards the strain axis upon large extensions.

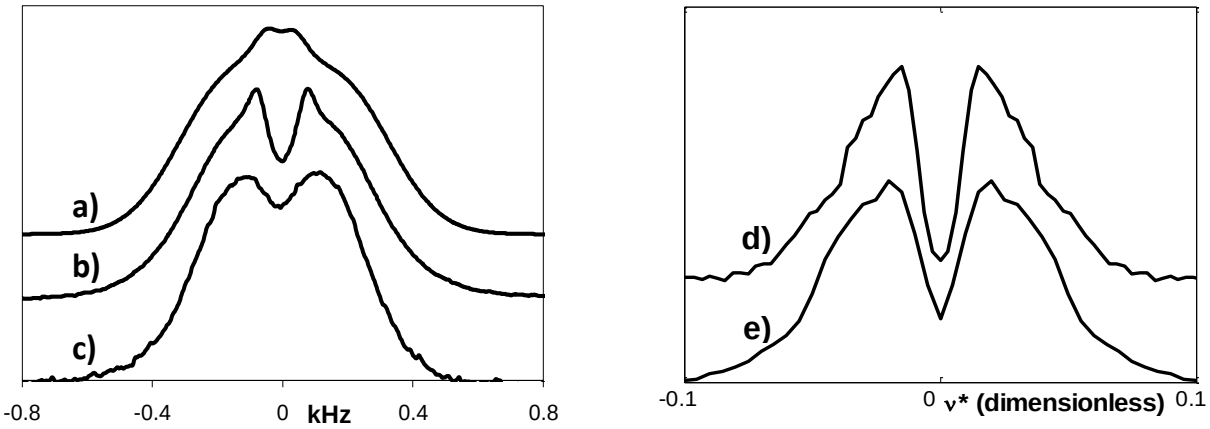

Figure 2.8: Experimental ^{2}H-NMR lineshapes for a) 60 mol % short chain bimodal network with ^{2}H-labeled long chains (α = 2.04); b) 36000 g/mol unimodal network (α = 1.98); and c) 90000 g/mol unimodal network (α = 2.26). Simulated ^{2}H-NMR lineshapes for d) 129-bead unimodal network (α = 3.05) and e) 90 mol % short chain bimodal network with long (300-bead) chains labeled (α = 2.53). For simulated networks, $\langle \nu^* \rangle$ is equal to $\langle S \rangle$.

To quantify the extent of overall chain orientation (rather than segment orientation) along the extension axis in simulated networks, we define the average chain orientation order parameter *Z* as the second Legendre polynomial of the ratio of the chain mean squared radius of gyration component along the strain axis ("z" direction) $R^2_{G,Z}$ to the total chain mean squared radius of gyration R^2_G. The order parameter *Z* is then given by:

$$Z = \frac{3R^2_{G,Z} \big/ R^2_G - 1}{2} \qquad (2.3)$$

Values of Z range from -½ (when all segments of a chain lie on a plane perpendicular to the "z" axis) to 1 (all segments of a chain are completely aligned parallel to the "z" axis). If chain segments are isotropically distributed, e.g., chains with random coil configurations, Z is equal to 0. A sketch of how Z is related to the overall orientation of the chain is displayed at the bottom right corner of Figure 2.9. This figure also shows the total dimensionless stress versus the ensemble average of Z in several simulated unimodal networks made with different chain lengths. Relatively large values of $\langle Z \rangle$, e.g., greater than 4/5, obtained for reasonable stresses (less than 0.15 in $k_B T/\sigma_{LJ}^3$ units) are only observed in networks with rather long chains. As an example of extreme chain alignment to the strain axis, chains with average Z values greater than 4/5 would exhibit average ellipsoidal-coil conformations with aspect ratios (i.e., $(\langle R^2_{G,Z} \rangle / \langle R^2_{G,Y} \rangle)^{1/2}$) greater than 3.6.

Large values of Z (i.e., greater than 4/5) are not observed for shorter chains (less than 100-bead long) because they would need to lose most of their configurational entropy to achieve such extremely oriented states. On the other hand, relatively long chains (longer than 100 beads) that lack entanglements with other chains need to lose only a part of their entropy in order to attain such aligned configurations. This could explain why the unusual shoulders in lineshapes are only seen for segments of PDMS chains with relatively high molar masses (e.g., greater than 36000 g/mol[28] that are roughly equivalent to chain lengths of 120 beads in our simulated networks).

Using this order parameter Z of overall chain orientation, we decompose the simulated spectrum of long chains (300-bead) in a highly extended bimodal network (also displayed in Figure 2.8e) into two spectra: one corresponding to weakly or

moderately oriented long chains (with ⟨Z⟩ < 4/5), and another to exceptionally oriented long chains (with ⟨Z⟩ > 4/5). Such decomposition (Figure 2.10) clearly shows that the outer shoulder (or wide splitting) arises from segments belonging to long chains that are extremely oriented and deformed towards the strain axis. The inner segment population (or narrow splitting), however, corresponds to segments of long chains that are moderately or even weakly oriented and deformed along the extension direction. Thus, the empirical approach used in reference 28 to analyze this type of complex lineshapes exhibiting two pair of doublets may be seen as phenomenologically correct. This empirical analysis could, for instance, be employed to gain insights about the relative sizes of these *"two"* chain segment populations through comparisons between the areas under the spectra of the outer and inner splittings. Moreover, this information about these two groups of long chains with different orientational responses may also be related to the network tensile properties, such as modulus, ultimate strain, and toughness.

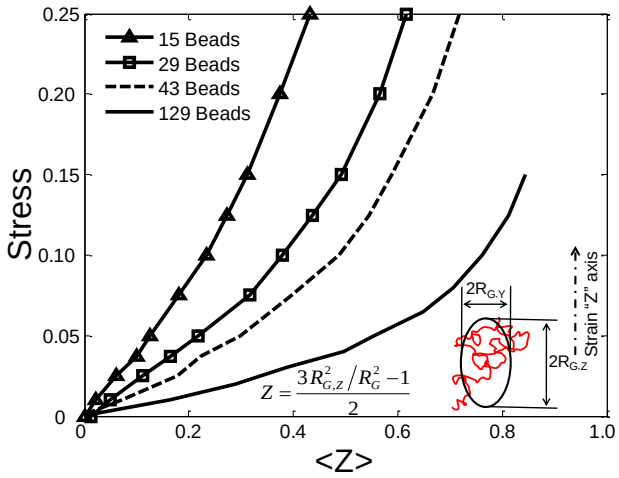

Figure 2.9: Stress (in $k_B T/\sigma_{LJ}^3$ units) vs. average chain orientation order parameter ⟨*Z*⟩ (dimensionless) for various simulated unimodal networks with different chain lengths: 15-bead long (triangles), 29-bead long (squares), 43-bead long (dashed), and 129-bead long (solid line). At the bottom, the definition of *Z*, and a sketch that illustrates the relation of *Z* to the average chain orientation.

We proceed now to analyze and compare the complex spectra observed for rather long chains in PDMS unimodal and bimodal networks through the approach used in reference 28. While the shoulders are not always as pronounced in these systems as in the 36000 g/mol unimodal network, all the PDMS bimodal long chain lineshapes were successfully fit to doublets with peak separation $\Delta\nu_w$ and $\Delta\nu_n$. These data are normalized by the elastic modulus and plotted vs. α^2-1/α in Figure 2.11a. Values of $\Delta\nu/E$ fall in the range predicted by ideal elasticity theory, $0.2\omega_Q a^3/k_B T \cong 0.14 \times 10^{-3}$ Hz/Pa, with $\omega_Q \cong 250$ kHz /12 = 21 kHz (taking local rotations into account) and $a^3 \cong (0.52\text{ nm})^3$. The $\Delta\nu_w/E$ and $\Delta\nu_n/E$ data follow universal trends for both unimodal and bimodal networks across different precursor chain lengths and compositions. This correspondence indicates that the effects of the excluded volume interactions and the constraints on segmental alignment are each linked to the average mesh size (modulus) of the bulk network. Therefore, it is surprising that the 90000 g/mol unimodal network lineshape does not display an outer shoulder (Figure 2.8c), even though the long chains in bimodal networks employed in this study (depicted in Figure 2.8a) are of the same precursor molar mass. The splitting between the peak maxima for the 90000 g/mol unimodal network are plotted in Figure 2.11b against best-fit lines generated from the unimodal and bimodal network data in Figure 2.11a. Also included are previously published data[28] for ^{2}H-labeled 30000 g/mol free chains dissolved in a protonated host network. Because these probe chains are not chemically attached to the network, their segments only align through excluded volume interactions with neighboring chains. These data follow the $\Delta\nu_n/E$ trend line as expected. Meanwhile, the $\Delta\nu$ values for the 90000 g/mol network closely follow the

$\Delta\nu_w/E$ relationship associated with segment alignment due to the effect of constraints. Thus, in Figure 2.8c the inner doublet $\Delta\nu_n$ is concealed by a more prominent outer doublet $\Delta\nu_w$ caused by segments of chains that are highly aligned due to the effect of cross-links and lack of entanglements. We attribute this lineshape characteristic to the structure of the 90000 g/mol unimodal network. This network was the only sample tested that could be classified as "non-model" due to its large soluble fraction and high degree of swelling in toluene (w_{sol} = 5.48%, Q = 7.31 – Table 2.1). The 90000 g/mol chains in bimodal networks are incorporated into networks of significantly better quality (Table 2.1) due to the associated increase in cross-link density. The molar mass between effective junctions, which takes into account the presence of trapped entanglements along the elastic chains, can be calculated from:

$$M_c = 3\rho RT/E\,. \qquad (2.4)$$

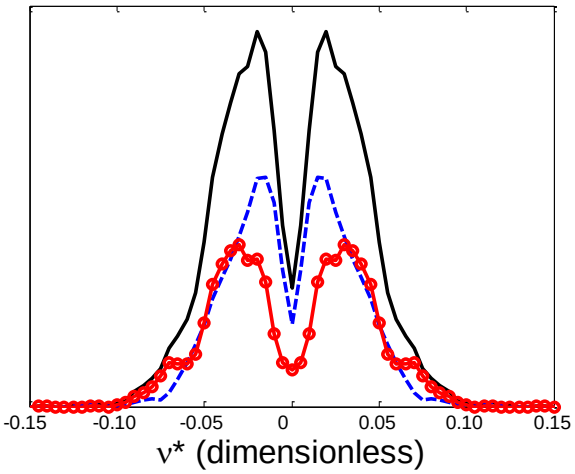

Figure 2.10: ^{2}H-NMR simulated lineshape for the 90 mol % short chain bimodal network with long chains labeled (solid line) as well as its decomposition into spectra yielded by weakly-to-moderately (dashed line) and highly (circles) oriented long chains. Chains with $\langle Z\rangle > 4/5$ are considered greatly oriented, otherwise they are considered to be weakly-to-moderately oriented. Elongation ratio α = 2.53. $\langle\nu^*\rangle$ is equal to $\langle S\rangle$.

Taking $\rho = 0.97$ g/cm^3 for PDMS and elastic modulus values from Table 2.1, we calculate $M_c = 27000$ and 12000 g/mol for the unimodal networks synthesized from 90000 and 36000 g/mol precursors, respectively. Therefore, elastic chains in both networks are expected to have about two effective junctions along their chain lengths, even though the 90,000 g/mol chains are almost three times longer than the 36000 g/mol chains. The lack of a visible "moderately or weakly oriented chain" split $\Delta\nu_n$ can then be explained by the relative reduction of interchain interactions in the longer chain unimodal network. We suspect that the presence of pendant chains and the removal of the relatively high fraction of soluble chains upon extraction led to chain interspersion (non-trapped entanglements).[43,44] Upon uniaxial extension the chains primarily disintersperse,[45] diminishing the effect of excluded volume interactions. Consequently, the segment alignment is dominated by the movement of the cross-links. This effect appears to have eclipsed the contribution of chain segment interactions between pendant chains and the elastic network, because an increased fraction of pendant chains is expected in such non-model networks.[30] The relative lack of $\Delta\nu_n$ in the 90000 g/mol unimodal network causes it to show a higher degree of average segmental orientation with respect to elastic modulus than the other unimodal networks (Table 2.1). This effect is also demonstrated by the 36000 g/mol precursors reacted in the presence of 30% non-reactive chains. After the solvent chains are extracted, this network (36000d) shows a higher degree of segment orientation than the standard 36000 g/mol unimodal network. We expect a higher contribution from disinterspersion of chains in the 36000d network due to its collapsed structure upon extraction. Table 2.1 also indicates a higher value of q for this network before removal of solvent chains (80.6 Hz/MPa) than after (73.3 Hz/MPa). This difference results

from the decreased degree of intersegmental interactions between network chains when solvent chains are present.[43,44]

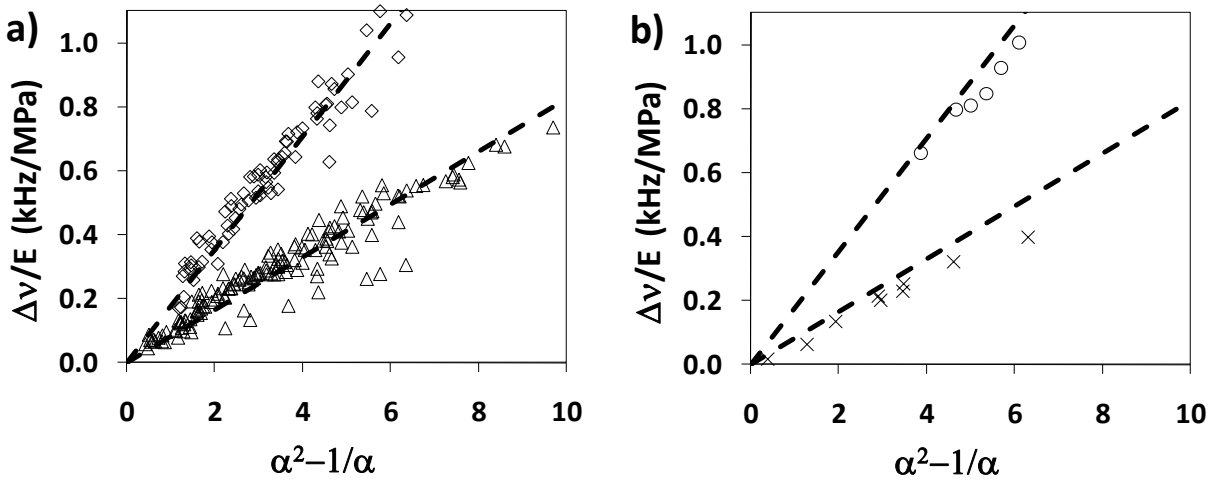

Figure 2.11: a) All data for the narrow ($\Delta\nu_n$/E-triangles) and wide ($\Delta\nu_w$/E-diamonds) spectral splittings found in ^{2}H-NMR lineshapes of unimodal and bimodal networks and the best fit lines through these data. b) $\Delta\nu$/E for the 90000 g/mol unimodal network (circles) and the 30000 g/mol ^{2}H-labeled free chains dissolved in a protonated 30000 g/mol network (x) plotted against the best fit lines generated in a).

2.4. Conclusions

Segmental ordering in bimodal networks is investigated using ^{2}H-NMR spectroscopy. We calculate the average absolute value $\langle|\nu|\rangle$ of the spectra to confirm the presence of highly oriented segments. Estimates of the total average chain segment order $\langle\nu\rangle$ are obtained from the entire ^{2}H-NMR spectrum through a recently developed methodology.[27] Even in the rest state, the lineshapes of the short and long chain components are markedly different due to the different degree of motional restriction on each. These spectral shapes are qualitatively reproduced in MC molecular simulations. The conformation of long chains is not affected when they are incorporated into a bimodal network structure. However, $\langle|\nu|\rangle_0$ values for short chains in undeformed networks evolve with bimodal composition as a result of the network topology.

Networks at about 90 mol % are of particular interest, because they have been demonstrated to produce optimal mechanical properties. Here, the high $\langle|\nu|\rangle_0$ value indicates increased motional restriction on the short chains that is likely the result of chains with a relatively high end-to-end distance during network formation. We further connect microstructure and macroscopic properties by measuring ^{2}H-NMR spectra for samples that have been uniaxially stretched. These experiments and results from the corresponding coarse-grained molecular simulations clearly demonstrate the reapportionment of segmental orientation from long to short chains with increasing short chain concentration. When their concentration is at 60 mol %, the shorter chains are found to be protected from segmental alignment since they are clustered into small domains within a medium of longer chains. Here, the segmental orientation of the shorter chains is dominated by excluded volume interactions between neighboring chains.

Optimum mechanical properties found with 90 mol % short chains are primarily due to increased mechanical loading on the short chain matrix. Wide spectral wings for these ^{2}H-labeled short chains indicate that some of these chains are moderately stretched even at the unperturbed state. The segmental alignment of the short chains is at a maximum when their concentration is further increased, but the networks become increasingly brittle. Thus, the ductility afforded by the long chain component is essential to producing bimodal networks with enhanced mechanical properties. There are likely regions dominated by long chains within these optimal networks that allow the samples to stretch without fracture even as the short chains are increasingly loaded. Although the relative orientation of short and long chain segments clearly evolves with concentration, both experiments and molecular

simulations indicate that the overall segmental alignment normalized by the elastic modulus is equal across all bimodal network compositions.

Through molecular simulations we further explored the microstructural nature of atypical ^{2}H-NMR spectra of highly extended unimodal and bimodal samples exhibiting two characteristic quadrupolar splittings. The outer splitting corresponds to segments of rather long chains that are able to be greatly stretched and oriented towards the strain axis. Conversely, the inner frequency splitting may be attributed to segments of chains that undergo more inter-chain interactions (i.e., trapped entanglements); as a result these chains are moderately or even weakly oriented towards the strain axis.

2.5 Acknowledgment.

This work was supported by the National Science Foundation Polymers Program under grant DMR-0705565.

REFERENCES

(1) Mark, J. E. *J. Phys. Chem. B* **2003**, *107*, 903-913.

(2) Andrady, A. L.; Llorente, M. A.; Mark, J. E. *J. Chem. Phys.* **1980**, *72*, 2282.

(3) Wu, W. L.; Jong, L.; Hanyu, A.; Coyne, L. D.; Stein, R. S. *Macromolecules* **1990**, *23*, 351-353.

(4) Smith T. L.; Haidar B.; Hedrick J. L. *Rubber Chem. Technol.* **1990**, *63*, 256.

(5) Oikawa, H. *Polymer* **1992**, *33*, 1116-1119.

(6) Hecht, A.; Horkay, F.; Geissler, E. *J. Phys. Chem. B* **2001**, *105*, 5637-5642.

(7) Saalwächter, K.; Ziegler, P.; Spyckerelle, O.; Haidar, B.; Vidal, A.; Sommer, J. *J. Chem. Phys.* **2003**, *119*, 3468-3482.

(8) Llorente, M. A.; Andrady, A. L.; Mark, J. E. *J. Polym. Sci., Polym. Phys.* **1981**, *19*, 621-630.

(9) Mark, J. E.; Tang, M. *J. Polym. Sci., Polym. Phys.* **1984**, *22*, 1849-1855.

(10) Mark, J. E. *Acc. Chem. Res.* **1994**, *27*, 271-278.

(11) Sotta, P.; Deloche, B. *Macromolecules* **1990**, *23*, 1999-2007.

(12) Brereton, M. G. *Macromolecules* **1993**, *26*, 1152-1157.

(13) McLoughlin, K.; Waldbieser, J. K.; Cohen, C.; Duncan, T. M. *Macromolecules* **1997**, *30*, 1044-1052.

(14) Warner, M.; Callaghan, P. T.; Samulski, E. T. *Macromolecules* **1997**, *30*, 4733-4736.

(15) Chapellier, B.; Deloche, B.; Oeser, R. *Prog. Coll. Pol. Sci. S.* **1992**, *90*, 111-114.

(16) Chapellier, B.; Deloche, B.; Oeser, R. *J. Phys. II* **1993**, *3*, 1619-1631.

(17) Sotta, P. *Macromolecules* **1998**, *31*, 3872-3879.

(18) Galiatsatos, V.; Mark, J. E. *Macromolecules* **1987**, *20*, 2631-2632.

(19) Subramanian P. R.; Galiatsatos V. *Makromol. Chem., Macromol. Symp.* **1993**, *76*, 233.

(20) Viers, B.; Mark, J. *J. Inorg. Organomet. Polym. Mat.* **2007**, *17*, 283-288.

(21) Hanyu, A.; Stein, R. *Makromol. Chem., Macro. Symp.* **1991**, *45*, 189-203.

(22) Besbes, S.; Bokobza, L.; Monnerie, L.; Bahar, I.; Erman, B. *Macromolecules* **1995**, *28*, 231-235.

(23) Sotta, P. *Macromolecules* **1998**, *31*, 8417-8422.

(24) Saalwächter, K. *J. Am. Chem. Soc.* **2003**, *125*, 14684-14685.

(25) Saalwächter, K.; Sommer, J. *Macromolecular Rapid Communications* **2007**, *28*, 1455-1465.

(26) Ries, M. E.; Brereton, M. G.; Klein, P. G.; Ward, I. M.; Ekanayake, P.; Menge, H.; Schneider, H. *Macromolecules* **1999**, *32*, 4961-4968.

(27) Aguilera-Mercado, B. M.; Cohen, C.; Escobedo, F. A. *Macromolecules* **2009**, *42*, 8889-8898.

(28) Genesky, G. D.; Duncan, T. M.; Cohen, C. *Macromolecules* **2009**, *42*, 8882-8888.

(29) Genesky, G. D.; Aguilera-Mercado, B. M.; Bhawe, D. M.; Escobedo, F. A.; Cohen, C. *Macromolecules* **2008**, *41*, 8231-8241.

(30) Patel, S. K.; Malone, S.; Cohen, C.; Gillmor, J. R.; Colby, R. H. *Macromolecules* **1992**, *25*, 5241-5251.

(31) Takahashi, H.; Shibayama, M.; Fujisawa, H.; Nomura, S. *Macromolecules* **1995**, *28*, 8824-8828.

(32) Flory, P. J. *Principles of Polymer Chemistry*; Cornell University Press, 1953.

(33) Carmesin I.; Kremer K. *Macromolecules* **1988**, *21*, 2819.

(34) Paul W.; Binder K.; Heermann D.; Kremer K. *J. Phys. II* **1991**, *1*, 37.

(35) Binder K.; Paul W. *J. Polym. Sci., Polym. Phys.* **1997**, *35*, 1.

(36) Depner, M.; Deloche, B.; Sotta, P. *Macromolecules* **1994**, *27*, 5192-5199.

(37) Sotta, P.; Higgs, P. G.; Depner, M.; Deloche, B. *Macromolecules* **1995**, *28*, 7208-7214.

(38) Yong, C. W.; Higgs, P. G. *Macromolecules* **1999**, *32*, 5062-5071.

(39) Deloche, B.; Beltzung, M.; Herz, J. *J. Phys. Lett. (Paris)* **1982**, *43*, L763-L769.

(40) Gronski, W.; Stadler, R.; Maldaner Jacobi, M. *Macromolecules* **1984**, *17*, 741-748.

(41) Trautenberg H. L.; Sommer J.-U.; Goritz D. *Macromol. Symp.* **1994**, *81*, 153.

(42) Kuhn, W.; Grün, F. *Colloid, Polym Sci.* **1942**, *101*, 248-271.

(43) Sivasailam, K.; Cohen, C. *J. Rheol.* **2000**, *44*, 897-915.

(44) Urayama, K.; Kohjiya, S. *J. Chem. Phys.* **1996**, *104*, 3352.

(45) Urayama, K.; Kohjiya, S. *Polymer* **1997**, *38*, 955-962.

CHAPTER 3

NETWORK TOPOLOGY AND MECHANICAL ENHANCEMENT IN BIMODAL NETWORKS: A MOLECULAR SIMULATION AND SANS COMBINED STUDY*

3.0 Abstract

Through both molecular modeling and small angle neutron scattering measurements (SANS), we investigate the relationships between microstructural heterogeneity, network connectivity and topology, and tensile properties in elastomeric networks made of chains with bimodal molar mass distributions. Network microstructural heterogeneity arises from purely entropic effects driven by the disparity in the fraction of chain ends and volume between the two sets of monodisperse chains. We specifically explore the impact of composition on the network topology and mechanical enhancement through Monte Carlo simulations in addition to SANS measurements on experimental PDMS samples selectively labeled with deuterium. We examine, through the use of network topological footprints, why certain bimodal polymer networks exhibit pronounced improvements of their tensile properties over those of unimodal networks with the same elastic modulus. We attribute the higher extensibility of certain bimodal networks compared to unimodal networks with similar elastic modulus to their greater spread in the distribution of shortest path lengths between all pairs of monomers. We find that optimal tensile properties, given by both high modulus and high extensibility, occur in systems where the concentration of shorter chains slightly exceeds their percolation transition and hence the extent of spatial cross-linking clustering is small.

* Chapter to be submitted to *Macromolecules* **2012**. Experimental deuterium-labeled PDMS networks used in this work were synthesized by Genesky, G. D. Detailed descriptions of the synthesis of the networks can be found on Genesky, G. D., Ph.D. Thesis, Cornell University, Ithaca New York, 2009.

3.1 Introduction

Polymer elastomers formed by end-linking two sets of chemically identical linear polymer chains whose molar mass differs by a factor of 10 or more have been of scientific interest[1–7] for some time. Such bimodal networks exhibit both a large ultimate stress and a large ultimate strain, that are not observed in unimodal networks, which generally have either a large ultimate stress or a large ultimate strain. Consequently, the toughness—amount of applied energy necessary per unit volume to deform and break the network (corresponding to the area under the strain stress curve, see Figure 3.1)—of certain bimodal networks can be much higher, due to their high modulus and ultimate strain, than that of unimodal networks with similar cross-link densities. The limited extensibility of the shorter chains has been attributed[1,7–15] to significantly contribute to the mechanical enhancement, partly evidenced by a non-linear stress upturn at larger deformations (Figure 3.1a), through augmenting the elastic modulus and the ultimate stress. Nonetheless, how short chains—only in definite composition ranges—improve the elastic modulus has not been fully explained yet. It has been reported,[5,14,15] via simulation studies, that short chains below their overlap concentration form isolated clusters leading to a highly heterogeneous network microstructure with low elastic modulus;[14] on the other hand, when short chains exceed their overlap concentration a network with larger elastic modulus and less inhomogeneous microstructure is attained.[14,15] Previous small-angle neutron scattering (SANS) measurements[16,17] have also provided strong evidence that end-linking can induce entropically driven segregation between the short chains that can eventually lead to the formation of micro-heterogeneities in bimodal networks with certain compositions.

Limited extensibility of short chains is however not the only significant factor in the mechanical enhancement of bimodal networks. More recent experimental studies[12,13] suggest that the remarkable tensile properties seen in some bimodal networks may also have a structural component. In addition, it is still unclear how the longer chains and the microstructural heterogeneities affect the compliance or pronounced extensibity of optimal bimodal networks, especially when compared to monodisperse networks with similar cross-link densities (see Figure 3.1b). It is important to emphasize that the resulting enhanced toughness observed in optimal bimodal and trimodal networks[7] strongly depends on this pronounced or extra network extensibility as much as on the modulus (Figure 3.1b). Nevertheless, most of the published works on bimodal networks center on the physical phenomena responsible for the modulus improvement and rather neglect to analyze, at least quantitatively, the underlying mechanisms of the extensibility enhancement.

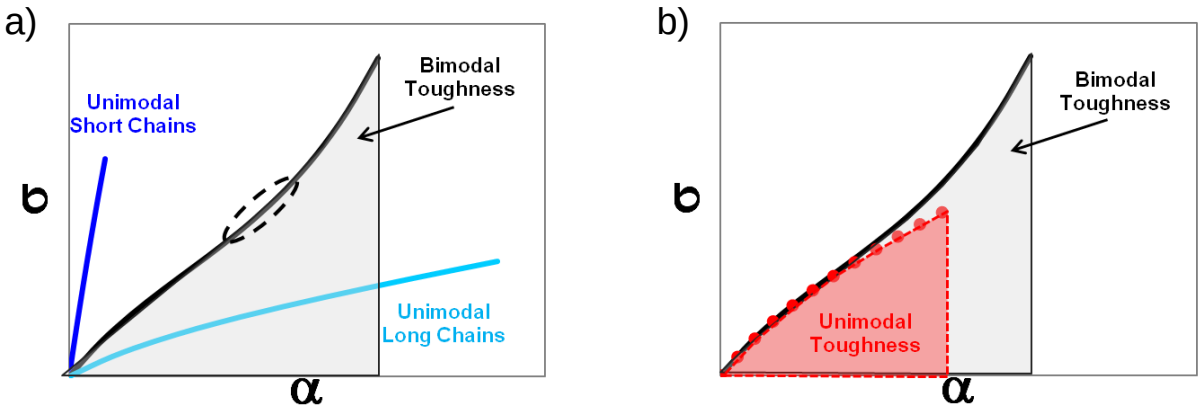

Figure 3.1: a) Depiction of the stress-strain curves of long- and short-chain unimodal networks as well as the stress-strain curve of a bimodal network with enhanced tensile strength. The improvement in toughness is shown in gray and the frequently observed stress upturn signaled by the dashed ellipse. b) Comparison between the stress-strain curves of a bimodal network with enhanced tensile strength (black/solid) and a unimodal network with the same elastic modulus (red/dots). Optimal bimodal networks exhibit larger ultimate strains than their equivalent (in terms of modulus) unimodal counterparts, what leads to significantly tougher networks.

Herein we study in more detail the relationship between the extent of heterogeneity of the network topology and the enhancement of the network elastic modulus and extensibility. We use both Monte Carlo simulations and SANS measurements of a set of bimodal polydimethylsiloxane (PDMS) networks, with chains molecular masses of 5.0-5.5 Kg/mol and 80-90 Kg/mol, spanning a wide range of compositions (0, 60, 70, 80, 90, 95, and 100 mol% of short chains) and extents of microstructural heterogeneity. Rather good agreement, in terms of both tensile responses and chain segment orientation, between these experimental and simulated sets of bimodal PDMS networks was previously reported.[14,15] Additionally, we analyze the topology of the resulting simulated networks through topological metrics borrowed from network theory[18–20] such as percolation/cluster analysis, and distribution of shortest-path lengths that have been successfully used in characterizing the topology of a great variety of systems (e.g., the world wide web, cellular and neural networks, protein folding, and disease transmission in populations).[18–20] The rest of the paper is organized as follows. In Section 3.2, we briefly describe and provide the appropriate references for the simulation and experimental methods. In Section 3.3, we first relate the extent of microstructural heterogeneities to the elastic modulus in bimodal networks. Also in Section 3.3, we present some phenomenological connections between topological metrics and both elastic network modulus and extensibility. Additionally, we suggest how these phenomenological connections between topological and mechanical properties can be further explored. In Section 3.4, we summarize with a few closing remarks.

3.2 Experimental and Simulation Methods

Both hydrogenated and randomly deuterated bimodal PDMS networks that we use in this work were synthesized and studied in an earlier work[15] on segment orientation in bimodal networks through ^{2}H-NMR measurements. We therefore refer the interested reader to this reference[15] for a complete description of the synthesis of precursor chain and the network curing. Two different sets of bimodal PDMS networks are used: 1) deuterium labeled short chains of (number average) molar mass of 5000(^{2}H) g/mol are end-linked with fully hydrogenated long chains of (number average) molar mass of 80000(^{1}H) g/mol; and 2) fully hydrogenated short chains of (number average) molar mass of 5500(^{1}H) g/mol are end-linked with deuterium labeled long chains of (number average) molar mass of 90000(^{2}H) g/mol. Table 3.1 shows the elastic modulus (E) and the soluble fractions (w_{sol}) for the networks used here. Small angle neutron scattering (SANS) measurements on the selectively deuterated bimodal networks have been performed at the National Institute of Standards and Technology (NIST) in Gaithersburg, Maryland. The reduction and analysis of the SANS data are carried out through an available processing tool that runs on IGOR pro whose methodology is described in detail in reference 21.

The simulated bimodal and unimodal networks used here are identical to the ones we used in earlier studies;[14,15,22] therefore, a comprehensive description of the simulation of the end-linking reaction (via the Bond Fluctuation Model[23]) and the uniaxial extensions (via Monte Carlo in an iso-stress ensemble) can be found in references 14, 15, 22 and the works cited therein. Simulated network characteristics are displayed in Tables 3.2 and 3.3.

Table 3.1: PDMS Network compositions and properties.

5000(^{2}H)-80000 g/mol bimodal networks

mol % short chains	E(MPa)	w_{sol} (mass %)
60	0.59	1.72
90	0.93	0.88
95	1.14	1.13
98	1.20	1.92

5500-90000(^{2}H) g/mol bimodal networks

mol % short chains	E(MPa)	w_{sol} (mass %)
0	0.27	5.48
70	0.60	1.82
80	0.76	1.01
90	0.80	2.31

The short-chain cluster identification analysis is carried out via successive products of the network Boolean connectivity matrix.[24] The Boolean connectivity matrix of a network is defined as follows: its entry (*i,j*) is equal to 1 (or True) if the i^{th} and j^{th} beads of the network are directly connected, and equal to 0 (or False) otherwise.[24] The product of such Boolean matrices is performed by substituting, in the conventional matrix product, additions and multiplications with *OR* and *AND* logical operators, respectively.[24] Successive Boolean powers of the network connectivity matrix provide detailed information on how the bead connectivities transitively map on and propagate across the network, allowing for identification and geodesic characterization of the network clusters.[24]

The shortest-path lengths for all the beads in the network (regardless of the type of chain to which they belong and also including the cross-links) are calculated

from the connectivity matrices through the Floyd-Warshall (also known as Roy-Floyd) algorithm.

Table 3.2: Characteristics of the simulated set of unimodal networks

Chain length (# of beads)	Number of chains	Number of cross-links	w_{sol} (mass%)	Inelastic cont.(mol%)
15	1659	871	0.00	5.3
29	858	472	0.00	4.4
43	579	304	0.00	2.3
129	193	111	0.00	2.6

Table 3.3: Characteristics of the simulated set of (15-300-bead) bimodal networks

Short chain cont. (mol%)	# of short chains	# of long chains	# of cross-links	w_{sol} (mass%)	Inelastic cont. (mol%)
60	110	73	105	0.07	25.1
70	169	73	121	0.13	18.2
80	268	67	185	0.25	15.8
90	490	54	286	0.00	12.7
95	778	41	451	0.00	9.3
98	1106	21	621	0.07	7.5
100	1659	0	871	0.00	5.3

3.3 Results and Discussion

3.3.1 Effect of Short Chain Clustering and Microstructural Heterogeneity on the Elastic Modulus in Simulated Bimodal Networks. Figure 3.2 shows the simulated stress-strain curves for the set of bimodal networks as well as the corresponding unimodals networks with similar elastic modulus (or cross-link densities). In agreement with the experimental set of bimodal PDMS networks,[7,14] it becomes apparent that the bimodal network with optimal tensile strength should have a molar composition of short chains between 90 and 95%. As we have not simulated the rupture of these networks, we cannot quantitatively determine the optimal bimodal network. It is worth recalling from the experimental results[7,14] that the unimodal networks made of the short chains are rather brittle and that the 60 mol% short chain bimodal network is highly extensible but its modulus is very low resulting in a weak network.

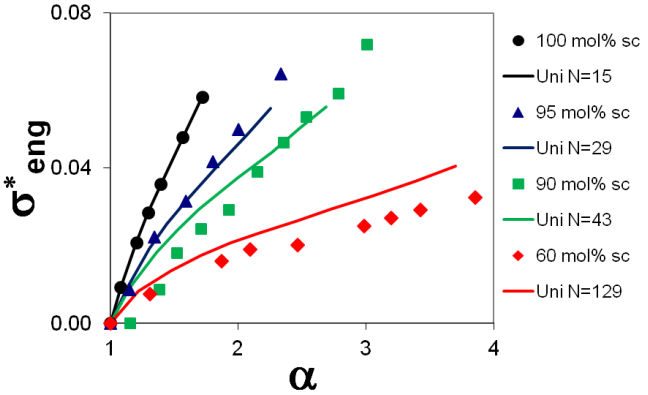

Figure 3.2: Simulated stress-strain curves for several bimodal networks (with 100, 95, 90, and 60 mol% of short chains) and the corresponding unimodal networks (with 15-, 29-, 43-, and 129-bead chains) having similar elastic moduli as those of the four bimodal networks. Stress σ^*_{eng} is in $k_BT/\sigma_{LJ}{}^3$ units.

We have found through molecular simulations that the degree of heterogeneity in the network structure (i.e., segregation of shorter chains after curing) is a strong

function of the short chain concentration, and this dependence is described by a percolation model. Figure 3.3a shows a typical percolation transition for the dependence of the fraction short chains that are part of the largest pure short-chain cluster $P_{\text{short chain}}$ on the network short chain content. $P_{\text{short chain}}$ is defined as follows,

$$P_{\text{shortchain}} = \frac{\#\text{ of short chains in the largest cluster}}{\text{total}\#\text{ of short chains}} \tag{3.1}$$

This pure-short chain cluster can be envisioned as a sub-network within the entire bimodal network. The less segregated the short chains are in the network, the greater the value of $P_{\text{short chain}}$. For instance, when $P_{\text{short chain}}$ is very close to the unity, most short chains are connected (through crosslinks and short chains only) and belong to an infinite short-chain cluster that pervades the entire space rather homogeneously. For simulated bimodal networks made of 15-mers and 300-mers, the critical percolation concentration—value at which the curve $P_{\text{short chain}}$ vs. concentration exhibits an inflexion point—is found to be around 75 mol% of short chains, which is lower than their previously reported[14] overlap concentration (95 mol%).

The degree of heterogeneity strongly influences the extent of elastic coupling among chains in our simulated bimodal networks, and ultimately determines the toughness of the network. For example, Figure 3.3b shows that the subcritical short chains in the 60 mol% (of short chains) network stretch considerably less upon extension than the supercritical short chains in the 90 mol% network. Snapshots of the bimodal networks and sub and supercritical compositions of short chains are found in Figure 3.4. On the left snapshots, short chains are colored depending on the size of the cluster to which they are attached; black short chains are the ones connected to the percolated "infinite" cluster. Short chains forming part of the percolated cluster are

elastically coupled and fully contribute to the enhancement of the modulus whereas those short chains forming part of isolated clusters poorly respond to elongation which reveals their lack of elastic coupling. This elastic coupling of the short chains is fundamental to the mechanical enhancement of bimodal networks because well coupled short chains exhibit a more even distribution of the load among them. This extent of elastic coupling between the short chains occurs for supercritical short chain concentrations; however, if the short chains concentrations significantly exceed the critical concentration, the percolated short chain cluster topology will approach that of the pure (100% short chains) short chain network. This will result in a more pronounced decrease of the ultimate strain than the corresponding improvement of the elastic modulus.

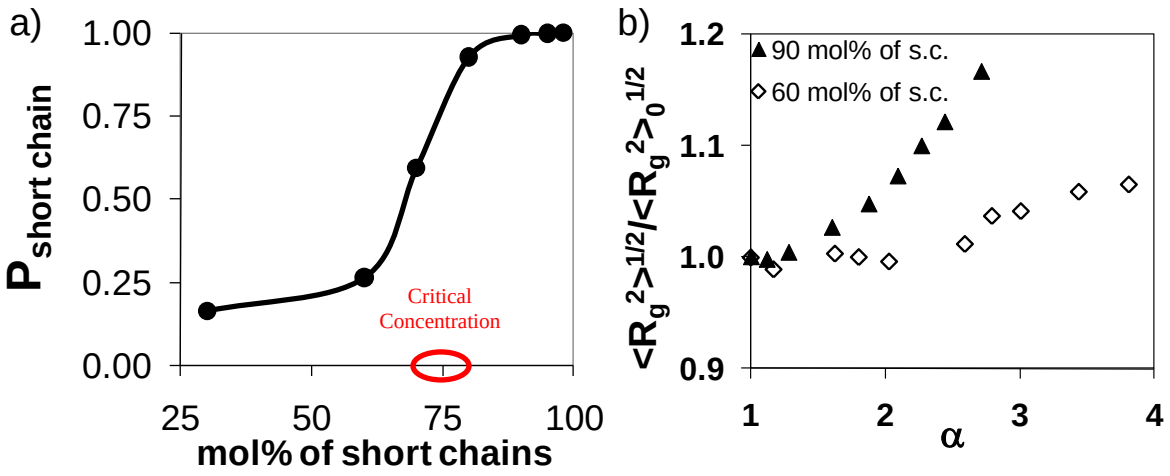

Figure 3.3: a) Fraction of short chains belonging to the largest cluster of short chains as a function of the short chain content (each composition is averaged over 25 networks). b) Relative radius of gyration (with respect to the unperturbed state) versus the elongation ratio for short chains in the 90 mol% (solid triangles) and 60 mol% (empty diamonds) networks.

Optimal tensile properties are therefore expected to occur at short chain concentrations slightly above the percolation transition when most of the short chains are elastically coupled and incorporated into a large structure of a strong but still

foldable skeleton, physically resembling a "*Swiss cheese"* (Figure 3.4, 90 mol% of short chains), as many of its inner parts are connected through longer and softer chains.

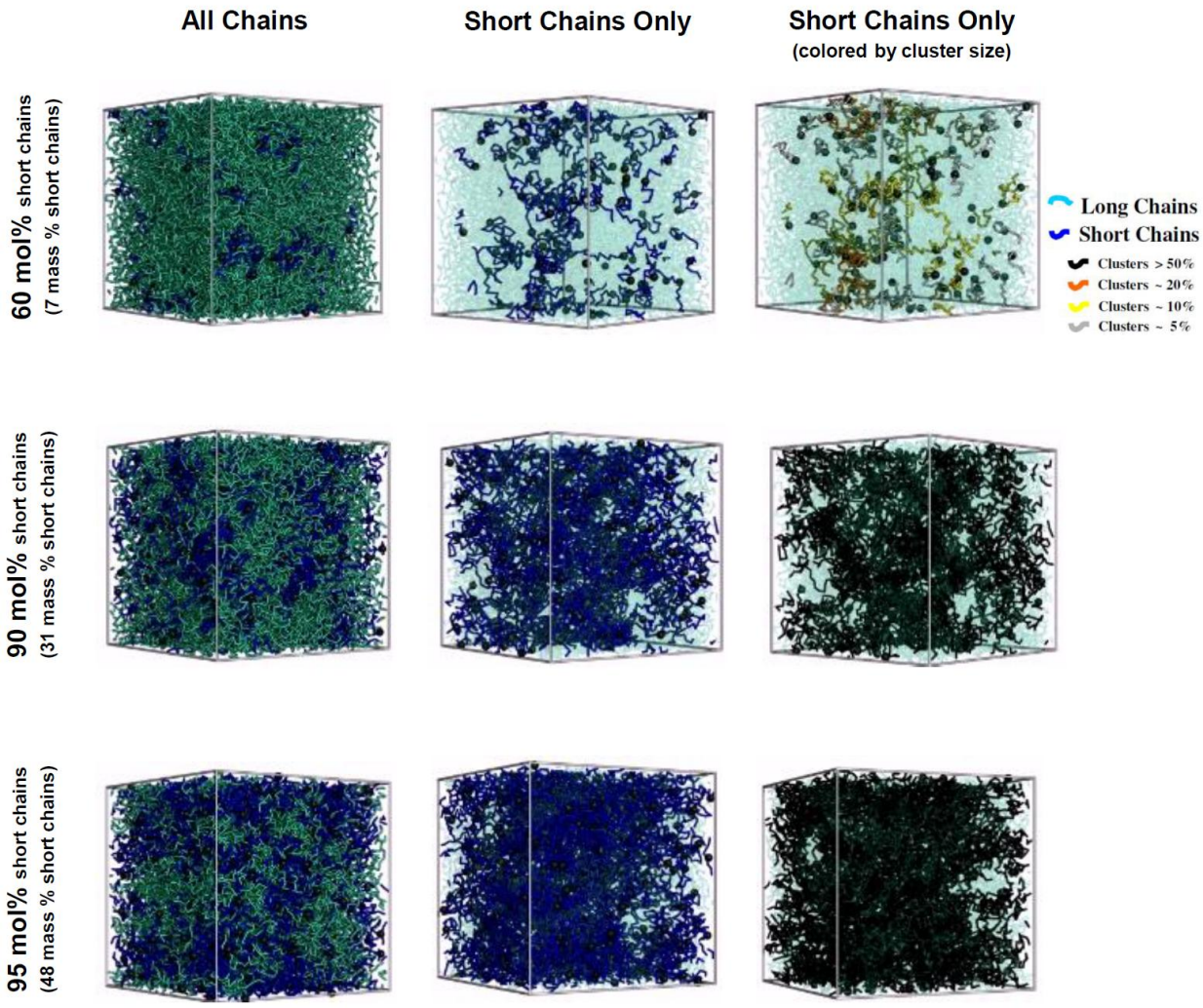

Figure 3.4: Snapshots of simulated bimodal networks at the unperturbed state for three different network compositions (60, 90, and 95 mol % of short chains). For each network three equivalent snapshots are shown: 1) with all chains, 2) only short chains (long chains are made transparent), and 3) only short chains but color-coded based on the size of the cluster they belong; chains in black form part of the percolated "infinite" cluster.

3.3.2 Exploring Short Chain Clustering and Microstructural Heterogeneity in Bimodal PDMS Networks via SANS. Figures 3.5a and 3.5b show the neutron scattering intensities I(q) as a function of the wave vector q for different sets of bimodal PDMS networks with short and long chains labeled, respectively. Properties and additional details about those two sets of bimodal PDMS networks can be found in Table 3.1. Both sets of bimodal networks have almost identical molar mass ratios of long chains to short chains, and in general are fairly similar in terms of their tensile properties dependence on the short chain content. Therefore, we proceed with our analysis assuming that: 1) the results from both sets approximately correspond to the same family of bimodal networks, and 2) this overall family of bimodal PDMS networks is represented rather well by our set of simulated coarse-grained networks described in Table 3.3. This latter assumption is supported by a previous work,[14] in which relatively good agreement was found between our set of simulated networks and a very similar set of PDMS bimodal samples to the ones used here.

In general, SANS results (shown in Figures 3.5a and 3.5b) obtained for the bimodal PDMS samples are in good agreement with what is found in the simulated bimodal networks (see discussion on network heterogeneities in previous section). For instance, bimodal PDMS networks with short chain content below or equal to 70 mol% exhibit heterogeneous structures of sizes larger than 150 nm (i.e., larger than 16 times the radius of gyration of the long chains). This is evidenced through the upturn in scattered intensities observed at low values of the wave vector ($q \approx 0.004$ Å^{-1}) for the bimodal networks with 60 and 70 mol% of short chains, shown in Figures 3.5a and 3.5b, respectively. Despite its unimodality, the network made entirely of long chains (0 mol% of short chains) also shows (Figure 3.5b) a pronounced upturn in the

scattered intensity at low q values (q≈0.004 $Å^{-1}$). We attribute this upturn in the scattered intensity to the much large size of the long chains that accordingly increases the correlation lengths between the long chains.

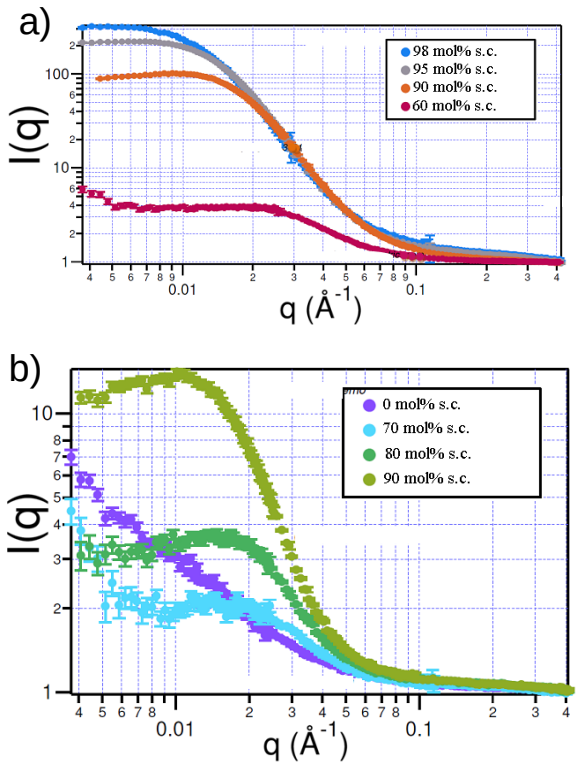

Figure 3.5: SANS spectra (scattered intensity vs. wave vector) for several bimodal PDMS networks. a) Set of bimodal networks with short chains labeled [5000(^{2}H) g/mol - 80000(^{1}H) g/mol]. b) Set of bimodal networks with long chains labeled [5500(^{1}H) g/mol - 90000(^{2}H) g/mol].

Also in agreement with simulations, networks with short chain concentrations from 80 to 90 mol% (Figure 3.5b and 3.5a) do not seem to have a great extent of heterogeneities, only modest shoulders for q values between 0.01 to 0.02 $Å^{-1}$are observed. Therefore, networks with short chain contents ranging from 80 to 90 mol % only exhibit a mild degree of structural heterogeneities with maximum characteristic sizes between 300 and 600 Å. Figure 3.5a also shows, as expected from our coarse-grained simulations, that bimodal PDMS networks with high short chain composition (higher than 95 mol%) have highly homogeneous microstructures for q values lower

than 0.015 $Å^{-1}$(i.e., sizes larger than 400 Å).

Considering that the bimodal PDMS network with optimal tensile properties, corresponding to the set of networks studied herein, is the one with 90 mol % of short chains,[14] we can rule out the hypothesis that high compositional heterogeneity and isolated clusters of short chains may function as fillers and lead to the enhancement in the mechanical properties. As previously found through simulations[14] and now experimentally confirmed in this work, only mild levels of compositional inhomogeneities, related to the hard and foldable skeleton-like structure of short chains (Figure 3.4, middle row), are associated with the enhancement of the tensile properties in bimodal networks.

3.3.3 Relating Shortest-Path Length Distributions to Tensile Properties in Elastomeric Networks. To the best of our knowledge, the impact of bimodality (or multimodality) on the ultimate strain (or extensibility) has not been quantitatively characterized in the literature. In this section we introduce a phenomenological approach to address this problem through the analysis of distributions of shortest path lengths between any two beads (any monomer or cross-link) in the network (see sketch in Figure 3.6a). Topological metrics have been used successfully[25–29] to characterize connectivity in elastomeric networks and predict its effect on the elastomer properties; for example, the cycle rank[26] of a network accurately describes the effective number of elastic strands in its structure.

The ultimate strain can depend on multiple factors such as strain rate, network connectivity, and trapped entanglements among others. Herein we solely focus on the impact of network connectivity and topology. Given that networks with equal, or very similar, modulus can exhibit very different ultimate strains (Figure 3.1b), we start

from the premise that the maximum network extensibility should not only depend on the cycle rank, number and average length of elastic chains, but also should be related to fluctuations (i.e., the distribution) of such quantities.

As a first attempt we consider to look at distributions of shortest path lengths between any pair of beads, including cross-links and monomers of both short and long chains, in the simulated networks. In principle, equivalent results could be obtained if distributions of shortest path lengths between cross-links only were considered. This would add, however, an additional level of complexity to the analysis because the average shortest path length also scales with the number of nodes of the graph analyzed. Because all simulated networks have approximately the same total number of beads (~25000) but broadly different number of cross-links, it is more convenient to analyze the total number of beads, rather than only the cross-links. Our attempt of quantifying network failure through shortest path length calculations is in part supported by the simulated results of Stevens et al.[28,29] who have successfully shown a strong relation between the minimum shortest path length and ultimate strain for grafted polymers on hard surfaces.

For every simulated network (which, as aforementioned, approximately have the same size and bead density), we compute the shortest path lengths between all pairs of beads (via the Floyd-Warshall algorithm) and obtain their normalized distributions of shortest path lengths $P(L_P)$. Consequently, in a network the fraction of pairs of beads with shortest path lengths between them ranging from $L_P - \frac{1}{2}\Delta L_P$ to $L_P + \frac{1}{2}\Delta L_P$ is given by $P(L_P)\cdot\Delta L_P$. The shortest path length L_P is in σ_{LJ} units, where σ_{LJ} denotes the Lennard-Jones characteristic bead diameter. When approximating these discrete distributions by continuous probability density distribution functions, the

following relations are defined:

$$\int_{\sigma_{LJ}}^{+\infty} P(L_P)\,dL_P = 1 \tag{3.2a}$$

$$\int_{\sigma_{LJ}}^{+\infty} (L_P)^k\, P(L_P)\,dL_P = \left\langle L_P{}^k \right\rangle \tag{3.2b}$$

and for the special case when k = -1,

$$\int_{\sigma_{LJ}}^{+\infty} \frac{1}{L_P} P(L_P)\,dL_P = \left\langle \frac{1}{L_P} \right\rangle \tag{3.2c}$$

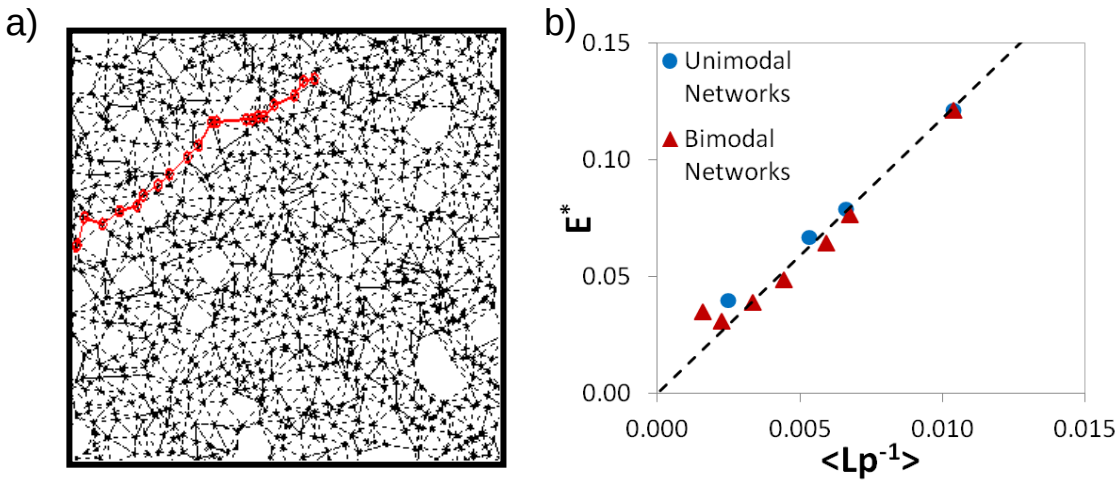

Figure 3.6: a) Sketch of the shortest path length between two nodes in a 2-dimensional network. b) Elastic modulus versus the average of the inverse shortest path length (Equation 3.2c). Elastic modulus E^* is in $k_BT/\sigma_{LJ}{}^3$ units and Lp is in σ_{LJ} units.

Ideal rubber elasticity theory predicts that the elastic modulus E scales with $k_BT/N_{\text{seg xlink}}$; where k_B is Boltzmann constant, T is the temperature, and $N_{\text{seg xlink}}$ is the number of chain segments between cross-links. As shortest path lengths also scale with $N_{\text{seg xlink}}$, a linear relationship between the elastic modulus E and $\langle L_P{}^{-1} \rangle$ is expected for networks with relatively high elastic modulus where the elastic response is dominated by cross-links rather than entanglements. As shown in Figure 3.6b, our

results corroborate this expected relationship between $\langle L_P^{-1} \rangle$ and the modulus.

In Figure 3.7 we show the calculated path length distributions for the simulated unimodal (Figure 3.7a) and bimodal networks (Figure 3.7b). As anticipated, the distributions broaden and the distribution modes become greater as the average length of precursor chains increases. As shown in Figure 3.7b, network bimodality has a significant impact on the qualitative shape of the path length distributions; in general path length distributions in bimodal networks are less symmetric around their modes, and in some cases even display a bimodal line shape (e.g., 95 mol% of short chains).

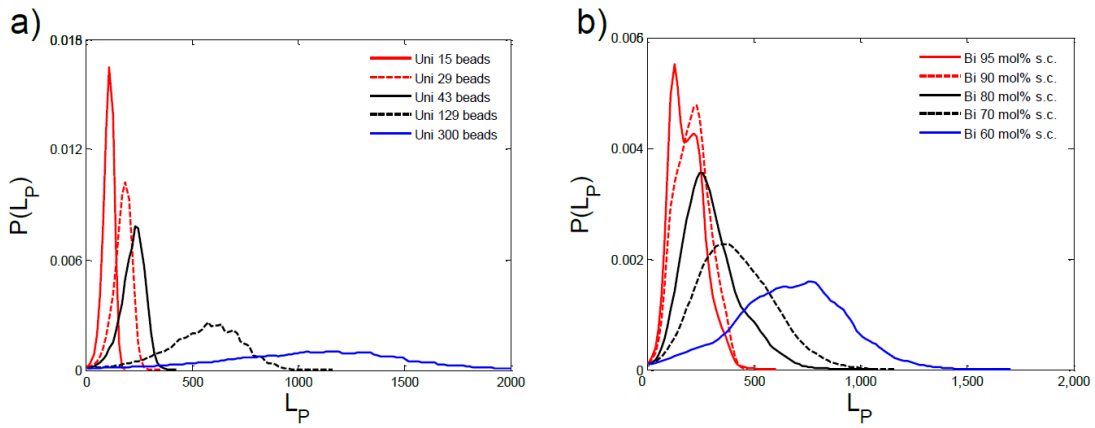

Figure 3.7: Shortest path distributions for a) unimodal networks and b) bimodal networks. Note that scales for the distributions are different for the two figures. Lp is in σ_{LJ} units and P(Lp) is in $1/\sigma_{LJ}$ units.

It is also worth noting that the path length distributions in unimodal networks are fairly self-similar, at least in networks with *relatively high* cross-link densities, as displayed in Figures 3.8a and 3.8b. This self-similarity of the scaled path length distributions suggests that the topology and connectivity in unimodal networks with *relatively high* cross-link densities are equivalent, differing only in proportion to the length of the precursor chains. Evidence shown in Figure 3.8b also suggests that the network connectivity obtained by the end-linking curing reaction can be described by

a stochastic process that follows a ("*master*") Weibull distribution, at least in networks with *relatively high* cross-link concentrations. Unimodal networks consisting of relatively long chains (i.e., with low cross-link densities) have path length distributions that deviate from the "*master*" Weibull-like distribution, but can still be described by Weibull distributions with different (smaller) value of the shape parameter.

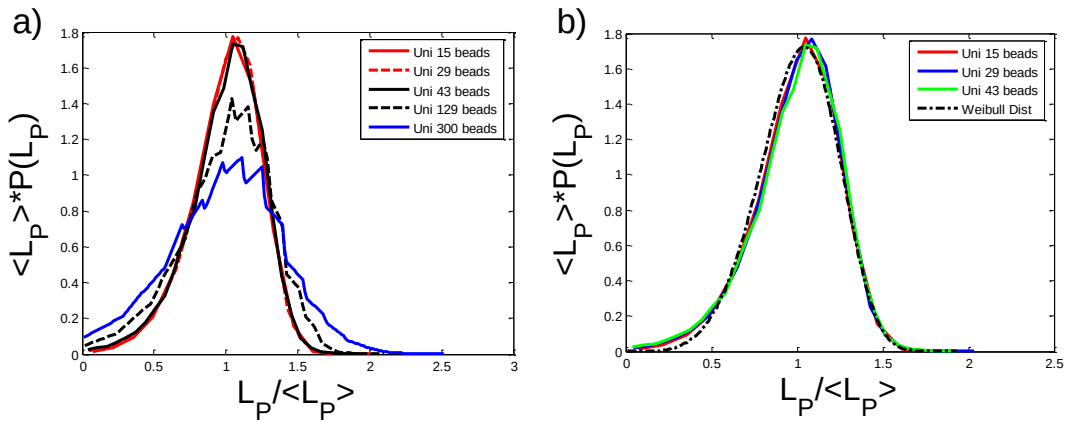

Figure 3.8: Shortest path distributions of unimodal networks scaled by the average shortest path length ⟨Lp⟩. a) All simulated unimodal networks are shown, and b) a comparison between the scaled shortest path distributions of unimodal networks with relatively high cross-link densities and a "*master*" Weibull distribution. Lp is in σ_{LJ} units and P(Lp) is in $1/\sigma_{LJ}$ units.

This observed change in the shape parameter of the Weibull-like distributions as a function of the cross-link concentration could be attributed to either lower effective values of the cross-link functionality (due to kinetic limitations undergone by longer chains) or an artifact of the simulation finite-size effects (as radii of gyration of 129- and 300-bead are comparable in size to the simulation box), which is evidenced by the less smooth shape of the distributions. Further analyses, in addition to statistical/stochastic models for the network connectivity obtained via end-linking, are necessary to precisely determine the origin of the observed dependence of the path length distribution scale or shape parameter on the cross-link density or precursor

chain length.

In Figure 3.9 we compare the scaled path length distributions of three bimodal networks to those of three unimodal networks with similar elastic modulus (see Figure 3.2 for comparisons of the elastic responses of the bimodal/unimodal network pairs). Because each pair of "equivalent" bimodal and unimodal networks have similar elastic moduli, both of their path length distributions have then similar values of $\langle L_P^{-1} \rangle$, and also rather similar values of $\langle L_P \rangle$. Therefore, the comparison of the $\langle L_P \rangle$ scaled path length distributions does not add any significant scale drift between the compared bimodal/unimodal networks of any of the three pairs, and conveniently places the three comparisons in the same range of "*universal*", and chain-length independent, values for both the L_P and $P(L_P)$.

As shown in Figures 3.9a, 3.9b, and 3.9c, bimodal networks exhibit broader path length distributions. This is more evident for the 90 mol% of short chains/43-bead and the 95 mol% of short chains/29-bead pairs of networks (Figures 3.9b and 3.9c). We attribute the remarkably enhanced extensibilities (or ultimate strains) of certain bimodal networks, compared to unimodal networks with similar moduli, to their broader path length distributions. The rationale for this is that while both networks (bimodal and unimodal) have approximately the same elastic modulus, bimodal networks will always have, due to their bimodality, a fraction of all possible chain-segment paths being able to stretch further than most of the chain-segment paths in the unimodal network (see shaded region in Figure 3.9b). This extra extensible fraction of paths plays a very important role especially at high strain values as it bears with most of the burden of the deformation. Consequently, for networks with similar moduli the higher the bimodal to unimodal path length variance ratio, the greater the

extensibility or ultimate strain enhancement.

Future work to quantitatively test this hypothesis on the relation between path length distributions and ultimate strain would involve the simulation of network failure. Such simulations are beyond the scope of this work. We can, however, extrapolate the previously reported[14] agreement in the elastic response between PDMS bimodal networks and our set of simulated bimodal networks to semi-quantitatively test our hypothesis on the network connectivity-extensibility relation. The main assumption we make here is that our simulated networks, in addition to quantitatively describe the elastic response of model bimodal and unimodal PDMS networks, also capture well enough the impact of bimodality on network topology and connectivity. While this assumption may not completely hold as the effective cross-link functionality (or the ratio of cross-links to chain ends) in the PDMS samples differ by approximately 30% from that of the simulated networks, the purpose of the following calculations is only to provide a semi-quantitative analysis.

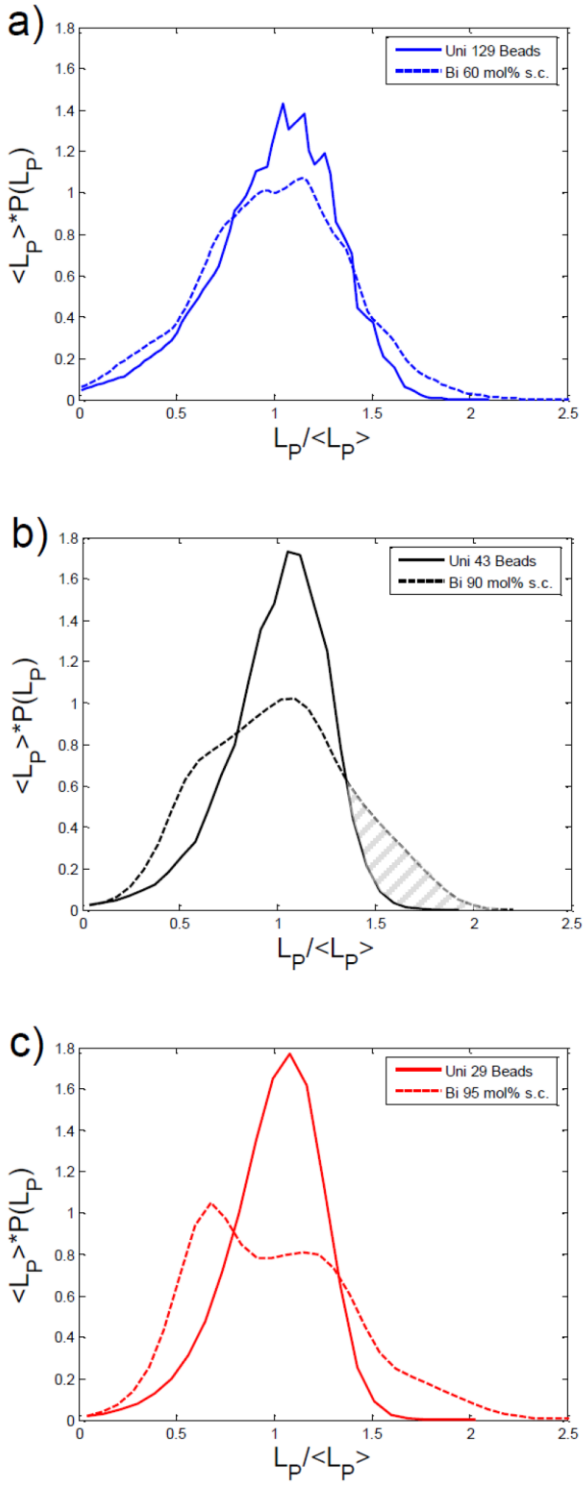

Figure 3.9: Comparison between scaled shortest path distribution functions between bimodal networks and unimodal networks with similar modulus. a) 60 mol% of short chains vs. unimodal of 129-bead chains (ratio of variances =1.4). b) 90 mol% of short chains vs. unimodal of 43-bead chains (ratio of variances =2.1). c) 95 mol% of short chains vs. unimodal of 29-bead chains (ratio of variances =2.8). Lp is in σ_{LJ} units and P(Lp) is in $1/\sigma_{LJ}$ units.

We use the conversion factor previously reported (300 g/mol per bead)[14] to estimate the equivalent molar mass, in terms of entanglement lengths, of one simulated Lennard-Jones bead of a PDMS coarse-grained chain. With this conversion factor, we find in reference 7 the closest bimodal – unimodal pairs of PDMS networks (with similar elastic moduli) to our simulated pairs of bimodal – unimodal networks. The characteristics of these (modulus) equivalent pairs (simulated and experimental pairs of networks) are as follows (% = mol %):

- (60% 15-bead + 40% 300-bead) – 100% 129-bead $\Rightarrow$

  (60% 4.5 kg/mol + 40% 91 kg/mol) – 100% 29 kg/mol

- (90% 15-bead + 10% 300-bead) – 100% 43-bead $\Rightarrow$

  (90% 4.5 kg/mol + 10% 91 kg/mol) – 100% 16.5 kg/mol

- (95% 15-bead + 5% 300-bead) – 100% 29-bead $\Rightarrow$

  (95% 4.5 kg/mol + 5% 91 kg/mol) – 100% 10 kg/mol

Ultimate strain values for the PDMS bimodal and unimodal networks listed above are available in reference 7. Bimodal to unimodal extensibility ratios are calculated for each of the PDMS bimodal – unimodal pairs of networks with similar modulus as follows,

$$\text{Extensibility Ratio} = \frac{\alpha_{u,Bi} - 1}{\alpha_{u,Un} - 1} \tag{3.3}$$

where $\alpha_{u,Bi}$ and $\alpha_{u,Un}$ are the ultimate strains of the bimodal and unimodal networks, respectively.

The bimodal to unimodal ratio of the path length variance is calculated for each of the simulated networks from

$$\text{Variance Ratio} = \frac{\left\langle L_P^2 \right\rangle_{Bi} \Big/ \left\langle L_P \right\rangle_{Bi}^2 - 1}{\left\langle L_P^2 \right\rangle_{Un} \Big/ \left\langle L_P \right\rangle_{Un}^2 - 1} \tag{3.4}$$

where the first and the second moments of the shortest path length distribution for simulated bimodal and unimodal networks are obtained from Equation 3.2b.

Figure 3.10 shows the values of the experimental extensibility ratios vs. the simulated variance ratios for the three pairs of bimodal – unimodal networks with similar elastic moduli. The extensibility ratios seem to have a strong positive correlation with the variance ratios (the approximate slope for the linear fit is 0.78). Additional and more rigorous tests are needed to assess the generality of the proposed relation between network connectivity and mechanical properties, including other multimodal and randomly cross-linked networks.

The results obtained from this semi-quantitative test suggest that the enhanced extensibility observed in certain multimodal networks has its origin in the broader distributions of shortest path length, between any two monomers, found in certain multimodal networks. Therefore, optimal mechanical properties (i.e., maximum toughness or area under the stress-strain curve) in multimodal networks should be expected to approximately occur in a network whose network connectivity and topology maximizes the product of a term corresponding to the elastic modulus (e.g., $\langle L_P^{-1} \rangle$) with another term corresponding to the network extensibility (e.g., $f(\langle L_P^2 \rangle / \langle L_P \rangle^2)$, where f is a function of the dimensionless second moment of the shortest path length distribution).

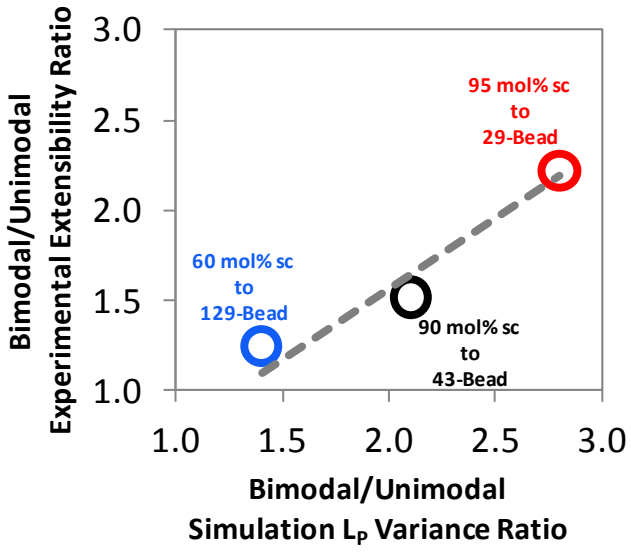

Figure 3.10: Experimental bimodal-to-unimodal extensibility ratio $(\alpha_{c,Bi}-1)/(\alpha_{c,Un}-1)$ vs. simulated bimodal-to-unimodal ratio of shortest path length distribution variance $(\langle Lp^2\rangle/\langle Lp\rangle^2-1)_{Bi}/(\langle Lp^2\rangle/\langle Lp\rangle^2-1)_{Un}$. All bimodal – unimodal pairs of networks have similar moduli.

3.4 Summary and Conclusions

Through both Monte Carlo simulations and small angle neutron scattering measurements (SANS) on PDMS bimodal networks, we find that optimal tensile properties, high modulus as well as high extensibility, occur in systems where the concentration of shorter chains slightly exceeds their percolation transition and hence spatial cross-linking clustering is small. We rule out the hypothesis that isolated clusters of short chains may contribute to the enhancement of the tensile properties of bimodal networks by acting as fillers. We explore, through the use of network topological footprints, a phenomenological approach to address why certain bimodal polymer networks exhibit pronounced improvements of their tensile properties over that of unimodal networks with the same elastic modulus. We propose that the higher extensibility of certain bimodal networks compared to that of unimodal networks with similar elastic modulus is quantitatively related to their broader spread in the

distribution of shortest path lengths between all pairs of monomers. Further work is necessary to more accurately and generally connect network connectivity and topology with such network mechanical properties as elastic modulus and ultimate strain.

3.5 Acknowledgments

This work was supported by the National Science Foundation Polymers Program under Grant DMR-0705565. The authors thank the staff of the NIST Center for Neutron Research for the beam time granted, and especially Dr. Steven R. Kline and Dr. Boualem Hammouda for their suggestions and fruitful discussions.

REFERENCES

(1) Erman, B.; Mark, J. E. *Structures and Properties of Rubberlike Networks*; Oxford University Press, USA, 1997.

(2) Llorente, M. A.; Andrady, A. L.; Mark, J. E. *Journal of Polymer Science: Polymer Physics Edition* **1981**, *19*, 621–630.

(3) Mark, J. E.; Curro, J. G. *The Journal of Chemical Physics* **1984**, *80*, 5262–5265.

(4) von Lockette, P. R.; Arruda, E. M. *Macromolecules* **1999**, *32*, 1990–1999.

(5) Sommer, J.-U.; Lay, S. *Macromolecules* **2002**, *35*, 9832–9843.

(6) Paris R., von L. *Polymer* **2008**, *49*, 5158–5168.

(7) Genesky, G. D.; Cohen, C. *Polymer* **2010**, *51*, 4152–4159.

(8) Curro, J. G.; Mark, J. E. *The Journal of Chemical Physics* **1984**, *80*, 4521–4525.

(9) Termonia, Y. *Macromolecules* **1990**, *23*, 1481–1483.

(10) Mark, J. E. *Acc. Chem. Res.* **1994**, *27*, 271–278.

(11) von Lockette, P. R.; Arruda, E. M.; Wang, Y. *Macromolecules* **2002**, *35*, 7100–7109.

(12) Viers, B. D.; Mark, J. E. *Journal of Macromolecular Science, Part A* **2007**, *44*, 131–138.

(13) Viers, B. D.; Mark, J. E. *Journal of Inorganic and Organometallic Polymers and Materials* **2007**, *17*, 283–288.

(14) Genesky, G. D.; Aguilera-Mercado, B. M.; Bhawe, D. M.; Escobedo, F. A.; Cohen, C. *Macromolecules* **2008**, *41*, 8231–8241.

(15) Aguilera-Mercado, B. M.; Genesky, G. D.; Duncan, T. M.; Cohen, C.; Escobedo, F. A. *Macromolecules* **2010**, *43*, 7173–7184.

(16) Wu, W. L.; Jong, L.; Hanyu, A.; Coyne, L. D.; Stein, R. S. *Macromolecules* **1990**, *23*, 351–353.

(17) Hecht, A.-M.; Horkay, F.; Geissler, E. *The Journal of Physical Chemistry B* **2001**, *105*, 5637–5642.

(18) Blinder, P.; Baruchi, I.; Volman, V.; Levine, H.; Baranes, D.; Jacob, E. B. *Natural Computing* **2005**, *4*, 339–361.

(19) Albert, R.; Barabási, A.-L. *Rev. Mod. Phys.* **2002**, *74*, 47–97.

(20) Newman, M. E. J. *SIAM Review* **2003**, *45*, 167–256.

(21) Kline, S. R. *Journal of Applied Crystallography* **2006**, *39*, 895–900.

(22) Aguilera-Mercado, B. M.; Cohen, C.; Escobedo, F. A. *Macromolecules* **2009**, *42*, 8889–8898.

(23) Carmesin I.; Kremer K. *Macromolecules* **1988**, *21*, 2819.

(24) Aguilera-Mercado, B. M. *Master's Thesis: Modelaje Molecular Mesoscopico de Sistemas Asfaltenicos*; Universidad Simon Bolivar: Caracas, Venezuela, 2005.

(25) Eichinger, B. E. *Macromolecules* **1972**, *5*, 496–505.

(26) Flory, P. J. *British Polymer Journal* **1985**, *17*, 96–102.

(27) Kloczkowski, A. *Polymer* **2002**, *43*, 1503–1525.

(28) Stevens, M. J. *Macromolecules* **2001**, *34*, 1411–1415.

(29) Tsige, M.; Lorenz, C. D.; Stevens, M. J. *Macromolecules* **2004**, *37*, 8466–8472.

CHAPTER 4

SAWTOOH TENSILE RESPONSE OF MODEL LIQUID CRYSTAL ELASTOMERS: A MOLECULAR SIMULATION STUDY*

4.0 Abstract

We study via coarse-grained molecular modeling the elastic response of semiflexible elastomer networks with idealized regular connectivity. A distinctive *sawtooth*-shaped stress-strain curve, reminiscent of those of some *super* tough natural materials, is found in such regular mesogenic elastomers under relatively large iso-strain uniaxial deformations (α > 3) at the nanoscale. Moreover, a perfect *soft* elastic behavior, including a bucking instability preceding hardening, is observed up to moderate extension ratios (α < 2.9) for these networks. This unique tensile response follows from a deformation mechanism that entails the successive creation and distortion of ordered (smectic C_A) chain domains in concert with crosslink segregation and layering; such events arise from the proclivity of the chains to align (due to the chain stiffness) and to disintersperse (due to the network regularity and lack of trapped entanglements). Multiple segregation states can then occur, each with a distinct α, where the stress is at a minimum. These mesogenic regular networks also exhibit a marked anisotropic elastic behavior, and pronounced shape-memory effects that can be reset upon heating. Additionally, we investigate the impact on the tensile behavior of chain stiffness, network architecture, and chemical bidispersity (by investigating end-linked semiflexible A-B-A tri-block copolymer chains). A significant enhancement in toughness and modulus is observed in regular networks with

* Chapter to be submitted to *Macromolecules* **2012**

mesogenic tri-block copolymer chains due to the further stabilization of the smectic chain domains via microphase separation of the different blocks; the creation of new smectic domains requires now more energy to access transitional states where the inter-block interfacial area must increase.

4.1 Introduction

Semiflexible polymer melts can transition, at appropriate temperatures and densities, from completely isotropic—random-coiled chains—states to ordered ones where chains align and have long-range orientation, and in some cases translational order.[1,2] When these polymer chains with limited flexibility are cross-linked to form networks, materials can result with fascinating mechanical properties, which are not simple extensions of the individual characteristics of both elastomers and semiflexible chains.[3–6] The unique tensile behavior of this class of materials originates from the strong coupling between orientation (and sometimes translational) order of mesogenic segments, and a variety of mostly non-affine deformation mechanisms such as stretching of chain-ends via reeling, unraveling, and distortion (through bending or unfolding) of fibril-like microstructures formed by bundled rod-like chains.[6–11] Some examples of such semiflexible polymeric networks with outstanding mechanical strength and pronounced non-linear elasticity can be found in both natural (e.g., fibrillar collagens,[6] actin cytoskeletal networks,[3,8,12,13] and spider dragline silks[6,14,15]) and man-made materials like liquid crystal elastomers. The range of technological uses for these semiflexible networks is very broad; for instance, liquid crystalline elastomers, which exhibit strong shape-memory effects, have found multiple applications as materials for electro-[16] and opto-mechanical[17] actuators, biosensors,[18] electro-dynamic contact lenses,[18] and artificial muscles[18–20] among others.

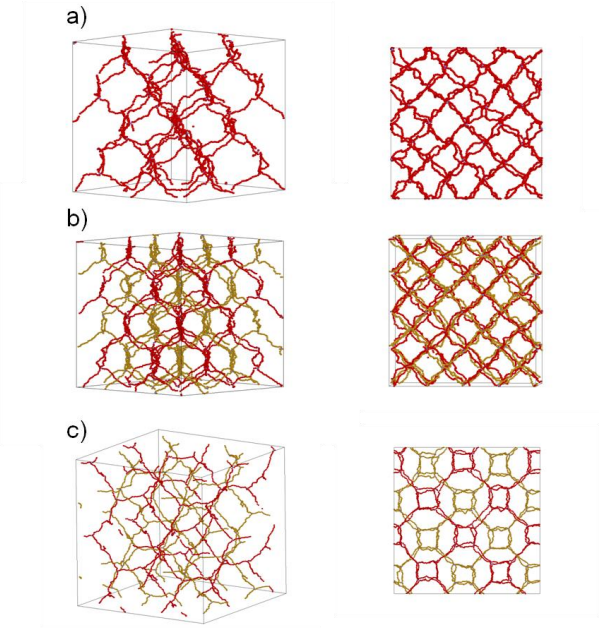

Figure 4.1: Idealized model networks with regular connectivity used in this work (fully extended). (a) Oblique (left) and frontal (right) views of a diamond network. (b) Oblique (left) and frontal (right) views of a double diamond network. (c) Oblique (left) and frontal (right) views of a double gyroid network. Strands of the idealized networks are shown in red, and for the bicontinuous networks the strands of the second interpenetrating network is shown in yellow.

It has been well established that the network microstructure can have an important quantitative, and in some instances also qualitative impact on the elastic response of liquid crystal elastomers. For example, mesogenic elastomers with superior liquid crystalline shape-memory effects have been obtained[21–23] by decreasing the number of frozen topological defects through a more homogeneous and isotropic cross-linking process. Liquid crystal elastomers that are completely free of quenched topological heterogeneities (originating from random cross-linking and trapped chain entanglements) are therefore expected to display marked and extraordinary non-linear elastic features. With the premise that less topologically heterogeneous networks can yield enhanced mechanical properties, in earlier works the elastic behavior of a defect free semiflexible network with diamond connectivity was studied via coarse-grained

molecular simulations.[24,25] Figure 4.1(a-c) displays snapshots of such defect free networks with regular connectivity; networks with diamond, double diamond, and double gyroid lattice connectivities are shown in Figures 4.1a, 4.1b, and 4.1c, respectively. The elastic response of a semiflexible diamond network showed[24,25] an atypical *staircaselike* shape arising from a stepwise extension mechanism that entails the successive and abrupt formation (via order-disorder-order transitions) of ordered chain domains that exclude the cross-links in parallel layers.

The studies on these idealized regular semiflexible networks have now become more relevant as their synthesis is becoming a tangible possibility due to the recent progress made in programmed self-assembly of molecular building blocks. Through the use of chemically and structurally tailored mesogens and rod-like polymers, a great variety of complex bi- and tri-dimensional highly regular microstructures has been obtained; for instance, honeycomb and kagome patterns,[26] DNA cubic grids,[27] and cubic as well as diamond interpenetrating networks[28] of bipyridine coordination polymers.

Herein we further study, through coarse-grained molecular dynamics, the tensile behavior of semiflexible elastomer networks with idealized regular connectivity and mesomorphic behavior. Contrary to the aforementioned previous studies[24,25] on the elasticity of semiflexible regular networks under iso-stress ensemble extensions (mimicking constant stress-rate experiments), the present work focuses on the elastic response under uniaxial iso-strain ensemble deformations (imitating constant strain-rate experiments). Because during an iso-strain ensemble deformation intermediate strain values are continuously imposed, the stress-extension ratio curve can reveal a more detailed picture of the stress-strain relationship and its underlying

free-energy landscape. The rest of the paper is organized as follows. In Section 4.2 (and in Appendix Section 4.A.1), we describe the simulation methods and model networks. In Section 4.3, the different elastic responses and deformation mechanisms corresponding to the two deformation schemes (iso-strain vs. iso-stress) are contrasted and reconciled. Additionally, shape-memory effects and tensile anisotropy are explored for the mesogenic diamond network. Also in Section 4.3, we study the impact on the tensile behavior of chain stiffness, network architecture, and chemical polydispersity (by incorporating semiflexible tri-block copolymer chains) and compare the simulated toughening mechanism to those observed in natural *super*-tough polymeric materials. Finally, in Section 4.4 we conclude with a few closing remarks.

4.2 Simulation Methods

4.2.1 Model and Method. The coarse-grained molecular model of elastomer networks used in this work consists of linear chains of Lennard-Jones (LJ) beads that are linked at the chain ends through cross-links. Cross-links are also represented as LJ beads, but with higher functionality (three or four). The characteristic length and energy scales of the LJ beads are σ_{LJ} and ε, respectively.

The potential energy between two bonded beads is given by,

$$U_{Bond}(r) = U_{EV-LJ}(r) + U_{FENE}(r) \tag{4.1a}$$

where $U_{EV\text{-}LJ}(r)$ is a purely repulsive Lennard-Jones potential, mimicking excluded volume interactions, of the form

$$U_{EV-LJ}(r)=\begin{cases}4\varepsilon\left[\left(\frac{\sigma_{LJ}}{r}\right)^{12}-\left(\frac{\sigma_{LJ}}{r}\right)^{6}+\frac{1}{4}\right] & \text{if } r/\sigma_{LJ}\le 2^{1/6}\\ 0 & \text{if } r/\sigma_{LJ}>2^{1/6}\end{cases} \tag{4.1b}$$

and $U_{FENE}(r)$ is the finitely extensible non-linear elastic (FENE) bond potential

$$U_{FENE}(r)=-\left(K_{FENE}\,R_0^2/2\right)\ln\left(1-r^2/R_0^2\right) \tag{4.1c}$$

where K_{FENE} and R_0 are, respectively, the spring force constant and the maximum length of the FENE bond. The typical values K_{FENE}= $30\varepsilon/\sigma_{LJ}^2$ and R_0=$1.5\sigma_{LJ}$ are used for the FENE parameters of coarse-grained polymer chains.[29]

Chain stiffness is modeled through the following bending potential between any two consecutive chain bonds,[30]

$$\frac{1}{k_BT}U_{Bend}(r)=K_{Bend}\left(1+\cos(\psi)\right) \tag{4.2}$$

where ψ is the angle formed between the two consecutive bonds, k_B is the Boltzmann constant, T is temperature and K_{Bend} is the chain stiffness constant (in k_BT units). No bending potential is used if any of the two consecutive bonds involves cross-links, which hence renders a fully flexible cross-linking between chains. The persistence length of the chains at a given temperature T is monotonously dependent on K_{Bend}.[31] In this work we vary K_{Bend} from 0 to 5 which covers the range from fully flexible (free chain persistence length ~ $1.3\sigma_{LJ}$ in θ solvent) to stiff/mesogenic chains (free chain persistence length ~ $4.8\sigma_{LJ}$ in θ solvent).

Non-bonded beads interact via a cut and shifted Lennard-Jones potential,

$$U_{LJ}^{i,j}(r)=\begin{cases}4\varepsilon^{i,j}\left[\left(\frac{\sigma_{LJ}}{r}\right)^{12}-\left(\frac{\sigma_{LJ}}{r}\right)^{6}-\left(\frac{\sigma_{LJ}}{r_c^{i,j}}\right)^{12}+\left(\frac{\sigma_{LJ}}{r_c^{i,j}}\right)^{6}\right] & \text{if } r/\sigma_{LJ}\le r_c^{i,j}\\ 0 & \text{if } r/\sigma_{LJ}> r_c^{i,j}\end{cases} \quad (4.3)$$

the values used for the interaction energies, $\varepsilon^{i,j}$, and cutoff distances, $r_c^{i,j}$, depend on the type of system studied. Specifically, for model elastomer networks made of homopolymer chains only (i.e., first part of this study) we use $\varepsilon^{i,j}=1.0\varepsilon$, and $r_c^{i,j}=2^{1/6}\sigma_{LJ}$; and for elastomer networks containing A(25%)-B(50%)-A(25%) tri-block copolymer chains (second part of the study) we use $\varepsilon^{i,j}=1.0\varepsilon$ for all the interactions and $r_c^{i,j}=2.5\sigma_{LJ}$ if beads i and j are chemically identical (resulting in a potential with an attractive well), or $r_c^{i,j}=2^{1/6}\sigma_{LJ}$ if beads i and j are chemically different (resulting in a purely repulsive potential). As a point of reference, a melt consisting of these 20-mer block copolymer chains (at $T= 2.0\varepsilon/k_B$ and $\rho = 0.85\sigma_{LJ}^{-3}$), with the above described interaction potentials, has an effective Flory-Huggins parameter of approximately $\chi N \approx 63$.[32]

In systems containing tri-block copolymers, cross-links have a different "chemical identity" to those of the two blocks. Cross-links are, consequently, slightly attracted to themselves (i.e., $r_c^{i,j}=2.5\sigma_{LJ}$ for interactions between cross-links), and beads belonging to any of the chain blocks interact repulsively ($r_c^{i,j}=2^{1/6}\sigma_{LJ}$) with cross-links. An additional set of simulations was performed for tri-block copolymer networks with cross-links having the same "chemical identity" as that of the chain ends (A-blocks); the tensile responses of this system were found to be almost identical to those of the previous case and hence will not be reported.

Molecular dynamics (MD) in the canonical (NVT) ensemble is used to equilibrate and simulate the deformation of the model elastomer networks. Newton's equations of motion are integrated using a velocity Verlet algorithm[33,34] and the Andersen thermostat[33] is employed to impose the desired temperature, which is $T^*= k_BT/\varepsilon = 2.0$ in most of the studied cases. Periodic boundary conditions are used in all directions of the orthorombic simulation box. The time step used for the integration is $\Delta t=0.005\sigma_{LJ}\ (m_{LJ}/\varepsilon)^{1/2}$, where m_{LJ} denotes the mass of the LJ bead, and the collision frequency of the Andersen thermostat is $\nu=10.0\ (\varepsilon/m_{LJ})^{1/2}/\sigma_{LJ}$.

4.2.2 Network Uniaxial Deformation. Following network creation and equilibration (see details in the Appendix Section 4.A.1), we uniaxially deform the networks via MD simulations in a quasi-continuous manner as well. The extension ratio α, defined as quotient of the box z-length (at any time during the deformation process) to the initial undeformed box z-length, is changed gradually by $\Delta\alpha=10^{-4}$ every 5000 MD time steps (i.e., the deformation is carried out at a constant strain rate of $d\alpha/dt=4\times10^{-6}\ (\varepsilon/m_{LJ})^{1/2}/\sigma_{LJ}$). For networks made of tri-block copolymer chains the strain rate used is $d\alpha/dt=8\times10^{-6}\ (\varepsilon/m_{LJ})^{1/2}/\sigma_{LJ}$. The box x- and y-lengths are varied concertedly to simulate a constant-volume uniaxial deformation. Similarly to the equilibration runs, all the energetic interactions appropriate to the particular system being deformed are fully active. The simulation temperature is $T=2.0\varepsilon/k_B$, except for some additional equilibration runs performed at higher temperatures when exploring the hysteretic tensile response in networks with regular connectivity.

At every time step, we calculate and collect values of the quantities of interest such as stress tensor components, bending angle ψ, and chain segment orientation

parameter *S*. This order parameter *S* is defined as $3/2\times\langle cos^2(\theta)\rangle$-1/2 where θ denotes the angle between a chain segment and the strain axis, and the angular brackets represent average over all chain segments. The individual components of the stress tensor are computed from the virial contributions of all the energetic interactions involved; those corresponding to the bending potential, a three-body force field, are calculated using the methodology described by Carpenter.[35] Values of the aforementioned quantities are averaged over extension ratio intervals of width $|\alpha_{i+1}-\alpha_i|=10^{-2}$, and reported at the midpoint of the intervals $(\alpha_{i+1}+\alpha_i)/2$. Note that although we impose a "strain rate", the stress is always evaluated for a system at a given strain; i.e., in an "iso-strain" ensemble. For this reason we refer to results from these simulations as "iso-strain" deformations.

The effects of the simulation finite size and the strain rate on tensile response were specifically assessed for a 20-mer diamond network with chain stiffness constant K_{Bend}=4.0 and T^*=2.0. These analyses were performed by comparing strain-stress results from the base network with simulation results of an eight-fold larger 20-mer diamond network and, the base 20-mer diamond network deformed at a 10 times slower strain rate. While some small quantitative discrepancies are found in both comparisons, especially for the finite size effect, the qualitative features of the stress-strain curves remain unaffected.

4.3 Results and Discussion

4.3.1 Tensile Response in Liquid Crystal Elastomers with Idealized Regular Topology. In this subsection we study the elastic response of a 20-mer diamond network with stiff (mesogenic) chains (K_{Bend}=5; T^*=2.0) subject to a uniaxial iso-

strain deformation (i.e., where the strain rate is imposed and the resulting stress is measured for a given elongation).

As shown in Figure 4.2a, the stress-elongation ratio curve for this network exhibits a distinct oscillatory or *sawtooth* shape. Unlike these iso-strain results, the elastic response curve under an iso-stress deformation—in which the stress is imposed and the resulting extension ratio is measured— was found to have a *staircaselike* shape.[24,25] Note that in actual uniaxial deformation experiments an iso-strain ensemble corresponds to a "strain ramp" tensile test, whereas an iso-stress ensemble mimics a "force ramp" tensile assay. The discrepancy between the shapes of the stress-extension ratio curves for the two deformation schemes (iso-stress vs. iso-strain) is due to the different thermodynamic ensembles associated with them that do not always necessarily sample the same states of the system.

The non-monotonous, *sawtooth* shaped, dependence of stress with extension ratio (e.g., Figure 4.2a) indicates that multiple states of the system can have the same stress but with different extension ratios, and will not be all accessible to an iso-stress ensemble. This is because in an iso-stress ensemble, where the macrostate of the system is defined for a given stress value, the specific microstates visited will depend on deformation history in a system with a non-monotonous tensile response. In contrast, several states with equal stress values and different extension ratios can be readily sampled in an iso-strain ensemble as the state of the system is defined by fixing the extension ratio.

Results from an iso-strain ensemble are consequently expected to encompass those obtained from an iso-stress ensemble and provide a more complete picture of the stress-extension ratio dependence and its underlying free-energy landscape. In a

simulation at fixed stress value σ, the system will tend to settle at the lowest strain value where the same stress σ occurs in the iso-strain ensemble simulations. Hence, isostress runs will visit the α regions where the upturns of the stress "teeth" occur (first encountered when coming horizontally from the left with fixed σ). Figure 4.2b sketches how the previously reported[24,25] iso-stress *staircaselike* stress-extension ratio curve can be mapped from the iso-strain *sawtooth* shaped curve. Similar mapping and qualitative discrepancies between the—non-monotonous—tensile responses under both iso-strain and iso-stress deformations have been experimentally observed[36] for main-chain liquid crystal elastomers undergoing necking instabilities (during strain induced polydomain-monodomain smectic transitions).

In addition to its distinct *sawtooth* shape, the tensile response of the moderately stiff diamond network displays other remarkable features (see Figure 4.2) such as a liquid-like behavior (i.e., null elastic modulus) at small deformations ($\alpha \approx$1.0-1.4), very small negative stresses at moderate deformations ($\alpha \approx$1.6-2.6), and pronounced strain hardening at larger elongation ratios ($\alpha \approx$2.7). Such nonlinear and atypical elastic features are characteristic of ideal liquid crystal elastomers and described by the so-called *neo-classical rubber elasticity theory*.[4,7,37–41]

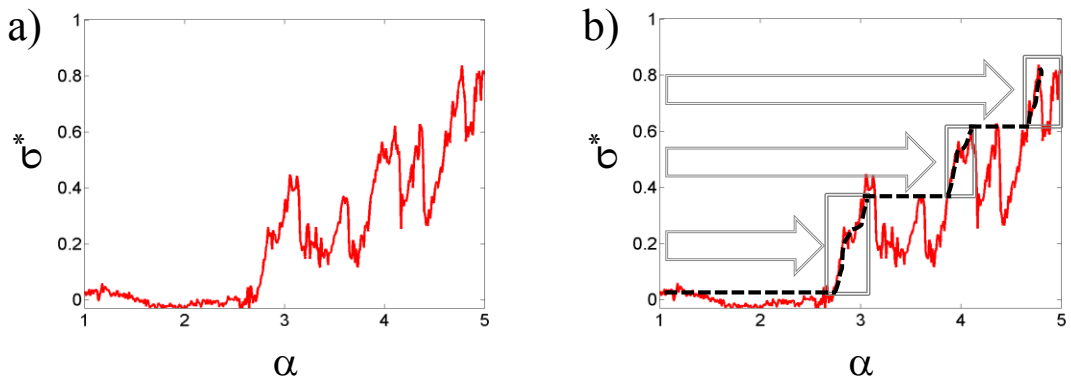

Figure 4.2: (a) "*Sawtooth-shaped*" stress-elongation ratio (σ^*vs. α) curve for a 20-mer diamond network with K_{Bend}=5 under uniaxial iso-strain ensemble deformations (T^* = 2.0). (b) Depiction of the "*staircaselike*" stress-elongation ratio curve for the same system under a uniaxial iso-stress ensemble deformation (dashed) mapped from the iso-strain deformation curve (full line). Boxes delimit the portions of the iso-strain deformation curve that are likely to be visited in iso-stress ensembles, and arrows illustrate the evolution of the elongation ratio for a given range of applied stress. In both figures stress σ^* is in k_BT/σ_{LJ}^3 units.

This liquid-like behavior (the ability to undergo finite deformations at no energy cost) is usually referred to as *soft elasticity*.[4,7,37–41] According to the *neo-classical rubber elasticity theory*, *soft elasticity* in ideal nematic elastomers originates from a *rotational invariance*[38] of the network free energy, with respect to the orientation of its nematic director, that results from a strong coupling between nematic order and applied deformation. As a consequence of this free energy *rotational invariance*, a continuous manifold of infinite macrostates with nonzero strains, known as soft (or Goldstone) modes,[4,37] arises and allows for rotations of the chain nematic directors—coupled with chain deformations—that occur at constant (and maximal) configurational plus orientational entropy of the chains.[4,7,41] Consequently, the stress-strain curve of an ideal liquid crystal elastomer would have two different and well defined regimes:[42–44] first, a *soft* one (with null elastic modulus) at a small yet finite range of strain values (where nematic orientation and deformation are fully coupled); followed by a second *hard* regime with a finite elastic modulus when mesogenic

molecules are moderately aligned and further chain deformations can no longer take place at constant configurational plus orientational entropy.

Another expected feature of ideal nematic elastomers during an iso-strain uniaxial extension, for imposed strain values near hardening, is the buckling—or Euler strut—instability (i.e., spontaneous expansion of the clamped elastomeric sample).[7] This instability occurs because, for a perfect liquid crystal elastomer, the derivative of the free energy landscape with respect to the strain is negative for strain values slightly below the *hard* transition.[7] In a uniaxial deformation setup that does not allow for sample buckling like ours, such instability is manifested through negative stress values for strains preceding the transition to the *hard* regime.

Nonetheless, real nematic elastomers[18,17,45–51] do not exhibit a perfect *soft elasticity*, and some[52] may not even show signs of a strong coupling between nematic order and applied strain. Actual liquid-crystal elastomers, due to their topological and compositional heterogeneities, require the application of a small non-zero force (and its corresponding small amount of work) for its deformation[7,41,53] during the rotation of the nematic director. Such departures from ideality due to network inhomogeneities also eliminate the possibility of regions with negative stresses.[7] This realistic and experimentally observed tensile response is known as *semisoft elasticity*,[4,7,50] and is theoretically described in terms of three separate elastic regimes: 1) *hard*, 2) *semisoft*, and 3) *hard*.[4,7,50] Significant finite values for the elastic moduli are the main characteristic of the *hard* regimes as opposed to the *semisoft* regime that displays much smaller elastic moduli. Considerable deformations can thus be performed with only a small amount of applied energy in the intermediate *semisoft* regime, during which nematic order and chain deformations are strongly coupled. In range of strain

values, the first *hard* regime is generally the narrowest and the last hard regime can last up to the material rupture.

More recently, nematic elastomers with much less topological and compositional heterogeneities have been created[21–23] by cross-linking the mesogenic polymer chains in the high temperature isotropic state and then cooling the resulting liquid crystalline elastomer to an aligned state. Such elastomers exhibit a small amount of non-idealities and hence a nearly ideal *soft* elastic tensile response. This pseudo *soft* elastic response of isotropically cross-linked mesogenic chains has been termed *super*(semi)*soft elasticity*.[22,23] However, the extent of network microstructural inhomogeneities in such isotropically cross-linked nematic elastomers is still enough to prevent a perfectly soft elastic response. Conversely, our model elastomer of stiff (mesogenic) chains with regular connectivity displays a completely ideal *soft* elastic response—including the bucking instability before the network hardening—up to moderate deformations ($\alpha < 3.0$), by virtue of the lack of frozen orientation defects (that would arise from both randomly placed cross-links and chain entanglements). Absence of such quenched orientation defects allows for a complete coupling of nematic order and chain deformation and Goldstone *soft* modes. Further consequences of the network regular topology on the tensile response, especially for larger elongation ratios, are discussed in the following subsection.

4.3.2 Non-affine Deformation Mechanisms: Successive Formation and Distortion of Smectic Chain Domains. The reported stepwise deformation mechanism[24,25] (*staircaselike* stress-strain curve) for an approximately equivalent stiff diamond network subject to an iso-stress uniaxial deformation was attributed to the abrupt and discrete formation of ordered chain domains that exclude the cross-

links.[24,25] For any given value of applied stress, the resulting equilibrated state of the system exhibits a definite number of ordered chain (and cross-link) domains which only occur over very narrow intervals of elongation ratio, giving a *staircaselike* shape to the stress-strain curve.[24,25] Moreover, it was reported[24,25] for such iso-stress deformations that the stepwise extension and corresponding shift between equilibrated states (e.g., from two to three ordered chain domains) involved an order-disorder-order transition. Specifically, upon a significant increase in the applied stress (enough to overcome the free-energy barrier between successive equilibrium states), the state with "*n*" ordered domains undergoes first a destruction of its segregated structure (during which cross-links become uniformly distributed) followed by the formation of a new segregated structured with "*n*+1" ordered domains (where cross-links are again excluded in well defined parallel layers).[24,25]

Despite the different deformation scheme and corresponding tensile response, the structural features of ordered chain domains and cross-links segregation remain unchanged under iso-strain deformation (Figure 4.3a). These strain-induced ordered domains are in fact smectic phases of the stiff—liquid crystalline—diamond network, because the mesogenic chains are not only aligned but also organized into layers, as evidenced in Figure 4.3a. Some chains may, however, form smectic defects by traversing cross-link layers and have chain sections inside the cross-link domain, or in an adjacent chain domain; examples of such defective chain configurations have been observed in a previous[2] work. It is important to stress that although strain-induced smectic phases can occur frequently in certain liquid crystal elastomers,[36,48,54–60] cross-link exclusion and layering due to the chains mesomorphic activity is rather atypical.

The observed layering and segregation of cross-links upon extension can be

attributed to the combination of three factors: regular topology of the network, strong smectic field, and cross-link flexibility. Regular connectivity and no trapped entanglements allow chains to suitably rearrange mostly through disinterspersion,[24,25] and also to strengthen the smectic field due to the lack of frozen topological heterogeneities. In addition, lattice-like connectivities can favor the cross-links layering as lattice nodes are usually layered as well. A high mesogenic field (a strong function of temperature, chain stiffness, density, and strain) is also essential to highly align the chains, and drive the microsegregation between the mesogenic chains and the more branched and isotropic network sections (i.e., the four-functional fully flexible cross-links) into separate alternating layers.

A deformation mechanism different from the aforementioned stepwise behavior[24,25] is expected to occur during an iso-strain uniaxial extension. This is because, by definition, the elastomer networks are forced to take on a continuous set of strain values (as opposed to the discrete set previously observed[24,25]) during the simulated deformation experiment. The overall deformation mechanism observed under iso-strain elongation is highly non-affine and depends on successive creation and distortion of the smectic chain domains. Contrary to the abrupt order-disorder-order transitions occurring during iso-stress deformation, such domain creation processes occur now more smoothly, reflecting the much slower "dynamics" imposed on the process.

For very small strains values ($\alpha \approx$1.0-1.4), where the elastic modulus is null, the deformation happens at constant entropy by a simultaneous rotation of the nematic director with minor chain deformations and cross-link rearrangements. Note that this stiff (K_{Bend}=5; T*=2.0) diamond network exhibits a nematic phase at the undeformed

state (α =1.0), where most of the chains are moderately oriented perpendicular to the direction arbitrarily pre-chosen as the strain axis, and its average chain segment orientation parameter *S*, with respect to the strain axis, is -0.22 (Figure 4.3c). Additional evidence on the anisotropy of the stiff diamond network at the undeformed state is discussed in Section 4.3.4.2.

In the range of elongation ratios from α =1.4 to 1.6, a nematic-smectic phase transition occurs which can be pinpointed by observing the sequence of snapshots as a function of strain (see movie in the Supplemental Material), and by the change in the slope of the order parameter *S* with respect to α (Figure 4.3c). This newly formed smectic phase is somewhat frustrated because the distance between consecutive domains of layered cross-links is shorter than the characteristic length of the "packed bundle" of mesogenic chains. As a result, chains form an anticlinic smectic C (Sm C_A) phase rather than further bend or reduce their characteristic length by increasing their number of hairpins (see deformation video in Supplemental Material or the SmC_A phase formed at α =2.0 in Figure 4.4d). This *accordion-like* arrangement of the ordered chain domains is responsible for the negative stresses (i.e., bucking instability) observed in the α ≈1.6-2.6 strain interval before network hardening. The elastic buckling instability arises from the fact that the *accordion-like* configurations entropically favor mildly folded *bellows* of chain domains over highly folded (or extended) ones.

For extension ratios ranging from 1.6 to approximately 2.9, the dominant deformation mechanism is the expansion of *bellows* of the bundled chains rather than stretching the chain ends or significantly changing the internal configuration of the

chains. When $\alpha \approx 2.7$, the stress is close to zero, signaling an "equilibrium" structure of that specific (first) *accordion-like* Sm C_A phase. Above this, around $\alpha \approx 2.9$, the *bellows* become fully extended (see video in Supplemental Material) with the chain domains forming now a Sm A phase, and the orientation order parameter *S* reaching a maximum (Figure 4.3c).

Beyond this first maximum in order parameter *S*, the expansion of chain domain *bellows* stops being the dominant extension mechanism. This is because the Sm A phase, where most of the chains are extremely aligned to the strain axis, cannot be further stretched without affecting the internal configuration of the chains (e.g., Figure 4.3a at $\alpha = 2.95$). Consequently, when ordered chain domains are arranged in a Sm A phase, the main deformation mechanism becomes hairpin unfolding of chains. In strong nematic (or smectic) fields, main-chain mesogenic polymers randomly incorporate hairpins along the chain to increase their configurational entropy, and to compensate for the orientation entropy lost due to their high alignment.[11] This has been observed experimentally,[61] described theoretically,[11] and reported in simulations of stiff diamond networks[24,25] (as "U-shaped chains").

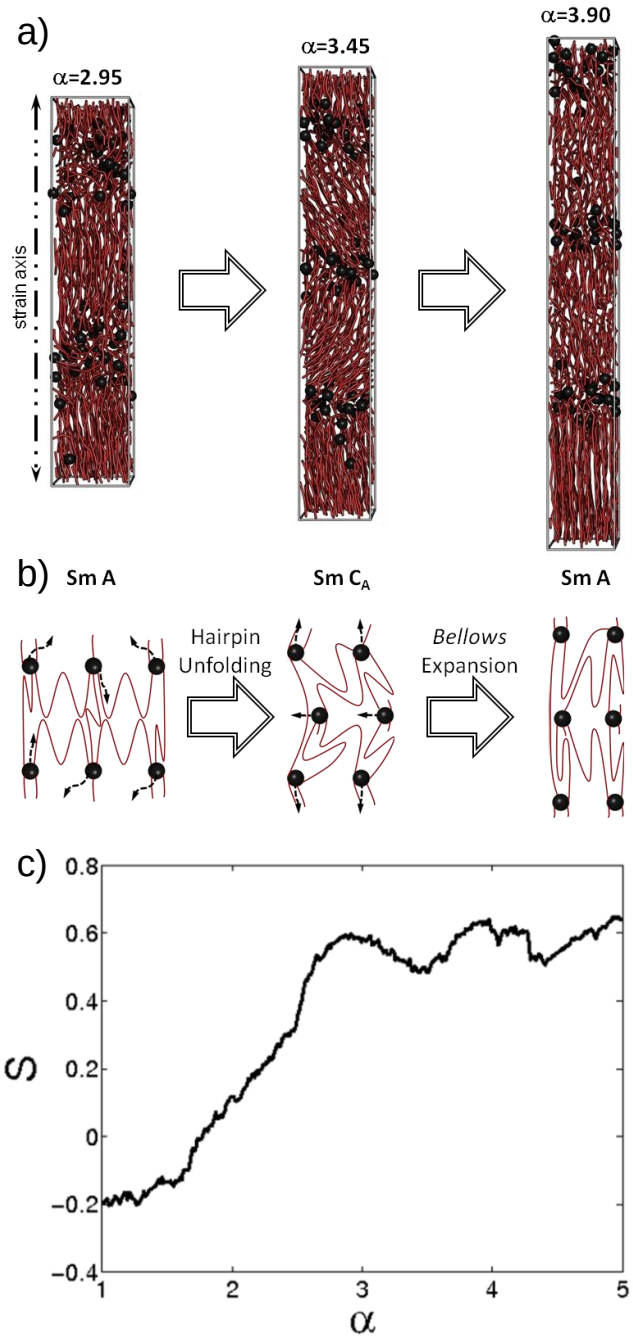

Figure 4.3: Iso-strain uniaxial deformation of 20-mer diamond network with K_{Bend}=5 and T* = 2.0. (a) Simulation snapshots at different elongations (α = 2.95; 3.45; 3.90). Different liquid crystalline smectic phases, formed by the chain and cross-link domains, are observed depending on the extension ratio. (b) Simplified sketch of the iso-strain deformation cycle of mechanisms with chain (and cross-link) domain creation (observed for $\alpha > 2.9$). (c) Ensemble average of the segment orientation order parameter "S" vs. extension ratio "α". In both figures a) and b) black beads and red strands represent cross-links, and mesogenic chains respectively.

For $\alpha \approx$2.9-3.45, a few hairpins unfold and take up the strain in a highly non-affine way, some chains disintersperse (facilitated by the regular network topology) and a few cross-links rearrange to minimize any misalignment with the strong smectic field. As a result, a new smectic chain domain is created in a continuous way from adjacent smectic domains (Figure 4.3a at α =3.45). During the "birth" of the new smectic chain domain, the overall amount of order decreases not only because the temporary chain rearrangements but also from the frustration of this new domain as it packs between closely spaced crosslink domains. Such frustration, just as before, leads to the formation of *accordion-like* Sm C_A phases between the newest domain and the adjacent "parent" domains. The occurrence of the Sm C_A phase is associated with a drop in stress and in the overall orientational order, both arising from the increase of orientational entropy of the bundled chains (Figures 4.3c, 4.3a, and 4.2a at α =3.45). After the new Sm C_A domains are formed, the principal deformation mechanism is again the expansion of *bellows* of the bundled chains, and this continues until all the chain domains become Sm A ($\alpha \approx$3.45-3.90) and the overall order reaches another maximum. After that, the deformation cycle (Sm A – hairpin unfolding – Sm C_A – *bellows* expansion - Sm A) keeps repeating until all possible chain Sm A domains are created and all chain hairpins have been unfolded. A simplified sketch of this iso-strain deformation cycle is shown in Figure 4.3b.

4.3.3 Shape-memory Effects of the Stiff Diamond Network: Tensile Hysteresis and Anisotropy. The liquid crystalline diamond network shows evidence of significant irreversibility in its deformation mechanism for both iso-stress[2] and iso-strain uniaxial extensions. Figure 4.4a shows the stress-strain curve for three

consecutive uniaxial deformation runs: a first loading, unloading, and a second loading. Smectic elastomers have been found [57,62] to exhibit experimentally such irreversible elastic response (known as poor strain or shape recovery) that leads to shape-memory effects, which are distinguishing properties of multiple smart materials. The pronounced hysteresis observed during the combined loading-unloading-loading run (Figure 4.4a) arises from the ability of the stiff diamond network microstructure to retain information about its previous deformation history. For instance, upon unloading at α =2.0, the smectic diamond network "remembers" its previous highly extended state and preserves the four smectic chain domains (formed at much higher extension ratios) although the network displayed only two smectic domains at the same extension ratio during the first loading (Figure 4.4d). This is because the deformation mechanism during unloading is mostly limited to collapsing the *accordion-like bellows* of bundled chains of the Sm C_A phase (Figure 4.4d). Successive merging of ordered chain domains (reversing the first loading elongation mechanism) is not observed because the associated energetic barrier cannot be surmounted during unloading when no energy is transferred to the system.

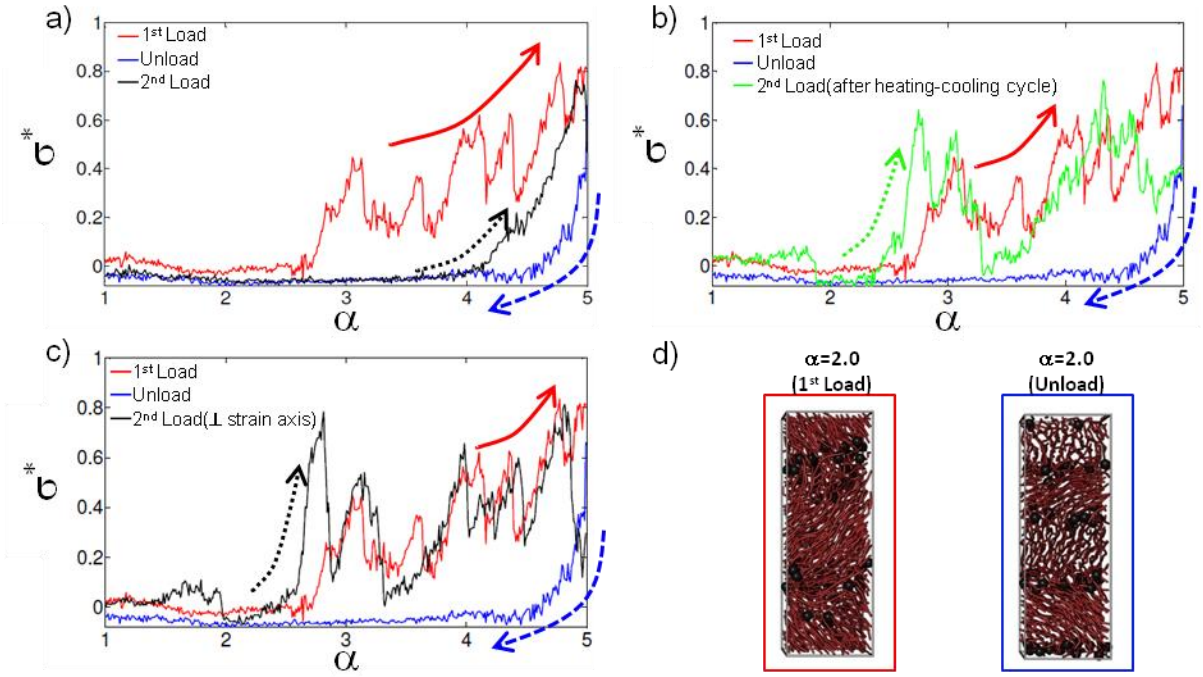

Figure 4.4: (a-c) Simulated tensile response for loading-unloading-loading runs of a 20-mer diamond network with K_{Bend}=5 under iso-strain uniaxial deformations (T^* = 2.0). (a) Second loading run is performed immediately after the unloading run is finished. (b) A heating (T^* = 4.0 for $10^5\sigma_{LJ}$ $(m_{LJ}/\epsilon)^{1/2}$ time units) and cooling (T = 2.0 for $10^6\sigma_{LJ}$ $(m_{LJ}/\varepsilon)^{1/2}$ time units) process is carried out between the end of the unloading run and the beginning of the second loading run. (c) A second uniaxial extension is performed along a direction perpendicular to the first strain axis immediately after the unloading run is finished. In these three figures, stress σ^* is in k_BT/σ_{LJ}^3 units. Solid, dashed, and dotted arrows follow σ^* vs. α for first loading, unloading, and second loading runs, respectively. (d) Comparison between simulation snapshots at fixed elongation ratio (α = 2.0) for both the first loading (left) and unloading (right) runs. Marked microstructural differences are evidence of the material memory of its deformation history.

One common way to "erase" the shape memory of "smart" liquid crystal elastomers is by increasing the temperature above the nematic (or smectic) – isotropic transition.[57,62] The stress-strain curve shown in Figure 4.4b corresponds to a combined loading – unloading – loading deformation run in which the network was heated (beyond the isotropization transition) and then cooled down back to the original temperature between the unloading and the second loading deformations. Due to this heating-cooling process, the Sm C_A phase formed during the first loading is completely destroyed, and the stiff diamond network, hence, "forgets" its previous

highly stretched state recovering the *sawtooth* shaped tensile response.

After the unloading run and at α =1.0, the diamond network still has the smectic director very aligned to the first loading strain axis. If the second loading extension is performed along any direction perpendicular to the original strain axis, the *sawtooth* stress-strain curve is also recovered without any heating and cooling (Figure 4.4c). This occurs because the previously formed smectic chain domains need to be completely rearranged and reassembled in an orthogonal direction, which seem to require a higher amount of energy than forming the original smectic domains from the initial nematic undeformed state (see higher peak around $\alpha \approx 2.7$). Carefully synthesized smectic liquid crystalline elastomers[48,51] where all the smectic layers have the same director (somewhat comparable to the diamond network after the unloading) have been shown to display similar anisotropy in their stress-strain curves (i.e., their elastic responses strongly dependent on the relative orientation of the strain axis with respect to the smectic director).

4.3.4 Tuning the Tensile Properties of the Regular Liquid Crystal Elastomers. In this subsection we explore the effects of modifying selected "design" variables on the tensile response of regular semiflexible elastomers. More specifically, we describe how the elastic properties of these ideally regular liquid crystalline elastomers can be tuned by changes in the network connectivity, chain length and stiffness, and chemical polydispersity of chains.

4.3.4.1 Chain length and network architecture. The elastic response of a 50-mer diamond network (not shown) with stiff mesogenic chains (K_{Bend}=5; T*=2.0) does not show any qualitative differences from that of the 20-mer stiff diamond network shown in Figure 4.2a. Expectedly, the major quantitative difference is that the stresses

obtained for this 50-mer diamond network are considerably lower due to its lower cross-link concentration.

Different regular lattice structures for the network connectivity were also examined. Both double diamond (Figure 4.5a) and double gyroid (not shown) networks display the *sawtooth* stress-strain curve and the same deformation mechanism that relies on successive creation of smectic chain domains coupled with the *accordion-like* distortion of such chain domains. As expected, the stresses for the stiff double gyroid network (trifunctional crosslinks) are also lower than those of the diamond networks (tetrafunctional crosslinks) due to a lower cross-link functionality. The evolution of the orientation order parameter *S* with the extension ratio (Figure 4.5b) of the double diamond network is very similar to that of the (single) diamond network (Figure 4.3c), exhibiting a rapid increase at small strains and oscillations at larger strains (corresponding to the creation and distortion of Sm C_A domains).

The only noticeable (qualitative) difference between the tensile responses of the double diamond and (single) diamond networks is that the range of strains where the former exhibits the liquid-like or perfectly *soft* behavior is much narrower than that of the latter (compare Figure 4.5a to Figure 4.2a). It seems that, in the range of small extension ratios, the rotation of the nematic director together with the small chain rearrangements do not occur at constant configurational plus orientational entropy in the double diamond network as it does with the (single) diamond one. We attribute this difference (i.e., *semisoft* response) to the excluded volume interactions (trapped entanglements) between chains belonging to different interpenetrating networks that may hamper the initial chain disinterspersion and cross-links rearrangement to transition to a smectic phase. The strain-induced nematic-smectic transition occurs

around the same extension ratio ($\alpha \approx$1.5-1.8) as for the (single) diamond network; the only difference is that it requires a small (non-zero) amount of energy for the double diamond network.

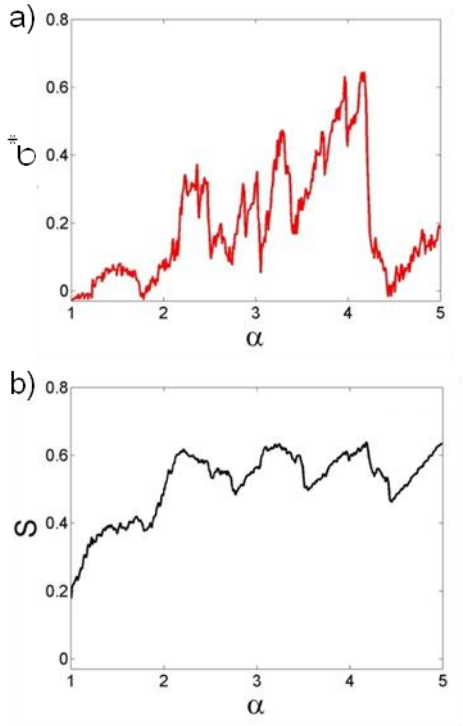

Figure 4.5: (a) "*Sawtooth-shaped*" stress-elongation ratio (σ^*vs. α) curve for a 20-mer double diamond network with K_{Bend}=5 under iso-strain uniaxial deformation (T^* = 2.0). (b) Ensemble average of the segment orientation order parameter "*S*" vs. extension ratio "α" for the same liquid crystalline network.

4.3.4.2 Chain stiffness: isotropic-nematic/smectic transitions. Chain stiffness is perhaps the most significant factor impacting on the elastic behavior of the semiflexible regular networks as it determines the occurrence of mesomorphic activity. For the force field used in this work, a one-to-one mapping can be established between temperature and chain stiffness to create mesomorphic phase diagrams as a function of chain stiffness (instead of temperature). The occurrence of liquid crystalline phases, as previously described, completely alters the deformation

mechanisms, and hence the tensile response, of these idealized regular networks. For instance, in isotropic networks the differences in free energy that govern the deformations are tied to the changes in entropy due to chain end-to-end distances, whereas in mesogenic elastomers the free energy landscape is a more complex non-linear function, weakly dependent on the chains end-to-end distances.[11] This non-linear function strongly depends on entropic contributions arising from hairpins and anisotropic packing frustrations, which may even occur at two different length scales (e.g., chain persistence and chain domain characteristic lengths).[11]

In previous works[24,25] for an equivalent diamond network under iso-stress deformations, it was reported that the transition from continuous (classical isotropic) to *stepwise* (liquid crystalline) elastic behavior occurs in the range of chain stiffness $3 < K_{Bend} < 4$. Figure 4.6a shows the iso-strain stress-strain curves ($T = 2.0$) of 20-mer semiflexible diamond networks for $3.5 \leq K_{Bend} \leq 5.0$. The overall isotropic (monotonous trend) – mesomorphic (*sawtooth* profile) transition must occur for K_{Bend} slightly below 3.75. Although the diamond network with K_{Bend} =4 clearly shows the *sawtooth* shaped tensile behavior, it does not exhibit the signature of a nematic phase in the undeformed state (α =1.0, see its simulated deuterium NMR spectrum and its snapshot: Figure 4.6c and Figure 4.6e, respectively). On the other hand, the diamond network with K_{Bend} =5 exhibits the typical anisotropic features[63] of a nematic elastomer (see its simulated NMR spectrum and its snapshot: Figure 4.6b and Figure 4.6d, respectively). In fact, the NMR spectrum of the diamond network with K_{Bend} =4 is closer to that of an isotropic elastomer than that of a nematic one; therefore, subsequent mesomorphic phases observed for this network (not shown) are mostly strain-induced, and thus more prone to have defects (e.g., the smectic defects

mentioned in section 4.3.2).

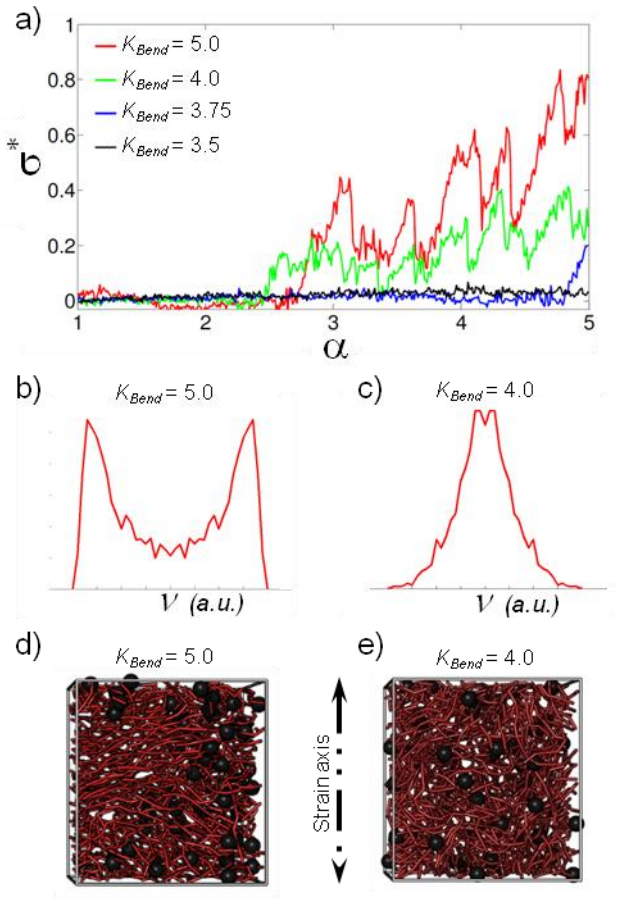

Figure 4.6: (a) Iso-strain stress-elongation ratio (σ^*vs. α) curves for 20-mer diamond networks with different values of chain stiffness K_{Bend}. Coupling between mesomorphic behavior and chain deformation (K_{Bend} > 3.75) completely dominates the elastic response of the diamond networks. Stress σ^* is in k_BT/σ_{LJ}^3 units. (b-c) Simulated NMR spectra for 20-mer diamond networks with K_{Bend} = 5 (b), and K_{Bend} = 4 (c) at their undeformed states. NMR spectra calculation is described in detail in previous works.[64,65] (d-e) Simulation snapshots for 20-mer diamond networks with K_{Bend} = 5 (d), and K_{Bend} = 4 (e) at their undeformed states. All these networks were simulated at the same temperature: T^* = 2.

4.3.4.3 Chemical polydispersity: enhanced tensile properties through further microsegregation. It has been stated throughout this work that strain-induced microsegregation between mesogenic chains and cross-links in alternating layers is one of essential features to attain the distinct tensile behavior displayed by the stiff regular elastomers. Moreover, the weaker the microsegregation, the more smectic

defects the network would have, and the less pronounced the *sawtooth* shape of the stress-strain curve would be (see Figure 4.6a). Starting from that premise, one way to augment the extent of microsegregation between cross-links and mesogenic chains is to add an energetic bias toward segregation; e.g., by replacing the mesogenic homopolymer chains with tri-block copolymer A(25%)-B(50%)-A(25%) mesogenic chains, where blocks A and B mutually repel each other (relative to their self interactions). Such tri-block copolymer chains, when free in a melt at temperatures below their order disorder transition, have the tendency to microphase separate into a symmetric lamellar phase, which should further stabilize the microsegregation between mesogenic chains and cross-links in alternating layers for end-linked networks. Figure 4.7a displays a fully extended (for clarity) diamond network made of A(25%)-B(50%)-A(25%) tri-block copolymer chains.

After equilibration (see section 4.A.1.2 for details), the diamond network with moderately stiff (K_{Bend} =4) tri-block copolymer chains effectively microphase separate into a lamellar phase (Figure 4.7b) that stabilizes a smectic phase formed by chain domains at the undeformed state (α =1.0). Recall that equilibrium smectic phases at the undeformed state were not observed for the K_{Bend} =4 homopolymer network.

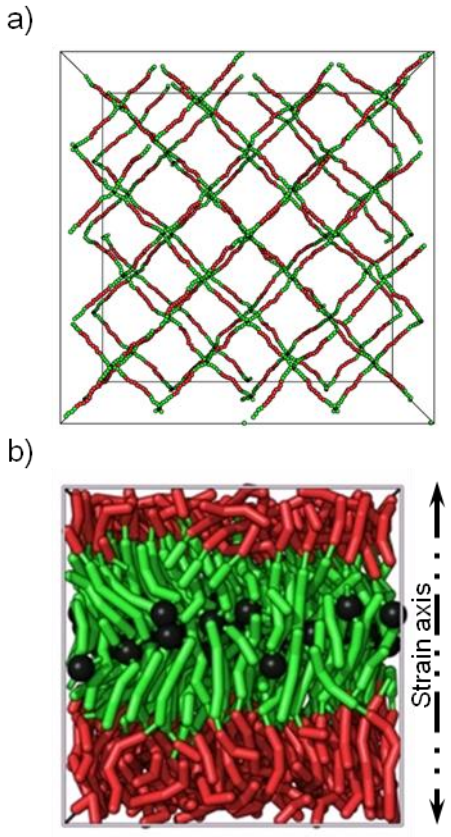

Figure 4.7: (a) Snapshot of the fully extended 20-mer diamond tri-block copolymer network with K_{Bend}=4. (b) Simulation snapshot at the equilibrated (T^* = 2.0 and χN > 60) undeformed state (α =1) for the same network. The chemical disparity introduced by the tri-blocks significantly favors the formation of smectic phases through (lamellar) microphase separation of the blocks. Black beads, red, and green strands represent cross-links, B (central) block, and A (end) block chains, respectively.

Figures 4.8a and 4.8b show the stress-strain curve and the segment orientation order parameter vs. extension ratio, respectively, for the diamond network with moderately stiff (K_{Bend} =4) tri-block copolymer chains. As expected, the use of mesogenic tri-block copolymer chains significantly changes the tensile response of the equivalent homopolymer diamond network in at least three ways: (1) The stress values and hence the toughness (area under the stress-strain curve), are about fivefold larger; (2) the stress-strain curve has very pronounced *sawtooth* shape, and (3) the equilibrium elastic modulus of the network (α =1) is finite (greater than zero).

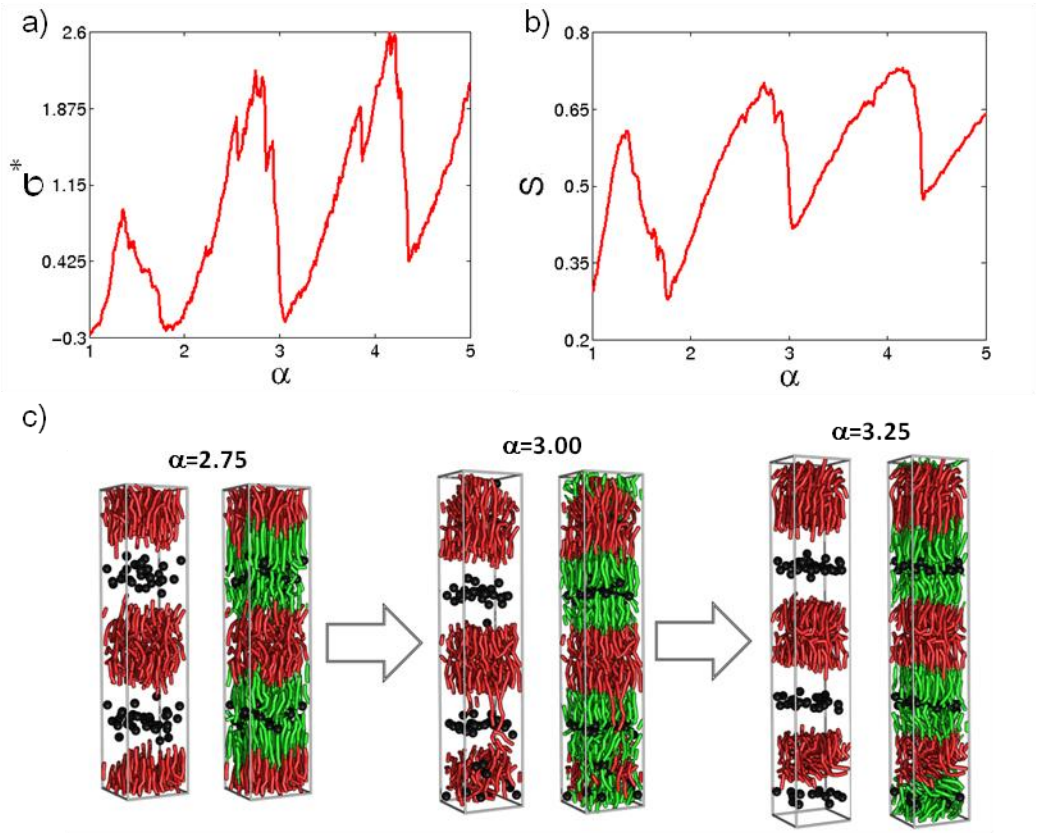

Figure 4.8: Iso-strain uniaxial deformation of 20-mer diamond tri-block copolymer network with K_{Bend}=4 at T^* = 2.0 and $\chi N > 60$. (a) Enhanced "*sawtooth-shaped*" stress-elongation ratio (σ^*vs. α) curve. (b) Ensemble average of the segment orientation order parameter "*S*" vs. extension ratio "α". (c) Simulation snapshots at different elongations (α = 2.75; 3.00; 3.25). Creation of newer smectic domains in tri-block networks also occurs continuously and from neighboring domains. Black beads, red, and green strands represent cross-links, B (central) block, and A (end) block chains, respectively. For clarity, snapshots without the A blocks are also shown.

The deformation mechanism for the diamond network with moderately stiff tri-block copolymer chains is the same as the one described for the stiff homopolymer diamond network—successive creation and distortion of smectic chain domains (see Figure 4.8c and the tri-block copolymer video in the Supplemental Information). We attribute the remarkable enhancement of the elastic response of the regular tri-block copolymer network to: 1) the fewer (or even lack thereof) smectic defects, 2) the

stabilization of smectic chain domains and stronger cross-link confinement, and 3) the increase of the energy barriers for new domain formation. The stabilization of the smectic phases and the occurrence of fewer smectic defects allow for a much more concerted strain-induced creation of new smectic domains (i.e., the "birth" of new smectic chain domains occurs more simultaneously and in a narrower range of strain values). This concertedness is promoted by the much higher energetic penalty that chains of one type would experience if they individually cross domains of the other block type. Therefore, a more collective (or cooperative) crossing motion takes place which leads to an overall deformation of the chemical domains involved in the formation of a new smectic domain. Deforming the existing domains and creating new smectic domains require an additional amount of work to overcome the energetic barriers associated with the increase of interfacial area between dissimilar chemical domains. We also attribute the complete disappearance of the *soft* region (liquid-like behavior) to such chemical-disparity barrier that is active even at small deformation.

Because chemical disparity significantly stabilizes the smectic chain domains and enhances the tensile response of moderately stiff diamond networks, we also explore whether this stabilizing effect, due to the tri-block copolymer chains, is sufficient to produce a *sawtooth* elastic response for a fully flexible diamond network. In Section 4.3.4.2 we determined that a minimum chain stiffness value of $K_{Bend} > 3.5$) was required to have the atypical *sawtooth* stress-strain curve in diamond homopolymer networks. The fully flexible 20-mer diamond tri-block copolymer network after equilibration displayed microphase segregation (a lamellar phase similar to the one shown in Figure 4.7b), and the stress-strain curve also exhibits a *sawtooth* profile (albeit less pronounced), as shown in Figure 4.9a. Therefore, the successive

and discrete-like deformation mechanism seen in these networks with regular connectivity can be alternatively obtained through microphase separations driven by chemical disparity only.

In a similar line of thought, we also investigate whether the chemical disparity can produce a *sawtooth* stress-strain curve even in a network with random connectivity. More specifically, we take a look at a fully flexible 20-mer tri-block copolymer network that was created via random end-linking. The end-linking process was carried out under dilute conditions to minimize the number of chain entanglements and increase the chains ability to rearrange, disintersperse, and spontaneously form smectic domains. Additional details on how this realistically end-linked network was created can be found in the Appendix 4.A. Figure 4.9b shows that stress – strain curve of this realistically end-linked tri-block copolymer network also exhibits the *sawtooth* pattern although with fewer "teeth". This result therefore suggests that the regularity in the network connectivity is not essential for the *sawtooth* tensile response.

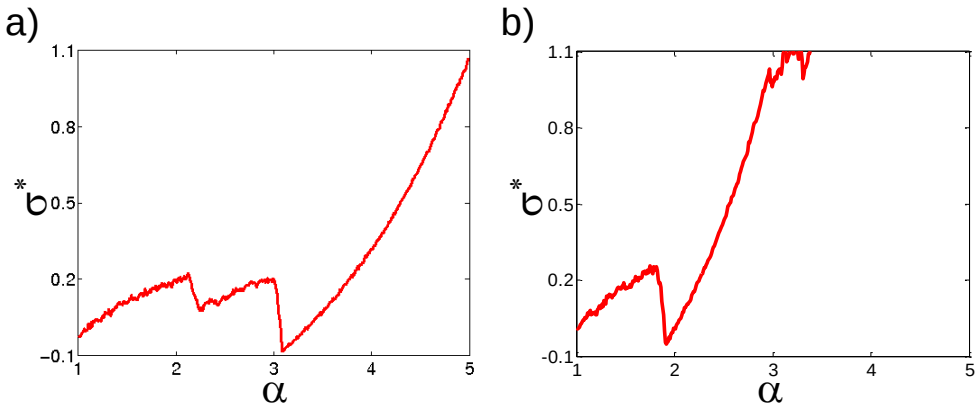

Figure 4.9: Iso-strain stress-elongation ratio (σ^* vs. α) curves for (a) a fully flexible (K_{Bend} = 0) 20-mer diamond tri-block copolymer network, and (b) a realistically end-linked 20-mer tri-block copolymer network with K_{Bend} = 0. T^* = 2.0 and χN > 60 for (a) & (b). Stress σ^* is in k_BT/σ_{LJ}^3 units.

Although regularity in the network connectivity and chain stiffness (or mesogenic activity) do not seem to be strictly necessary to produce a *sawtooth-like* stress-strain curve, enthalpy-driven microphase separation combined with regular connectivity and main-chain mesomorphic activity gives the best defined and enhanced sawtooth tensile response. This enhancement in the tensile response may be attributed to the synergistic and simultaneous stabilization of microphase separation of the tri-blocks, and the liquid crystalline smectic domains that are promoted by the lack of chain entanglements and frozen structural disorder found in highly regular networks.

It is worth mentioning that such sawtooth tensile response, observed in the networks discussed in this work, is expected to occur only at nanoscales. This is because the *saw teeth* will smear—as a consequence of averaging the resulted stress over larger spatial regions–and produce a much smoother stress-strain curve as the size of the sample increases.

4.3.5 Successive and Discrete-like Extension as Toughening Mechanism. *Sawtooth* iso-strain elastic responses have been observed at nanoscales, through atomic force microscopy, in natural materials with extraordinary mechanical strength such as the muscle protein titin[66] and organic polymer adhesives[67] found between carbonate plates in abalone shells. The outstanding toughness—total energy that can be absorbed via deformation (i.e., the area under the stress-strain curve)—of such natural materials has it origin in deformation mechanisms that also involve discrete and sequential processes. For instance, the deformation mechanism of the polymer adhesive between nacre tablets[67] consists of successive and concerted unraveling of discrete "modules" of folded adhesive polymer structures. A rough comparison

between the discrete and sequential deformation mechanisms of both adhesive polymers in nacre and liquid crystal elastomers with regular topology is displayed in Figure 4.10. The oscillatory nature of these stress-strain curves allows to maintain a relatively high value of average stress over a large range of strains,[67] resulting in considerably high toughness (much larger area under the stress-strain curve than that of typical elastomers). Similar toughing mechanisms[14,68] are also found in spider and worm silk fibers where successive splitting of beta-sheet crystallites by breaking dense regions of hydrogen bonds (after the semi-amorphous protein domains have been highly extended) play an important role on their outstanding tensile strength.

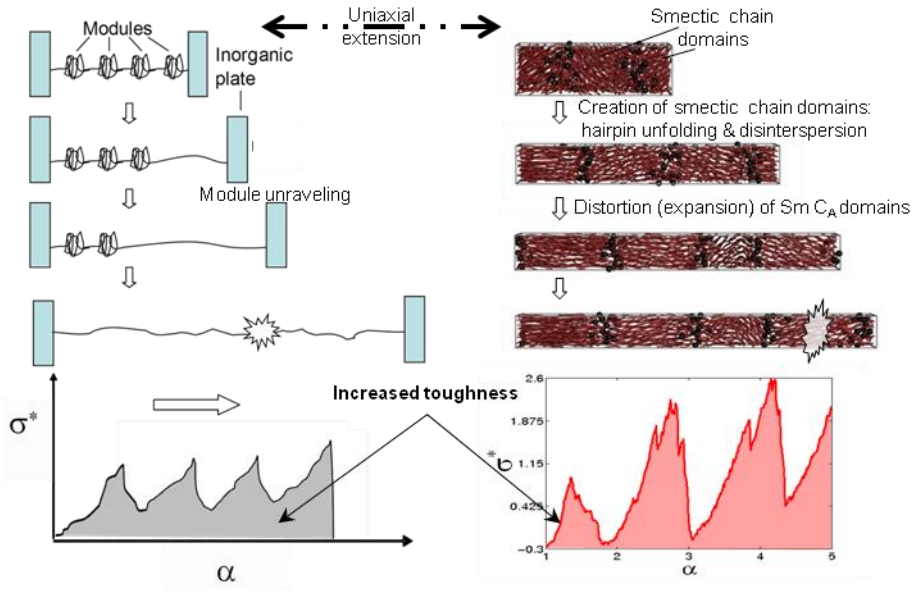

Figure 4.10: Similarities between tensile responses and deformation mechanisms of organic polymer adhesives in nacre[67] (left) and liquid crystal elastomers with regular connectivity (right).

4.4 Summary and Conclusions

A distinctive *sawtooth*-shaped elastic response was found for model elastomer networks of semiflexible chains with regular connectivity undergoing iso-strain uniaxial deformations at nanoscales, or scales comparable to the characteristic length

of liquid crystalline smectic domains found in such networks. It is also shown that the discontinuous *staircase-like* stress-strain curve previously reported for iso-stress deformations of these networks[24,25] can be mapped from the *sawtooth* iso-strain stress-strain curve. This unusual tensile response arises from both chain mesomorphic activity (associated with chains with sufficient stiffness) and the network regular topology. A mesogenic single diamond network exhibits a perfect *soft* elastic behavior, including a bucking instability preceding hardening, up to moderate extension ratios ($\alpha < 2.9$), followed by the oscillatory *sawtooth* pattern for larger strains. Such sawtooth stress-strain curve considerably increases the network toughness by maintaining high average stresses over wide strain intervals, in a manner similar to that reported[66,67] for *super* tough natural materials (e.g., nacre, titin, and spider silk).

The elastic sawtooth pattern arises from a distinct, highly non-affine, deformation mechanism. This mechanism involves two processes: 1) the successive creation of smectic (Sm C_A) chain domains, which (due to the regular network architecture) exclude cross-links in parallel layers; and 2) the *accordion-like* distortion of such chain domains. Contrary to the discontinuous transitions observed[24,25] during iso-stress deformations, under iso-strain elongation newer Sm C_A chain domains are created (once the Sm C_A domains have become Sm A and can no longer be stretched) in a continuous and concerted fashion by hairpin unfolding and disinterspersion of mesogenic chains.

The simulated semiflexible regular networks undergoing mesomorphic activity exhibit pronounced elastic hysteresis due to the irreversibility of the deformation mechanism; smectic domains do not merge upon unloading. After a loading-unloading

cycle these networks have highly anisotropic configurations and, similarly to elastomers with shape-memory effects, can be reset to their “initial”, still anisotropic but less ordered states by increasing the temperature above the isotropization transition.

The type of network architecture was found to have a small effect on the *sawtooth* elastic response as long as the connectivity is regular in homopolymer networks. On the other hand, chemical polydispersity, through the use of semiflexible tri-block copolymer chains, was found to significantly amplify the *sawtooth* stress peaks and overall elastic response. This mechanical enhancement can attributed to 1) the further stabilization of the smectic chain domains and increase in the cross-links confinement brought about by the microphase separation of the different blocks, and 2) the higher deformation energy barriers caused by the enthalpic penalty associated with the transient increase of the inter-block interfacial area during the creation of new smectic domains. In addition, we also found that the stabilization of the smectic chain domains due to the chemical disparity between the different blocks may be sufficient to produce less pronounced *sawtooth* elastic behavior in fully flexible networks with regular and realistically end-linked connectivities.

The distinctive elastic responses of the elastomeric networks studied herein arise from combinations of network architecture, chains mesomorphic activity, and microphase separation driven by chemical disparity of the different blocks of the copolymer chains. Additional opportunities of finding materials with unprecedented tensile properties may still remain unveiled within the space defined by these three factor or even other “design variables”. For instance, other phases induced via microphase separation and network architecture such as FCC, and BCC, may lead to

similar successive and discrete-like deformation mechanisms but in a more isotropic fashion. Moreover, because one of the major technological areas of application of liquid crystal elastomers is actuators and artificial muscle, further simulation work on coupling these liquid crystal elastomers with regular connectivity with actuating mechanisms (e.g., magnetic, and optical) can result in providing more encouragement to material scientists to synthesize these highly regular mesogenenic elastomers.

4.5 Acknowledgments

The authors thank Professor Ronald C. Hedden for very insightful discussions about this work. This work was supported by the American Chemical Society Petroleum Research Fund, and the National Science Foundation Polymers Program under Grant DMR-0705565.

4.A Appendix

4.A.1 Network Preparation. The following subsection describes the preparation of the model networks with regular and realistic connectivity. In general, all model networks are first created at relatively low densities (swollen-like state), and then are gradually compressed until melt-like bead densities are attained.

4.A.1.1 Creation of swollen model networks. Model networks, of either homopolymer or tri-block copolymer chains, with regular connectivity are created by initially placing cross-links on the sites of a chosen crystal lattice, and later growing chains through random walks between cross-links. To preserve the lattice structures, this process is carried out at very low bead densities (in the order of $10^{-3}\sigma_{LJ}^{-3}$) at which point these regular networks have highly extended strands. In most cases we use 20-bead chains (with 50-bead chains in a few networks) and three different crystal lattice

topologies: a) diamond lattice (Figure 4.1a), having a single entanglement-free network with tetrafunctional cross-links (128 strands and 64 nodes); b) double diamond lattice (Figure 4.1b), with two bicontinuous interpenetrating networks with tetrafunctional cross-links (256 strands and 128 nodes); and c) double gyroid lattice (Figure 4.1c), with two bicontinuous interpenetrating networks with trifunctional cross-links (192 strands and 128 nodes).

Elastomer networks of A(25%)-B(50%)-A(25%) tri-block copolymer chains with more realistic connectivity are created through simulations of the end-linking reaction. Such curing simulations are carried out on a lattice in the framework of the Bond Fluctuation Model (BFM).[69] Detailed descriptions of this end-linking simulation scheme can be found in previous works.[64,65,70] Coarse-grained units (i.e., chain beads and cross-links) are represented as cubes which only experience excluded-volume interactions and bonding restrictions during the reaction process (conditions consistent with a temperature well above the order-disorder transition "ODT" and the nematic-isotropic transition). During curing, polymer volume fractions lower than those of the melt are used to obtain networks with fewer trapped entanglements,[31] so that an implicit solvent is present. Tri-block copolymer chains with fewer entanglements may exhibit an enhanced capability to rearrange through chain disinterspersion and micro-phase separate within the network. In the BFM a polymer volume fraction of $\varphi_m \approx 0.46$ approximates melt-like conditions,[71] and the volume fractions used during end-linking are $\varphi = 0.60\varphi_m$ and $0.40\varphi_m$ for networks made of 20- and 50-bead chains, respectively. These volume fractions are greater than the corresponding chain overlap volume fractions, $\varphi^* = 0.48\varphi_m$ (20-bead) and $0.28\varphi_m$ (50-bead), calculated from the radii of gyration of the chains in the melt.

The curing simulation is initiated by randomly placing (128) chains and (70) cross-links in the simulation box and subsequently relaxing them with 10^6 hop moves per coarse-grained unit.[64,65,70] Following this relaxation period, the actual end-linking begins and bond formation between chain ends and neighboring cross-links is allowed as the equilibrating hop moves continue. The curing ends after almost all the chain ends react. Resulting soluble fractions are less than 1.0 mass%, and fractions of elastic material—chains that are neither single looped nor pendent—are 98.3 mol% and 96.0 mol % for the networks made of 20- and 50-bead chains, respectively.

4.A.1.2 Gradual network compression and network equilibration. In the continuum MD framework, the bead densities of the created networks are in the order of $10^{-3}\sigma_{LJ}^{-3}$ for the networks with regular connectivity, and $10^{-1}\sigma_{LJ}^{-3}$ for those realistically end-linked, after an appropriate transformation of the BFM lattice coordinates into the off-lattice scheme. Through a subsequent gradual isotropic compression of the network, or "extraction" of the implicit solvent, a final melt-like bead density of ρ= $0.90\sigma_{LJ}^{-3}$ is obtained via MD. The compression is carried out in a quasi-continuous fashion; box dimensions l_{box} are slightly varied every 5000 MD time steps (i.e., time interval of $25\sigma_{LJ}$ $(m_{\mathrm{LJ}}/\varepsilon)^{1/2}$), and the rate at which l_{box} varies is $d(l_{box})/dt$=-4×10^{-6} $(\varepsilon/m_{\mathrm{LJ}})^{1/2}/\sigma_{LJ} \times l_{box}$. Such a constant logarithmic compression rate (i.e., exponential decay of the box dimensions with time) allows for faster deformation rates at very low densities (i.e., beginning of the compression) when chains have plenty of space to rearrange, and slower deformation rates at higher densities when little free space is available. During the compression run the temperature is set to T^*= k_BT/ε =2.0, and all the energetic interactions (such as, excluded volume, bending,

bonding, and chemical affinity or disparity) are turned on. Once the melt-like density is attained, an additional equilibration MD run at constant volume of up to 2×10^8 time steps (time $\approx10^6\sigma_{LJ}$ $(m_{LJ}/\varepsilon)^{1/2}$) is performed until converged values are observed for properties such as, average potential energy, stress, bending angle, and segment orientation order parameter.

REFERENCES

(1) Sigaud, G.; Yoon, D. Y.; Griffin, A. C. *Macromolecules* **1983**, *16*, 875–880.

(2) Dijkstra, M.; Frenkel, D. *Phys. Rev. E* **1995**, *51*, 5891.

(3) Wilhelm, J.; Frey, E. *Phys. Rev. Lett.* **2003**, *91*, 108103.

(4) Warner, M.; Terentjev, E. M. *Progress in Polymer Science* **1996**, *21*, 853–891.

(5) Urayama, K. *Macromolecules* **2007**, *40*, 2277–2288.

(6) Knight, D. P.; Vollrath, F. *Philosophical Transactions of the Royal Society of London. Series B: Biological Sciences* **2002**, *357*, 155 –163.

(7) Warner, M.; Terentjev, E. M. *Liquid crystal elastomers*; Oxford University Press, 2007.

(8) Gardel, M. L.; Shin, J. H.; MacKintosh, F. C.; Mahadevan, L.; Matsudaira, P.; Weitz, D. A. *Science* **2004**, *304*, 1301 –1305.

(9) Janmey, P. A.; McCormick, M. E.; Rammensee, S.; Leight, J. L.; Georges, P. C.; MacKintosh, F. C. *Nat Mater* **2007**, *6*, 48–51.

(10) MacKintosh, F. C.; Käs, J.; Janmey, P. A. *Phys. Rev. Lett.* **1995**, *75*, 4425.

(11) Adams, J. M.; Warner, M. *The European Physical Journal E* **2005**, *16*, 97–107.

(12) Storm, C.; Pastore, J. J.; MacKintosh, F. C.; Lubensky, T. C.; Janmey, P. A. *Nature* **2005**, *435*, 191–194.

(13) Dalhaimer, P.; Discher, D. E.; Lubensky, T. C. *Nature Physics* **2007**, *3*, 354.

(14) Wu, X.; Liu, X.-Y.; Du, N.; Xu, G.; Li, B. *Applied Physics Letters* **2009**, *95*, 093703–093703–3.

(15) Nova, A.; Keten, S.; Pugno, N. M.; Redaelli, A.; Buehler, M. J. *Nano Lett.* **2010**, *10*, 2626–2634.

(16) Corbett, D.; Warner, M. *Sensors and Actuators A: Physical* **2009**, *149*, 120–129.

(17) Corbett, D.; Warner, M. *Liquid Crystals* **2009**, *36*, 1263–1280.

(18) Woltman, S. J.; Jay, G. D.; Crawford, G. P. *Nat Mater* **2007**, *6*, 929–938.

(19) Thomsen, D. L.; Keller, P.; Naciri, J.; Pink, R.; Jeon, H.; Shenoy, D.; Ratna, B. R. *Macromolecules* **2001**, *34*, 5868–5875.

(20) Spillmann, C. M.; Naciri, J.; Martin, B. D.; Farahat, W.; Herr, H.; Ratna, B. R. *Sensors and Actuators A: Physical* **2007**, *133*, 500–505.

(21) Urayama, K.; Kohmon, E.; Kojima, M.; Takigawa, T. *Macromolecules* **2009**, *42*, 4084–4089.

(22) Biggins, J. S.; Warner, M.; Bhattacharya, K. *Phys. Rev. Lett.* **2009**, *103*, 037802.

(23) Biggins, J. S.; Warner, M.; Bhattacharya, K. *Journal of the Mechanics and Physics of Solids* **2012**, *60*, 573–590.

(24) Bhawe, D. M.; Cohen, C.; Escobedo, F. A. *Physical Review Letters* **2004**, *93*, 257804–257804–4.

(25) Bhawe, D. M.; Cohen, C.; Escobedo, F. A. *J. Chem. Phys.* **2005**, *123*, 014909–11.

(26) Tschierske, C. *Chem. Soc. Rev.* **2007**, *36*, 1930–1970.

(27) Seeman, N. C. *Angewandte Chemie International Edition* **1998**, *37*, 3220–3238.

(28) Biradha, K.; Sarkar, M.; Rajput, L. *Chem. Commun.* **2006**, 4169–4179.

(29) Kremer, K.; Grest, G. S. *J. Chem. Phys.* **1990**, *92*, 5057.

(30) Escobedo, F. A.; de Pablo, J. J. *J. Chem. Phys.* **1997**, *106*, 9858–9868.

(31) Bhawe, D. M.; Cohen, C.; Escobedo, F. A. *Macromolecules* **2004**, *37*, 3924–3933.

(32) Horsch, M. A.; Zhang, Z.; Iacovella, C. R.; Glotzer, S. C. *The Journal of Chemical Physics* **2004**, *121*, 11455–11462.

(33) Frenkel, D.; Smit, B. *Understanding Molecular Simulation*; 2nd ed.; Academic Press, 2001.

(34) Swope, W. C.; Andersen, Hans C.; Berens, Peter H.; Wilson, Kent R. *J. Chem. Phys.* **1982**, *76*, 637.

(35) Carpenter, J. E. *J. Comput. Chem.* **2002**, *23*, 667–672.

(36) Patil, H. P.; Lentz, D. M.; Hedden, R. C. *Macromolecules* **2009**, *42*, 3525–3531.

(37) Golubović, L.; Lubensky, T. C. *Phys. Rev. Lett.* **1989**, *63*, 1082–1085.

(38) Olmsted, P. D. *Journal de Physique II* **1994**, *4*, 16.

(39) Warner, M.; Bladon, P.; Terentjev, E. M. *Journal de Physique II* **1994**, *4*, 93–102.

(40) Terentjev, E. M. *Journal of Physics: Condensed Matter* **1999**, *11*, R239–R257.

(41) Fried, E.; Sellers, S. *Journal of the Mechanics and Physics of Solids* **2004**, *52*, 1671–1689.

(42) Conti, S.; DeSimone, A.; Dolzmann, G. *Journal of the Mechanics and Physics of Solids* **2002**, *50*, 1431–1451.

(43) DeSimone, A. In *Poly-, Quasi- and Rank-One Convexity in Applied Mechanics*; Schröder, J.; Neff, P., Eds.; Springer Vienna: Vienna, 2010; Vol. 516, pp. 241–264.

(44) DeSimone, A. In *Mechanics and Electrodynamics of Magneto- and Electro-elastic Materials*; Ogden, R. W.; Steigmann, D. J., Eds.; Springer Vienna: Vienna, 2011; Vol. 527, pp. 231–266.

(45) Urayama, K.; Mashita, R.; Kobayashi, I.; Takigawa, T. *Macromolecules* **2007**, *40*, 7665–7670.

(46) Brand, H. R.; Pleiner, H.; Martinoty, P. *Soft Matter* **2006**, *2*, 182–189.

(47) Krause, S.; Zander, F.; Bergmann, G.; Brandt, H.; Wertmer, H.; Finkelmann, H. *Comptes Rendus Chimie* **2009**, *12*, 85–104.

(48) Sanchez-Ferrer, A.; Finkelmann, H. *Macromolecules* **2008**, *41*, 970–980.

(49) Ren, W.; McMullan, P. J.; Griffin, A. C. *physica status solidi (b)* **2009**, *246*, 2124–2130.

(50) Biggins, J. S.; Terentjev, E. M.; Warner, M. *Phys. Rev. E* **2008**, *78*, 041704.

(51) Ren, W.; McMullan, P. J.; Griffin, A. C. *Macromolecular Chemistry and Physics* **2008**, *209*, 1896–1899.

(52) Zubarev, E. R.; Talroze, R. V.; Yuranova, T. I.; Plate, N. A.; Finkelmann, H. *Macromolecules* **1998**, *31*, 3566–3570.

(53) Xing, X.; Radzihovsky, L. *Annals of Physics* **2008**, *323*, 105–203.

(54) Rousseau, I. A.; Mather, P. T. *J. Am. Chem. Soc.* **2003**, *125*, 15300–15301.

(55) Hiraoka, K.; Sagano, W.; Nose, T.; Finkelmann, H. *Macromolecules* **2005**, *38*, 7352–7357.

(56) Adams, J. M.; Warner, M. *Phys. Rev. E* **2005**, *72*, 011703.

(57) Ishige, R.; Osada, K.; Tagawa, H.; Niwano, H.; Tokita, M.; Watanabe, J. *Macromolecules* **2008**, *41*, 7566–7570.

(58) Ishige, R.; Tokita, M.; Naito, Y.; Zhang, C. Y.; Watanabe, J. *Macromolecules* **2008**, *41*, 2671–2676.

(59) Sánchez-Ferrer, A.; Finkelmann, H. *Macromolecular Rapid Communications* **2011**, *32*, 309–315.

(60) Brown, A. W.; Adams, J. M. *Phys. Rev. E* **2012**, *85*, 011703.

(61) Li, M. H.; Brûlet, A.; Davidson, P.; Keller, P.; Cotton, J. P. *Phys. Rev. Lett.* **1993**, *70*, 2297–2300.

(62) Giamberini, M.; Cerruti, P.; Ambrogi, V.; Vestito, C.; Covino, F.; Carfagna, C. *Polymer* **2005**, *46*, 9113–9125.

(63) Domenici, V. *Progress in Nuclear Magnetic Resonance Spectroscopy* **2012**, *(In Press)*, DOI: 10.1016/j.pnmrs.2011.07.003.

(64) Aguilera-Mercado, B. M.; Cohen, C.; Escobedo, F. A. *Macromolecules* **2009**, *42*, 8889–8898.

(65) Aguilera-Mercado, B. M.; Genesky, G. D.; Duncan, T. M.; Cohen, C.; Escobedo, F. A. *Macromolecules* **2010**, *43*, 7173–7184.

(66) Rief, M.; Gautel, M.; Oesterhelt, F.; Fernandez, J. M.; Gaub, H. E. *Science* **1997**, *276*, 1109–1112.

(67) Smith, B. L.; Schaffer, T. E.; Viani, M.; Thompson, J. B.; Frederick, N. A.; Kindt, J.; Belcher, A.; Stucky, G. D.; Morse, D. E.; Hansma, P. K. *Nature* **1999**, *399*, 761–763.

(68) Nova, A.; Keten, S.; Pugno, N. M.; Redaelli, A.; Buehler, M. J. *Nano Letters* **2010**, *10*, 2626–2634.

(69) Carmesin I.; Kremer K. *Macromolecules* **1988**, *21*, 2819.

(70) Genesky, G. D.; Aguilera-Mercado, B. M.; Bhawe, D. M.; Escobedo, F. A.; Cohen, C. *Macromolecules* **2008**, *41*, 8231–8241.

(71) Paul W.; Binder K.; Heermann D.; Kremer K. *J. Phys. II* **1991**, *1*, 37.